Experimental investigation of dynamic contact angles on adaptive surfaces

Corrected Version

Experimentelle Untersuchung dynamischer Kontaktwinkeln auf adaptiven Oberflächen

Master-Thesis von Simon Silge
Betreuung: Prof. Dr. Hans-Jürgen Butt, Prof. Dr. rer. nat. Steffen Hardt, Dr. Rüdiger Berger
Tag der Einreichung:

1. Gutachten: Prof. Dr. rer. nat. Steffen Hardt
2. Gutachten: Prof. Dr. Hans-Jürgen Butt

TECHNISCHE UNIVERSITÄT DARMSTADT

Fachbereich Maschinenbau
Institut für Nano- und Mikrofluidik

Experimental investigation of dynamic contact angles on adaptive surfaces
Corrected Version
Experimentelle Untersuchung dynamischer Kontaktwinkeln auf adaptiven Oberflächen

Vorgelegte Master-Thesis von Simon Silge
Betreuung: Prof. Dr. Hans-Jürgen Butt, Prof. Dr. rer. nat. Steffen Hardt, Dr. Rüdiger Berger

1. Gutachten: Prof. Dr. rer. nat. Steffen Hardt
2. Gutachten: Prof. Dr. Hans-Jürgen Butt

Tag der Einreichung:

Bitte zitieren Sie dieses Dokument als:
URN: urn:nbn:de:tuda-tuprints-12345
URL: http://tuprints.ulb.tu-darmstadt.de/1234

Dieses Dokument wird bereitgestellt von tuprints,
E-Publishing-Service der TU Darmstadt
http://tuprints.ulb.tu-darmstadt.de
tuprints@ulb.tu-darmstadt.de

Erklärung zur Master-Thesis

Hiermit versichere ich, die vorliegende Master-Thesis ohne Hilfe Dritter nur mit den angegebenen Quellen und Hilfsmitteln angefertigt zu haben. Alle Stellen, die aus Quellen entnommen wurden, sind als solche kenntlich gemacht. Diese Arbeit hat in gleicher oder ähnlicher Form noch keiner Prüfungsbehörde vorgelegen.

Darmstadt, den July 27, 2019

(Simon Silge)

This is a corrected version created after submission. The results provided by the charging measurements (Figure 48) were wrong by a factor of 10 due to wrong amplification settings in post-processing and are now corrected. That does not change the conclusion as it still shows that charging happens. Another error corrected regards the measurement error of weight measurements mentioned in the text. In the respective diagram Figure 43 the error bars were correct (0.3 mg), but in the text measurement error was wrong (3 μg).

Abstract

Dynamic wetting phenomena appear in many industrial and natural processes and their understanding is important for the improvement of material design in many fields. When a liquid wets a surface, it is possible that the contact changes the wetting properties of the surface e.g. by polymer swelling or molecular reorganisation. A theory for the dynamic contact angle hysteresis (CAH) on adaptive surfaces was proposed by Butt et al. In the present work, a high-speed goniometer was built to measure dynamic contact angles at velocities from less than 1 mm/s to more than 20 cm/s. In the future, this setup can be used in combination with other methods to verify if the adaptive wetting theory is correct. The setup consists of an adjustable tilted plate, a high-speed camera and a backlight illumination. Two modes of adaptation can be investigated on the setup: velocity dependent contact angles for fast adaptation time scales and drop-wise adaptation for slow adaptation time scales. The functionality of the setup was verified by measuring the dynamic CAH on two testing materials, namely fluorosilane and poly(dimethylsiloxane)(PDMS) brushes. The measurements were compared to the theories of adaptive and non-adaptive wetting. The molecular kinetic theory and adaptive wetting theory have shown good fitting performance. Additionally, drop-wise adaptation was investigated by measuring velocity and contact angles over a series of drops on PDMS. The velocity was found to increase or decrease over the drop number. The increasing velocity can be explained by a significant increase of contact angles that was observed. Exposing the surface to air for a few minutes or the use of an ionising air blower can reverse the observed changes in velocity to a great extent, but not completely. Additional experiments proved that drop charging occurs and also shows drop-wise dependence. It is not clear if this effect is strong enough to explain the change in contact angle, but it is a promising starting point for future investigations.

Acknowledgement

I would like to thank especially my supervisors Prof. Dr. rer. nat. Hardt, Prof. Dr. Butt and Dr. Berger for supporting me during the work on this thesis and for giving me the opportunity to participate in the research on this interesting subject. Special thanks also go to Alexander Saal for all his help throughout the months at the institute. Furthermore, I would like to thank Amy Stetten for her good advice and the help with additional measurements as well as Chao-Ming Zhu and William Wong for the interesting discussions. Thanks also go to the technical staff Gunner Kircher, Uwe Rietzler, Helma Burg, Andreas Best, Andreas Hanewald and Gabriele Schäfer, who provided me help with synthesis, measurements, sample preparation or other advice. I also thank the team from the mechanical and electronic workshop of the institute and all the other colleges that helped me. Last but not least, I would like to thank my sister for proofreading and my family and my girlfriend for their support during my studies and the work on this thesis.

Contents

1 Introduction

Wetting describes the behaviour of a liquid on a solid and wetting phenomena play a crucial role in natural and industrial processes[1]. The wettability, i.e. how well the liquid spreads, is determined by intermolecular forces between liquid, solid and the surrounding phase (e.g. air)[1]. A classical example is the leaf of a Lotus flower[2] (Figure 1). The superhydrophobicity of the leaf makes it nearly impossible for water drops to remain on its surface so that they roll off and remove possible dirt with them. This results in a self-cleaning effect, which is used by a number of plants and protects them from fungi, algae and other types of contamination [2]. The superhydrophobicity is accomplished by a microstructure on the leaf that reduces adhesion and places the drop or dirt particles in so-called 'fakir' state, sitting only on the tips of these structures. The effect of microstructures is also used by insects to maintain their wings clean or improve their ability to walk on water [3]. But also for industrial applications wetting phenomena are of great importance. Low wettability, that means high hydrophobicity, is needed for applications such as waterproofing of textiles, water repellent automotive parts, prevention of bio-fouling and drag reduction in micro-channels[4]. In other cases, hydrophilic behaviour can be essential, for example for coating or deposition of pesticides on plant leaves [5], where the liquid should spread fast and cover the surface with a homogeneous film. For improvement of wetting processes, a deeper understanding of the underlying physical processes is therefore indispensable. Self-cleaning, self-healing, superamphiphobicity and switchable wettability are some examples of current topics of interest in the research [6].

Figure 1: Wetting phenomena: a drop sitting on a Lotus leaf [7].

However, adaption can influence the wetting process. Many studies have shown that surfaces can adapt to the surrounding phase e.g. by swelling or marcomolecular reorientation [8]. The wettability can be affected by these processes and this responsive behaviour can be used to design switchable surfaces [9]. For example, a surface can be switched from hydrophobic to hydrophilic by exposure to different solvents [9]. One of the numerous possible application for adaptive materials is the use in agriculture. Polymer films that are used to prevent soil water evaporation and maintain soil moisture are hydrophobic [10]. This can prevent rain or water from irrigation to reach the crops and soil[10]. An adaptive film can be designed to be hydrophilic when in contact with liquid water to allow its infiltration, but to turn hydrophobic on dry days to decrease evaporation[10]. Adaptation can also be observed on polymers used in everyday applications like poly(ethylene terephthalate) (PET) [11] or polyimides [12], that have shown a change of surface properties over the time of a few minutes. For fast adaptations, this process can be estimated to happen on the microseconds scale [8] and would not be noticed in common wetting characterisation methods, as for example the inflating drop method. These kinds of adaptations might thus still be overlooked but could drastically affect the wetting properties at high speeds, e.g. in industrial coating processes. Therefore, the observation of dynamic contact angles at high contact line velocities can help to characterise rapidly adaptive surfaces correctly and to determine the effect of fast adaptations on the wetting processes.
Butt et al. proposed a theory to describe dynamic wetting on adaptive surfaces. The adaptive wetting theory predicts that contact angles are influenced by surface adaptation and depend on the relation of

adaptation time scales and contact line velocity. To test the predictions of the adaptive wetting theory, experimental data of contact angles on adaptive surfaces is necessary. In order to be able to measure dynamic contact angles at high velocities, a new experimental setup is needed. The aim of this thesis is the construction of such a setup, that allows the measurement of contact angles for drops that move at more than 20 cm/s. For the measurement drops are deposited onto an inclined plate and are recorded with a high-speed camera as they move down the plate. Apart from the construction of the tilted plate setup a suitable software for analysis of the videos was assembled, capable of processing large numbers of images. In order to test the functionality of the setup, a first set of experiments on a possibly adaptive surface in comparison to a presumably non-adaptive surface was conducted.
Ultimately, the proof or disproof of the adaptive wetting theory cannot follow only from dynamic contact angle measurements, as fitting the theory to contact angle data would not verify it. Instead, it will have to be accompanied by measurements of the adaptive time scales. The adaptive time scales constitute the other important parameter of the adaptive wetting theory and therefore need to be identified independently. That can be done by measuring the swelling kinetics in the case of a swelling process. Surface plasmon resonance (SPR) or X-ray reflectometry (XRR) can give time-resolved information about film thickness, surface roughness and density and would be suitable candidates. These measurements are not part of this work and will be carried out in the future. The objective of this thesis was therefore not to be able to lead to a conclusive result about the adaptive wetting theory but the construction of a high-speed goniometer as one part of a number of methods necessary to do so.
The objective of this thesis is the construction of a tilted-plate setup to measure contact angles at high contact line velocities of up to 20 cm/s. Furthermore, the functionality of the setup is to be verified with a first testing material for adaptive wetting and compared to a presumably non-adaptive surface.
This thesis is structured as follows: In Chapter 2 the background of wetting phenomena is explained. This includes a quick discussion of contact angles in equilibrium and of common dynamic contact angle models, namely the hydrodynamic theory and the molecular-kinetic theory in Sections 2.1 to 2.3. Section 2.4 discusses the adaptive wetting processes, first by reviewing published studies on this topic and second by presenting the adaptive wetting theory for dynamic contact angles by Butt et al. [8]. Chapter 3 explains the choice and construction of the tilted plate setup. Mechanical and optical parts are discussed, followed by the measurement software and the general measurement routine. Finally, the choice and synthesis of materials for testing the functionality of the setup is explained. Chapter 4 contains the experimental results and is divided into three sections. Section 4.1 discusses the dynamics of a single drop on an incline, including a comparison to theory. In Section 4.2 the dynamic contact angle hysteresis is measured for a variety of velocities by changing the inclination angle to verify the functionality of the setup. At last, in Section 4.3 the influence of drop history is investigated. The number of drops and time in between experiments to let the surface reverse the possible adaptation are varied. After the presentation of the investigation results, possible causes for the findings are discussed. Future studies can use these as a starting point and try to identify the responsible causes using additional and complementary methods. Finally, a summary and an outlook are given in Chapter 5.

2 Background

2.1 Surface tension and the Young's contact angle

Surface tension has its origin in the fact that liquid molecules adjacent to the interface are in an unfavourable energy state [13]. In contrary to molecules in the bulk of the liquid, they are not surrounded by other liquid molecules from all sides (Figure 2). This situation creates a difference in the molecular interactions and causes the liquid to form a shape of minimal interface area. The work

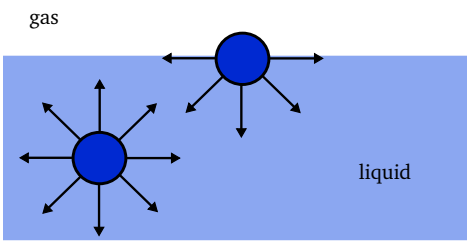

Figure 2: Schematic view of a liquid molecule at a gas-liquid interface and a liquid molecule in the bulk

W necessary to increase the interface area of the liquid by a differential area dA depends directly on the surface tension γ [13]:

$$\delta W = \gamma \cdot dA \tag{1}$$

When a small drop is deposited onto a substrate it will create a spherical cap shape with a specific

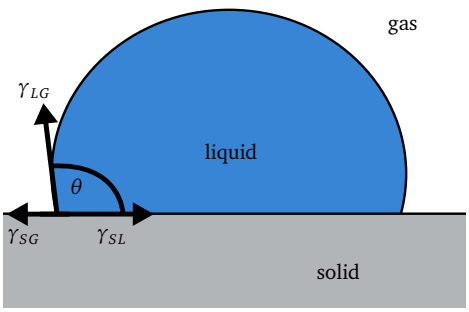

Figure 3: The contact angle and the surface tensions at the three-phase interface

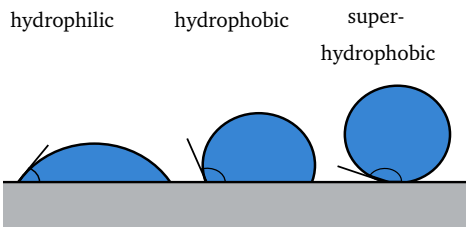

Figure 4: Different wetting domains

angle at the contact line of the three phases (gas, liquid, solid), called the contact angle θ (Figure 3). According to the contact angle we can distinguish between hydrophilic ($\theta < 90°$) and hydrophobic ($\theta > 90°$) or even super-hydrophobic domains ($\theta > 150°$) (Figure 4)[13]. Also the term superhydrophilictiy is being used for surfaces with contact angles close to zero, although a common definition

has not yet been established [14]. A super-hydrophilic surface will create a thin film that spreads fast over a large area, while for super-hydrophobic surfaces the drop almost takes the form of a sphere and will roll off easily in case of a tilted substrate. The contact angle depends on the forces acting on the three-phase contact line. In Figure 3 one can see the three surface tensions γ_{SG}, γ_{SL}, γ_{LG} at the solid-gas, solid-liquid and liquid-gas interface respectively[13]. For a drop in equilibrium on a flat, inert, chemically homogeneous plate Young's relation can be derived:

$$\cos\theta_E = \frac{\gamma_{SG} - \gamma_{SL}}{\gamma_{LG}}, \tag{2}$$

where θ_E is the equilibrium contact angle[13].
Additional relations have been proposed for the cases not applying to these restrictions:

1. For a chemically heterogeneous surface the Cassie-Baxter relation applies. For a surface composed of two different species with θ_1 and θ_2 it can be shown that:

$$\cos\theta_{app} = f_1 \cos\theta_1 + f_2 \cos\theta_2, \tag{3}$$

   where θ_{app} denotes the apparent contact angle, f_1 the surface area fraction of species 1 and f_2 the surface area fraction of species 2.

2. For a rough surface there are two possible states (Figure 5):

   a) The Wenzel state: The liquid fully wets the complete surface and the Wenzel relation can be used:

$$\cos\theta_{app} = r \cos\theta_E, \tag{4}$$

   where r denotes the roughness of the surface. This leads to a higher apparent contact angle θ_{app} for $\theta_E < 90°$ and a lower apparent contact angle for $\theta_E > 90°$ compared to the Young's angle θ_E, because $r > 1$. That means, that roughness in the Wenzel state reinforces the wetting behaviour.

   b) The Cassie-Baxter state: The liquid only partially wets the surface and air is trapped in pockets between the liquid and the solid. This can create super-hydrophobic surfaces and is sometimes called the Lotus Effect as it was observed that the Lotus leaf displays high water-repellency due to micro-roughness creating a Cassie-Baxter state. The Cassie-Baxter relation applies here as well, interpreting the air pockets as surface fraction with a contact angle of 180°.

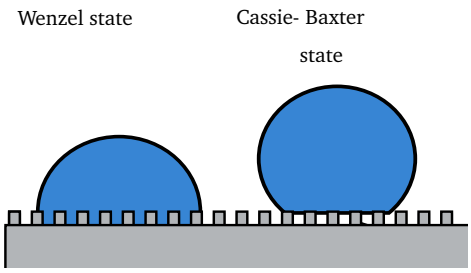

Figure 5: Different wetting domains on rough surfaces

2.2 Contact angle hysteresis

For non-ideal surfaces, i.e. for real surfaces, not one single contact angle can be observed as predicted by Young's relation, but rather the observed static contact angle varies between two limiting angles. Theoretical calculations show that there are actually a number of metastable states for hetereogenous or rough surfaces, separated by energy barriers [15, 16]. Experiments confirm these findings and show that the contact angle depends on the way of deposition and whether the interface has been recently advanced or recessed [1]. This is known as the contact angle hysteresis (CAH). Therefore, usually a range of angles is determined limited by the maximum (advancing) and a minimum(receding) contact angle to characterise this behaviour. The CAH is caluclated as their difference.
Intents to relate the experimental static contact angles to the Young's angle have been made, for example by applying vibration to the surface and droplet to overcome the energy barriers and reduce the static hysteresis. Decker et al. [17] were able to show that by vibrating the surface, after advancing or receding the contact line, the CAH can be decreased, supporting the theory of metastable states separated by energy barriers. Surface effects such as surface roughness or heterogeneity are commonly assumed to be the main causes of the CAH [18]. But the hysteresis can also have other causes as for example liquid adsorption, or a liquid film left behind the receding line [19], reaction of liquid and surface [20] or other forms of adaptation of the surface to the contacting liquid phase [8]. These cases have been investigated less and are often not considered in discussions about the CAH [21, 18, 17].

2.3 Dynamic contact angles

So far only the contact angle of a static drop was discussed. The contact angle of a moving drop depends on the contact line velocity [1]. The advancing contact angle increases in most cases while the receding contact angle decreases[1]. That means that an increasing hysteresis between the two angles is created for an increasing velocity of the drop(Figure 6). Hysteresis can therefore be defined as the sum of a static and a dynamic component.

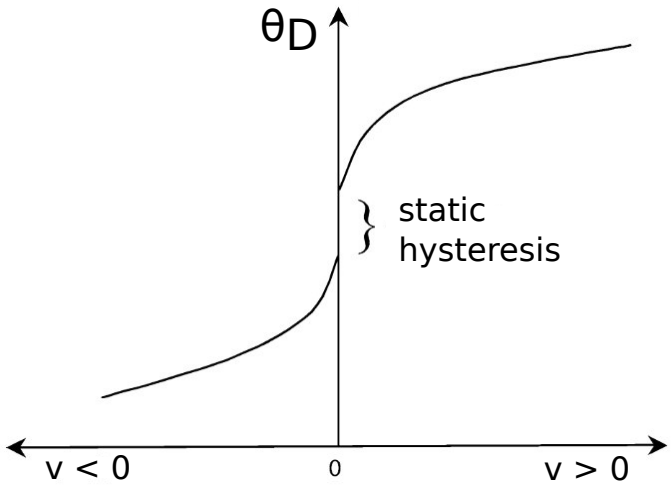

Figure 6: Dependence of the contact angle on contact line velocity v and the static CAH. Adapted from[1].

To quantify CAH experimentally mostly three different methods have been implemented, sometimes without clear differentiation between their characteristics. Eral et el. [18] presented a review of the different methods upon which the following section is based. The three methods are:

1. The sessile drop or inflating drop method, for which the liquid is pumped into and out of a sessile drop. By this, the advancing and receding angle of the moving contact line can be measured. A problem of the sessile drop method is the need for the immersed needle which changes drop shape, especially for small droplets. That can lead to changed observed contact angles. Furthermore, it is not always distinguished between quasi-static measurements of a moving contact line and true static CAH of a recently moved contact line, that had time to relax [22, 23].

2. For the tilted plate method a drop is deposited on a plate, which is then tilted. The lower and the upper contact angles are measured when the drop is on the verge of sliding because of gravity surpassing the resisting force. The angles at the cricital inclination measure therefore a static CAH. Similar to this is the centrifugal plate method, for which gravity is replaced by centrifugal force. For the tilted plate, Pierce et al. [24] found that the way of droplet deposition can affect the minimum angle for droplet sliding resulting in errors of up to 60%.

3. The Wilhelmy method, for which a surface is dipped into or pulled out of a liquid while the forces are measured and from this, the dynamic advancing and receding contact angles are deduced. The Wilhelmy plate has the disadvantage of the need for a substrate that has the same surface on all sides and of indirect contact angle measurement by measuring the force but the advantage of averaging over the surface.

While for the sessile drop method the droplet sits on a horizontal plane and is of approximately symmetrical shape, in contrast a droplet sitting on a tilted plane is of asymmetric shape with distinct contact angles at the lower (leading edge) and the upper part (trailing edge) of the drop. Krasovitski et al. argued that the maximum and minimum angle for the tilted plate and the advancing and receding angle of the sessile drop method measure different quantities, although they can be similar [25]. Pierce et al. found in experiments differences of more than 70° for receding compared to upper angles. To quantify CAH no uniform definition has been found and therefore great caution is needed when comparing measurements from different methods. Although this fact has been emphasised repeatedly [25], [24], [26] still these angles are sometimes not distinguished [27].
For a clear differentiation of the different angles the following denotation will be used:

1. θ_A^∞, θ_R^∞ for the static advancing (recently advanced) and receding (recently receded) contact angle.

2. θ_A*, θ_R* for the quasi-static advancing and receding contact angle measured by slowly inflating and deflating a sessile drop with the objective of substrate characterisation.

3. θ_{max}, θ_{min} for the static contact angle on the rear and front of a drop on a tilted plate before the drop starts sliding (at the sliding angle α_c).

4. $\theta_A(v)$, $\theta_R(v)$ for the dynamic contact angles measured for a moving drop at the front and rear side on a tilted plate.

The term hysteresis will be used for all four cases as the difference between the two respective angles. The drop sitting on an inclined plate is pulled down by gravity but is held in place by the CAH[18]. As mentioned, the droplet is asymmetric and the different curvature at the top and the bottom results in a pressure difference (Laplace pressure). The static CAH creates a resisting force that can prevent the droplet from moving, the adhesion force [18]. The lateral adhesion force was found to be proportional to the surface tension, the length of the three-phase contact line (i.e. the shape of the droplet), and the difference in the cosines of the contact angles at the leading and trailing edge [28]. ElSherbini and Jacobi derived for this retarding force :

$$F_{Adh} = \frac{24}{\pi^3}\gamma D(\cos\theta_{min} - \cos\theta_{max}), \tag{5}$$

where D is the diameter of a circle with an area equivalent to the drop's contact area.

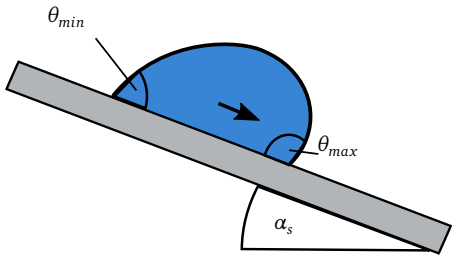

Figure 7: Drop on an incline at critical angle α_c starts moving

When the plane reaches a critical inclination the gravity surpasses the resisting forces and the drop starts to move (Figure 7). For the critical sliding angle α_c the following relation can be deduced from (5):

$$\rho V g \sin\alpha_c = \frac{24}{\pi^3}\gamma D(\cos\theta_{min} - \cos\theta_{max}) \tag{6}$$

with gravitational acceleration g and density liquid ρ.
When the drop starts to move, the dynamic part of the CAH becomes relevant [18]. Therefore, for the sessile drop method, where a droplet is inflated and the contact line is moving, it is important to use slow contact line velocities and report them together with the angle measurements. Sometimes it is stated, that for low speeds the contact angles show no velocity dependence [29], but that is not generally true. Velocity dependence has been reported even for very low velocities in the order of μm/s[30]. The dynamic component of hysteresis results from the interplay of the liquid's motion with the solid [18]. Different models have been proposed by researchers to explain and quantify the dynamic effects. Two approaches are mainly discussed in literature: hydrodynamic theory and molecular kinetic theory. Also, combinations of the two approaches have been proposed by Petrov and Petrov [31] and De Ruijter [32], as well as alternative approaches as for example the one proposed by Shikhmurzaev [33], combining hydrodynamics and non-equilibrium thermodynamics and implementing dissipation by the creation and destruction of interface at the contact line.
Blake presented a brief overview of the proposed theories in [1], upon which the following two sections are based. The most common theories, namely the hydrodynamic theory and MKT, are explained in Section 2.3.1 and 2.3.2. This is followed by a quick review and comparison to other theories in Section 2.3.3. An additional theory for taking adaptive processes into consideration was proposed by Butt et al. and is explained in Section 2.4. Here I also discuss the possibility of combining the adaptive theory with the hydrodynamic and molecular kinetic theory.

2.3.1 Hydrodynamic theory

The dynamic wetting process is a dissipative process. In the hydrodynamic theory the dissipation is assumed to be viscous. For the hydrodynamic approach the problem is divided into three scales: the microscopic scale, the mesoscopic scale and the macroscopic scale. The angle observed experimentally is macroscopic and explained by viscous bending of the moving liquid-gas interface, while the microscopic angle differs and is mostly assumed to be constant and equal to the equilibrium angle because of governing inter-molecular forces. Figure 8 depicts this schematically. A problem occurring

when applying the classic continuum fluid dynamic theory to wetting phenomena is that the no-slip condition cannot hold. This condition states, that the velocity of a fluid at an interface with a solid has the same velocity as the solid, i.e. does not slip. This is of course not true for the case of moving contact lines and would lead to unlimited stress in the vicinity of the contact line. As a result various methods have been proposed to solve the singularity, for example by introduction of slip (Navier slip, nonlinear slip) or a precursor film.

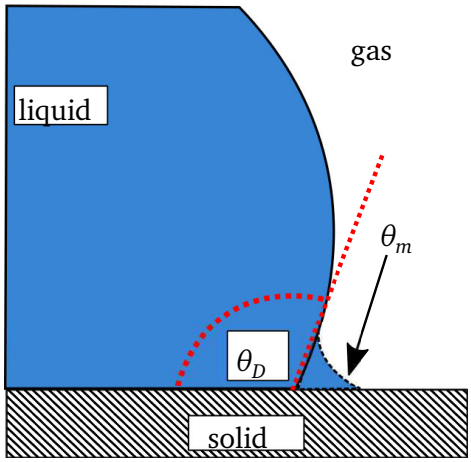

Figure 8: Macroscopic dynamic and microscopic contact angle in hydrodynamic theory. Microscopic angle is over-proportional in size for illustration. Based on [1].

Assumptions for the hydrodynamic approach are a capillary number of $Ca < 0.1$, negligible inertial effects (low Reynolds number) and ideal surfaces without static hysteresis [34]. The capillary number (Ca) is the dimensionless velocity and characterises the ratio of viscous drag to surface tension forces:

$$Ca = \frac{v\eta}{\gamma_{LG}} \tag{7}$$

with dynamic viscosity of the liquid η and contact line velocity v. On the mesoscale, viscous bending and a balance of viscous and surface tension forces govern the shape of the gas-liquid interface. The macroscopic contact angle is determined by using matched asymptotic expansions to solve the flow equations in the different scales. The hydrodynamic theory for dynamic contact angles in its most common form is

$$\theta(v)^3 - {\theta_m}^3 = 9\,Ca\,\ln(\frac{L_v}{L_s}), \tag{8}$$

where L_v and L_s are macroscopic and microscopic length scales respectively and θ_m is the microscopic contact angle, usually assumed to be equal to the equilibrium Young's angle θ^∞. The microscopic length scale L_s is the slip length, necessary to remove the mentioned singularity and is determined by fitting Equation 8 to experimental data, as measuring it is impossible. The fitting sometimes leads to unphysical submolecular slip-lengths, indicating that the model is not complete or at least not universally valid. One reason might be that the microscopic contact angle may also be velocity dependent.

2.3.2 Molecular kinetic theory

The molecular-kinetic theory (MKT) assumes the dynamic CAH to be governed by adsorption/desorption processes in the three-phase zone. The dissipation channel for this theory is friction at the contact line. For the MKT, two new parameters are specified to describe the processes on the molecular scale:

the quasi-equilibrium frequency of the statistical molecular jumps and the average displacement, being the distance of adsorption sites on the surface. A schematic of this process can be seen in Figure 9. The frequency for solid-liquid interactions $\kappa_{0,s}$ can be written as function of the activation free energy of wetting $\Delta G_w^\star$:

$$\kappa_{0,s} = \frac{k_B T}{h} \exp \frac{-\Delta G_w^\star}{N k_B T}, \tag{9}$$

where k_B is the Boltzmann constant, h the Planck constant and N the Avogadro number. The original version of the MKT did not include viscous effects[35], but later a modified frequency κ_0 was proposed:

$$\kappa_0 = \frac{\kappa_{0,s} h}{\eta \nu_m} \tag{10}$$

where η is the dynamic viscosity and ν_m the molecular flow volume. Furthermore, a relation between increasing work of adhesion W_{Adh} and increasing frequency was found:

$$\kappa_0 \sim \frac{k_B T}{\eta \nu_m} \exp(-W_{Adh}). \tag{11}$$

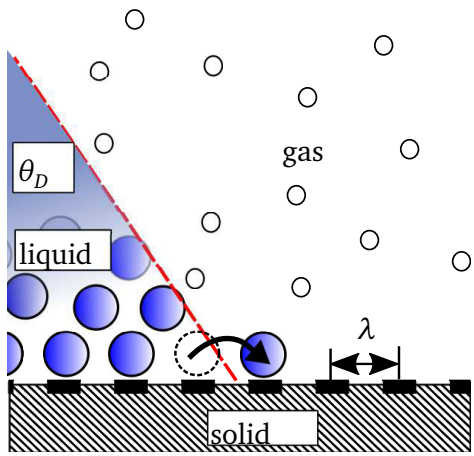

Figure 9: Schematic view of a molecule hopping from one adsorption side to another over distance λ. Based on [1]

Under equilibrium the adsorption/desorption process is equally probable in the forward and backward direction because of equal energy barriers. When a force is applied to move the contact line the equilibrium of the adsorption processes is disturbed and jumps into one direction become more probable. This driving force is equal to the out-of-balance surface tension force and the MKT is described by the following equation:

$$v = 2\kappa_0 \lambda \sinh[\gamma_{LG}(\cos\theta^\infty - \cos\theta(v))\frac{\lambda^2}{2k_B T}] \tag{12}$$

in which v is the velocity of the contact line, λ the distance of adsorption sites on the surface and T the absolute temperature. For receding contact angles the sign of the velocity is negative. In practice, the unknown parameters can only be fitted. Usually they are plausibly found to be in molecular range for the distance of adsorption sites λ, and vary between Kilohertz to Gigahertz for the quasi-equilibrium frequency κ_0. This model does not take viscous bending into account and the contact angle in Equation (12) can be interpreted as the microscopic contact angle.

So far no consensus has been found and the theories are mostly limited to small Capillary and Reynolds numbers as well as flat surfaces [1]. Moreover, the common approaches model the contact angle only as a function of the contact line speed and material properties, but it was shown by Clarke et al. that the flow field in the liquid also affects the dynamic contact angle [36]. That is a fact that has been taken into consideration neither by the MKT nor by hydrodynamic theory and will probably lead to new models or adaptations in the near future. Blake et al. proposed a model for a 'hydrodynamic assist' to explain this observations. The approach is that during forced wetting the shear stress can assist the surface tension and reduce velocity dependence [37].

Another controversial point of proposed models is the relation of microscopic and macroscopic contact angle. In 2014, a study on this topic was published by Chen et al. [38]. They observed a convex nanobending of the interface close to the three-phase contact line for partially wetting liquids. This was found by studying the interface of a liquid drop by tapping mode atomic force microscopy (TM-AFM). Due to the convex bending different contact angles can be measured locally depending on the distance from the solid. From the measured interface profile, local angles have been calculated at 4nm, 10nm and 100nm distance from the surface and for different, low speeds ($\leq 30\frac{nm}{s}$). Both, bending curvature and local contact angles increase with velocity. For the static case, the contact angles have the same values. But for dynamic cases the contact angles closer to the contact line were found to be more dependent on velocity, and therefore to be higher. The hydrodynamic theory cannot explain that, because here usually the microscopic contact angle is assumed to be constant. MKT was able to fit the contact angles for each location over v. But for each local contact angle other fitting parameters were necessary. Furthermore, MKT does not include bending, as the hydrodynamic theory does. Chen proposes that a microscopic contact angle on the nanoscale is followed by the convex bending where a mesoscopic contact angle can be measured and on a larger macroscopic scale by a concave viscous bending where the macroscopic angle can be measured.

Based on these findings, recently a theory was submitted by Wang and Chen [39, 40] that claims to be a general model over the full range of contact line velocities with unprecedented fitting performance. The idea is based on the hydrodynamic theory but replaces the constant microscopic contact angle by a velocity dependent mesoscopic angle $\Theta_{me}(v)$. This angle is calculated from a force balance of the driving force and a velocity dependent friction force $\gamma_{SG}(cos\Theta(0) - cos\Theta_{me}(v)) = \zeta v$, with friction coefficient ζ. Up to here, the model is equivalent to the linearised version of the Petrov combination of hydrodynamic theory with MKT [31]. The novelty is the definition of the mescoscopic friction coefficient ζ by a velocity dependent empirical correlation. At a critical velocity, Wang and Chen predict a strong decrease in friction due to rolling motion, slippage and air entailment. By this, non-monotonous contact angles can be explained, that show a transition to a lower contact angle at high velocities. The only experimental data provided for this transition was taken from Blake et al. [20]. Also, the study lacks a physical explanation of the newly introduced empirical parameters. The good fitting performance is not very surprising as the model is basically a combination of the well-fitting hydrodynamic theory and MKT, similar to Petrov and Petrov. The fact, that the model can represent transitions is interesting but requires further experimental proof. The necessity of parameter fitting and the lack of the flow field influence remain also for this model.

Seveno et al. carried out an extensive analysis of the most important dynamic contact angle theories, namely the hydrodynamic theory, molecular-kinetic theory, their combination by Petrov and De Ruijter and a simplified version of Shikhmurzaev's theory [41]. Fitting results for dynamic contact angles on silica surfaces and PET were compared. The Petrov model resulted in physically not realistic parameters for multiple experiments. Also it was criticised to contain over-parametrisation, because of the large number of unknown parameters. Hydrodynamic and molecular kinetic theory both were able to represent most data well, and with physically acceptable parameters, although hydrodynamic

theory, as was to expect, seemed to fit better for the experiments with viscous liquids and MKT for the less viscous liquids. Shikhmurzaev's formula showed slightly higher errors. But this could also result from the simplification carried out for the comparison. The authors concluded, that it is difficult to define one model as the most appropriate. Still, the existing contact angle models can represent most data well. Therefore they may, understanding their limits, be used for cautious analysis of the dynamic of contact angles.
An aspect not taken into account by these theories is the possible change of surface properties induced by the contact with the liquid. These changes, or adaptations, will be examined in the next section.

2.4 Adaptive wetting

MKT and hydrodynamic theory are defined for ideal and smooth surfaces with one equilibrium angle for the static case. In reality surfaces exhibit static CAH and multiple metastable static contact angles. As mentioned in Section 2.2 the CAH is typically described to be caused by chemical heterogeneity or roughness of the surface, but can also be a consequence of molecular interactions of liquid and solid (such as hydrogen bonding) [21] or a change of the surface properties induced by an external force or process. Another way to interpret this is the one used by Tretinnikov who distinguishes between thermodynamic and kinetic hysteresis[11]. The thermodynamic hysteresis is described to be caused by roughness and heterogeneity of the surface while kinetic hysteresis is attributed to time- or rate-dependent processes such as the swelling of the substrate or reorientation of functional groups in the surface [11]. These are examples for surfaces adapting to the surrounding phase and can therefore be called adaptive surfaces. Some other examples for adaptive processes are polymer reconstruction, selective swelling of mixed polymer brushes, recovery of treated PDMS, reconstruction of organic monolayers, replacement of contamination/adsorption layers, ordering of liquid molecules, adsorption of surfactants to the surface or the formation of an electric double layer [8]. Adaptive processes can affect the interfacial energy of the solid and thereby the contact angles. Although adaptive surfaces have been investigated before, the common theories for dynamic contact angles do not account for this kind of adaptive behaviour and for that reason an adaptive wetting theory was proposed by Butt et al. [8]. In the following, a review of previously published studies on adaptive wetting is presented, and thereafter the mentioned adaptive theory is explained.

2.4.1 State of the art

Adaptive surfaces have been studied for several decades with the objective to design materials in a way that they can respond to a number of situations that require distinct surface properties. Luzinov et al. 2004 published a detailed overview of the investigations done on adaptive surfaces [42]. Most studies have investigated the physical phenomena of the adaptation processes for a specific material. Usually, contact angle measurements have only been implemented for the characterization of surface properties and in most cases have been limited to equilibrium angles or (quasi-)static hysteresis. In the following, a review of a selection of studies published on adaptive surfaces is presented. The focus lies on studies that either cover aspects of dynamic contact angles and dynamic or static CAH or propose some kind of quantitative model or equation to describe the effect of the adaptive process on the contact angle.
One early example of investigation on contact angle adaptation by surface reconstruction and recovery of treated polymers is the work of Yasuda et al. from 1981, who studied the relation of molecular reorientation and contact angle hysteresis [43]. When macromolecules have both hydrophobic and hydrophilic functional groups, the molecules near the surface try to change their orientation depending on the surrounding phase. The wettability therefore not only depends on the chemical configuration of the surface molecules but also on their orientation. When in contact with water, the macromolecules, if mobile, reorientate and hydrophilic groups move to the surface because of their interaction with the water. Whereas, if the surface is in contact with dry air, the polar groups can be buried. Yasuda

et al. showed that oxygen-plasma-treated hydrophobic surfaces exposed to air display a decay of wettability over time, which is dependent on the degree of cross-linking. One of the main reasons for this is the thermodynamically favourable reorientation of hydrophilic groups, that were created at the surface by the plasma treatment, towards the bulk [44]. For higher degrees of cross-linking the mobility of surface macromolecules is smaller and therefore their rearrangement takes longer. While for these surfaces the reorientation of functional groups takes days, Yasuda et al. assumed that for hydrogels the rotation of molecules is faster than the time required for contact angle measurements. Furthermore, they stated that high hysteresis of polymer surfaces containing hydrophilic functional groups is caused primarily by the high mobility of surface molecules. The advancing contact line passes over a dry surface with buried hydrophilic groups, while the receding contact line passes over a surface with a rearranged surface configuration. Already Good et al. found 1978 that molecular orientation has an influence on the CAH of polymers [45].

Tretinnikov et al. studied the dynamic wetting of polymer surfaces by the Wilhelmy balance method and found for some polymers that the receding angles are time-dependent [11]. The authors assume that this is caused by reorientation of hydrophobic and hydrophilic groups in the surface when in contact with water. This work stands out as additionally different immersion speeds were tested finding increasing advancing and decreasing receding contact angles for poly(ethylene terephthalate) (PET), nylon 6 and poly(ether urethane)(PU) at increasing speeds. For the other surfaces that were tested no velocity dependency was found. As the investigated velocities were very low (<50 mm/min) viscous effects on the contact angle were assumed to be negligible and the findings were explained by surface adaptation of PET, nylon 6 and PU. The velocity dependency was attributed to the fact, that at higher speeds the surface adaptation, i.e. the reorientation, cannot equilibrate fully before the contact line passes. Depending on the contact line velocity intermediate states lead to different contact angles.

Schmidt et al. investigated the adhesive and marine biofouling properties of polymers [27]. Results indicate that the CAH is dependent on the time of exposure to the test liquid. A strong correlation between higher cross-linking density and low contact angle hysteresis was found. This is because the increased cross-linking results in stronger immobilization of surface molecules and higher resistance to liquid penetration.

An interesting work on dynamic wetting of responsive surfaces over wide speed ranges was done by Blake et al., who experimentally studied the advancing contact angles during reactive wetting of water on gelatin-coated poly(ethylene terephthalate)[20]. The wetting behaviour shows two modes with a smooth transition, which is attributed to the change of wettability caused by the reaction of the surface with water. For slow wetting velocities the reaction has time enough to change the substrate from hydrophobic to hydrophilic, while at high velocities the contact angles show hydrophobic characteristics. The data was analysed using the MKT with different fitting parameters for the two respective modes. The transition was found to be of zeroth-order kinetics. Noteworthy is also the experimental method to investigate the dynamic advancing contact angles, which consists in a coated tape that is entered into the liquid vertically at variable speed, allowing speeds of up to 10 m/s. No receding angles were measured and the effect of reactive wetting on CAH is not discussed. Furthermore, in contrast to the previously mentioned adaptation processes, the chemical reaction is only allowing one-directional change of surface properties as the retraction of liquid will not return the tape to its original state.

Another bi-directional adaptive process is imbibition of a liquid into the substrate, for example the swelling of a polymer. Lam tested wetting of FC-732-coated surfaces by liquids with different molecule chain lengths and found that smaller molecules lead to higher hysteresis [46]. The explanation provided is that liquid sorption or retention causes hysteresis and thus an easier penetration into the polymer surface by shorter molecules leads to higher hysteresis.

Grundke et al. showed by variable angle spectroscopic ellipsometry that for smooth polyimide films in contact with water over time advancing and receding contact angle decrease [12]. This was attributed to swelling and polymer reorientation. Also, a thickness increase by 10nm consisting of 98.6 % polyamide and 1.4% water was measured.
Minko et al. produced adaptive surfaces consisting of a rough needle-like polymer structure of micrometre size coated with a mixed polymer brush [9]. Brushes are chains of polymers that are anchored to the substrate at one end and according to brush density and surrounding solvent can either stretch or collapse. A more detailed explanation will be given in Section 3.5.3. The brush structure used by Minko et al. reversibly switches when in contact with different solvents. This collapses or swells one component of the brush and results in a change of surface properties. The microscopic structure is used to amplify hydrophilic and hydrophobic states as explained by the Wenzel equation. It was shown that the surface switches to hydrophobic by exposure to toluene and switches back when in contact with acid water. The change takes several minutes switching the brushes to a hydrophilic state while also increasing the (quasi-static) CAH.
Hanni-Ciunel et al. studied the effect of film swelling on static contact angles for polyelectrolyte mono- and multilayers [47]. A decrease of contact angles of about 7° over time was observed for poly(styrene sulfonate) and attributed to a change in the swelling state of the coating. It can be represented by first-order kinetics. The equation is parametrised by a relaxation time and two contact angles, one for the initial state and one for the final equilibrium. The relaxation time was found to be rather slow with 50 minutes. From further experiments, it was also concluded that the swelling state differs for a coating in water-saturated atmosphere compared to a coating in direct contact with water. In evaporation experiments an increased evaporation velocity was found for poly(diallyl dimethylammonium chloride) which also exhibits a change in contact angle between ambient and water-saturated air. The change of surface free energy of the substrate due to swelling was calculated from the difference in contact angles in the two swelling states (water-saturated and ambient conditions). An explanation was proposed that the change in the surface free energy for swelling of coatings creates a driving force enhancing the imbibition of water into the substrate which in turn increases the evaporation speed.
Dupas et al. investigated the wetting of polymers by their solvents theoretically and experimentally [48]. When a hydro-soluble polymer is dried, the polymer's surface can restructure and apolar parts can segregate towards the surface increasing hydrophobicity. When wetted with water the contact angle decreases over time as the polymer becomes hydrated. It is known, that the contact angle depends on solvent concentration in the polymer[49]. This hydration is goverend by diffusion from the liquid into the polymer and by condensation of evaporated solvent onto the surface. It was calculated, that the uptake of water by condensation at a distance of a few micrometer decreases with contact line velocity and film thickness. When the contact line moves fast, the coating has less time to hydrate an thus is drier. The theoretical model for the description of the solvent activity in the film was not connected to theory for the contact angle but qualitative conclusions were made. Contact angles were measured on maltodextrin for different film thicknesses and contact line velocities. They are higher for high thicknesses and high velocities confirming that a lower concentration exists at the contact line. In a previous, related study it was calculated that the concentration profile in front of the contact line can decrease very sharply depending on the contact line velocity [50]. A molecular cut-off length was predicted at which the contact angle is determined. A model calculation showed a concentration decrease of up to 90% within the first 5 nm from the contact line. The results of the model calculations can be found in Figure 10.
In conclusion, many of the available studies on adaptive surfaces have focused on the physical processes of adaptation and implemented static contact angle measurements for surface characterization. A few studies additionally contain qualitative observations about the influence of surface adaptation on CAH [43], [45], [46]. Exceptions, to my best knowledge, are the work of Blake et al. - the only

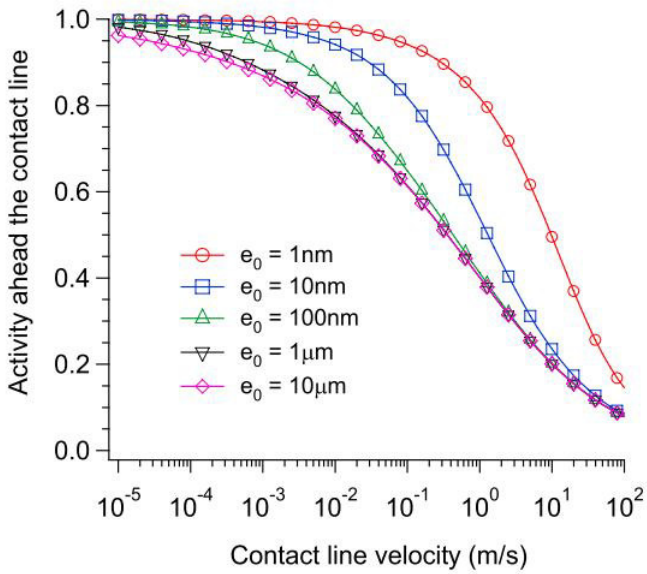

Figure 10: Model calculations for the velocity dependence of the water activity at $5\,\mathrm{nm}$ in front of the contact line for different initial thicknesses e_0. From [50]

one found to have investigated the influence of some kind of surface adaption (namely a reactive process) on dynamic contact angles over a wide speed range [20] - and Tretinnikov - who explicitly investigated the influence of low velocities on CAH for adaptive surfaces but did not propose a mathematical theory to describe it [11]. Zeroth-order and first-order kinetics have been proposed by Blake for dynamic contact angles in a reactive process [20] and by Hanni-Ciunel for static contact angles in a swelling process [47] respectively. But the first comprehensive theory on the dynamic contact angle hysteresis for adaptive surfaces was proposed in 2018 by Butt et al. This theory promises quantitative prediction of the contact angle depending on contact line velocity and will be explained in the following section.

2.4.2 Dynamic contact angles in adaptive wetting

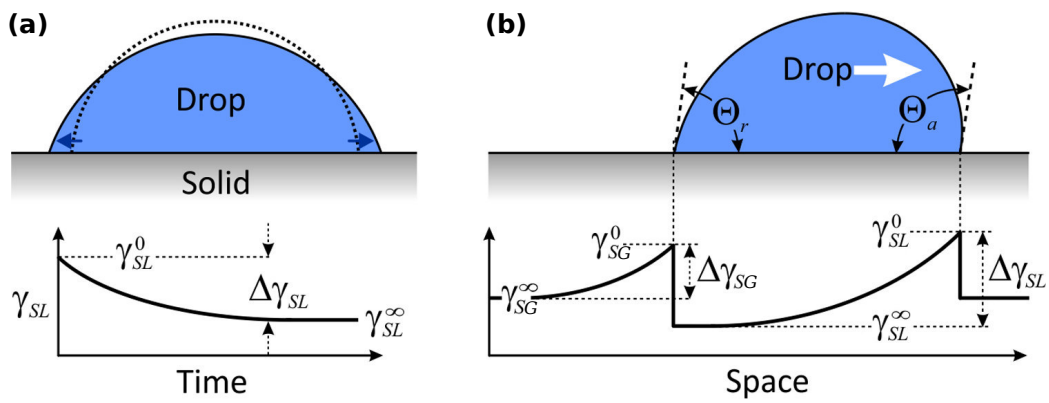

Figure 11: Interfacial energies for different drops. (a) shows the effect on the contact angle for a change of interface energy at the liquid-solid interface of a spreading drop. The dashed line indicates the initial state and the solid line the equilibrium state. Underneath the change of the interfacial energy γ_{SL} over time is depicted. (b) illustrates surface adaptation for a moving drop in steady state. The graph shows interfacial energies γ_{SL} and γ_{SA} over space. Figure and description adapted from [8].

Butt et al. proposed a theory based on Young's equation for adaptive surfaces governed by a change of interfacial energies. Excluded are reactive, corrosive or soluble surfaces as they cause multiple effects and normally change the topography. In the following, a brief overview of the deduction will be shown, for more details please consult [8]. Considering the Young's relation is defined for the equilibrium it can be formulated in the following manner:

$$\cos\theta_E^{\infty} = \frac{\gamma_{SG}^{\infty} - \gamma_{SL}^{\infty}}{\gamma_{LG}^{\infty}}, \tag{13}$$

where ∞ indicates the equilibrium state of the surface in contact with the liquid for $t \to \infty$. When a liquid gets into contact with the surface the initial liquid-solid interfacial energy γ_{SL}^{0} changes due to the adaptive process and will eventually reach equilibrium γ_{SL}^{∞}. The kinetics will depend on the specific process but for simplicity first order kinetics were assumed by Butt et al.:

$$\gamma_{SL}(t) = \gamma_{SL}^{\infty} + \Delta\gamma_{SL}\, e^{-t/\tau_{SL}}, \tag{14}$$

in which $\Delta\gamma_{SL} = \gamma_{SL}^{0} - \gamma_{SL}^{\infty}$ is the change of the interfacial energy from initial to equilibrium state and usually positive and τ_{SL} is the relaxation time of the adaptation at the solid-liquid interface. Figure 11a shows a schematic illustration of the change of the interfacial energies over time and its effect on the contact angle. The surface changes from a dry state to a wet state and saturates.
Figure 11b shows a moving drop on an adaptive surface. In this case at the rear side, where the liquid is receding, the drop has a different contact angle. This is due to the fact, that the receding contact line moves over an already changed surface configuration. At first, it is assumed that the receding contact line withdraws from a surface in the saturated wet state. For this, it has to be exposed sufficiently long to the liquid to reach equilibrium. At the point where the liquid recedes the saturated surface will be exposed to the gas. After time τ_{SG} the solid-gas interfacial energy transitions from the initial wet state to the equilibrium dry state. The new liquid-gas interface created at the receding side can also relax due to adsorption processes in time τ_{LG}. Both were also modelled by first-order kinetics:

$$\gamma_{SG}(t) = \gamma_{SG}^{\infty} + \Delta\gamma_{SG}\, e^{-t/\tau_{SG}} \tag{15}$$

$$\gamma_{LG}(t) = \gamma_{LG}^{\infty} + \Delta\gamma_{LG}\, e^{-t/\tau_{LG}} \tag{16}$$

In order to insert equations 14 - 16 into Young's relation a peripheral thickness l_{SL} was introduced in accordance with Hansen and Miotto [51]. It is the width of the contact region, that has an effect on the contact angle. The width depends on the specific nature of the interface and should be at least of the range of surface forces. Also, the thickness of the interface can be considered a measure of l_{SL} and ranges from a few molecules to multiple nanometres. This also agrees with Tay et al. who have calculated a strong velocity dependence of liquid concentration in polymer films within the first 5 nm in front of the contact line [50] (Figure 10). Butt et al. used $l_{SL} = 10$ nm as an educated guess.
The contact angle then depends on the velocity v of the moving contact line and the relation of l_{SL} and the adaptation time scales. For an advancing contact line moving over a dry substrate the solid-liquid surface energy adjusts and leads to a change in the contact angle:

$$\cos\theta_A(v) = \frac{\gamma_{SG}^{\infty} - \gamma_{SL}(t = l_{SL}/v)}{\gamma_{LG}^{\infty}} = \cos\theta^{\infty} - \frac{\Delta\gamma_{SL}}{\gamma_{LG}^{\infty}}\, e^{-l_{SL}/v\tau_{SL}}. \tag{17}$$

This relation neglects any dynamic effects, e.g. viscous dissipation, apart from the change of interface energy. For slow contact lines $v << l_{SL/\tau_{SL}}$ the adaptation process can equilibrate so that $\gamma_{SL}(t) \to \gamma_{SL}^{\infty}$ and $\theta_A(v) \to \theta^{\infty}$. For fast contact lines $v >> l_{SL/\tau_{SL}}$ the adaptation process cannot equilibrate and

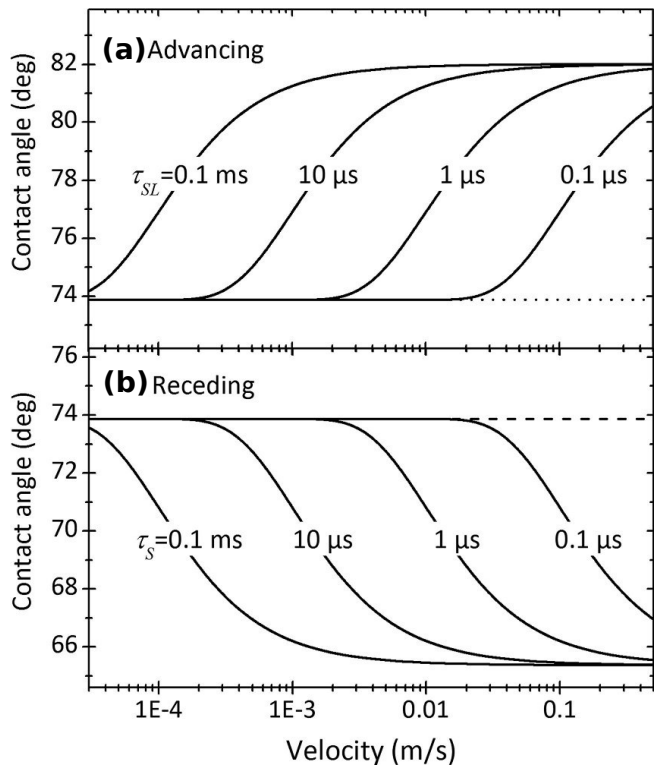

Figure 12: The dynamic contact angles of water at the advancing (a) and receding (b) contact line for different velocities and relaxation times. Calculated using $\gamma_{LG}^{\infty} = 0.072N/m, \gamma_{SG}^{\infty} = 0.06N/m, \gamma_{SL}^{\infty} = 0.04N/m, \Delta\gamma_{SL} = \Delta\gamma_{SG} = 0.01N/m$ and $l_{SL} = l_{SG} = 10nm$. Figure and description adapted from [8].

$\gamma_{SL}(t) \rightarrow \gamma_{SL}^{0}$. As $\Delta\gamma_{SL}$ is commonly positive [8] the contact angle will increase with increasing contact line velocity v.

In a similar way the dynamic receding contact angle can be calculated. As other relaxation processes govern the receding side a different peripheral length l_{SG} is used. It is assumed that the change of γ_{LG} can be neglected because the time scale for the liquid-gas interfacial energy is much smaller than for the gas interface $\tau_{LG} << \tau_{SG}$. For a contact line receding on a saturated wet surface results:

$$\cos\theta_R(v) = \cos\theta^{\infty} + \frac{\Delta\gamma_{SG}}{\gamma_{LG}^{\infty}}\, e^{-l_{SG}/v\tau_{SG}}. \tag{18}$$

In contrast to the advancing side, the receding angle decreases with increasing velocity. Figure 12 illustrates the relation of contact line velocity, adaptation time scales and contact angles. As velocity or adaptation time increases the $\theta_A(v)$ increases and $\theta_{D,d}$ decreases, resulting in increasing CAH. Equation 17 and 18 therefore show, that the adaptive processes amplify the usual dynamic behaviour of increasing CAH for increasing speeds, which are excluded here and commonly explained by MKT or hydrodynamic theory.

For the case of a moving drop the at the receding side it has to be considered, that the surface in contact with the liquid may not have enough time to equilibrate to the wet state before the receding contact line passes. Thus the assumption used for eq 18 that $\gamma_{SL} = \gamma_{SL}^{\infty}$ at the receding contact line is not always valid. Therefore for a moving drop can be shown that:

$$\cos\theta_R(v) = \cos\theta^{\infty} + \frac{\Delta\gamma_{SG}}{\gamma_{SG}^{\infty}}\, e^{-l_{SG}/v\tau_{SG}}(1 - e^{-L/v\tau_{SL}}) - \frac{\Delta\gamma_{SL}}{\gamma_{LG}^{\infty}}\, e^{-L/v\tau_{SL}} \tag{19}$$

with drop length L.
Three different velocity regimes were identified by Butt et al. :

- Low velocity ($v << l_{SG}/\tau_{SG}$, Figure 13a): All surface energies equilibrate and thus $\theta_R(v) = \theta^{\infty}$.
- Intermediate velocity ($l_{SG}/\tau_{SG} << v << L/\tau_{SL}$, with droplet length L , Figure 13b) : The solid-vapor surface at the receding side does not reach equilibrium and $\gamma_{SG} = \gamma^0_{SG}$. The liquid-solid interface equilibrates to the saturated wet state and therefore at the receding side $\gamma_{SL} = \gamma^{\infty}_{SL}$. This results in $\gamma_{LG} \cos\theta_R(v) \approx \gamma^0_{SG} - \gamma^{\infty}_{SL}$.
- High velocity ($L/\tau_{SL} << v$, Figure 13c): When v is high enough to impede any adaptation that means that the receding contact line moves over a dry-state substrate so that $\gamma_{SG} \to \gamma^{\infty}_{SG}$.

The three regimes can be related to three surface states. In regime one, the solid-liquid interface is in an equilibrated wet state, while the solid-gas interface is in an equilibrated dry state. In regime two, both interfaces are in the wet state. And in regime three both interfaces are in the dry state. In between these regimes, velocity dependent transitions happen. Figure 14 shows $\theta_R(v)$ for the three regimes and their transitions. In between the last two velocity regimes the liquid-solid interface does not reach the saturated wet state and the receding contact line passes over a partially adapted surface. That interestingly leads to an increasing $\theta_R(v)$ with increasing v. This would then even result in $\theta_R(v) \to \theta_A(v)$, for the model calculation as a consequence of neglecting other dynamic effects for this theory.

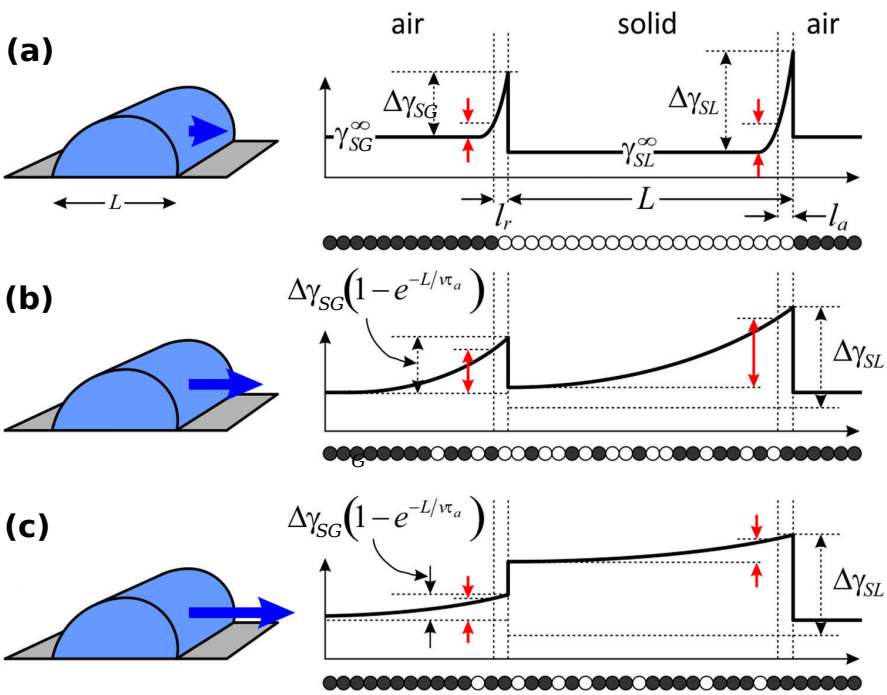

Figure 13: Interfacial energies for a two-dimensional drop moving at different velocities: low (a), intermediate (b) and high (c). The red arrows show the energy dissipated per unit length. The circles indicate a typical set of surface molecules in the wet (white circles) or dry (black circles) state. In this figure, it is assumed that $\gamma^{\infty}_{SG} > \gamma^{\infty}_{SL}$. Figure and description adapted from [8].

The adaptive wetting theory only models the contact angle dynamics caused by the change of the surface energies. In reality, these processes will coincide with other dynamic phenomena described by hydrodynamic or molecular-kinetic theory. Hydrodynamics, for example, predict an increasing dynamic CAH for increasing drop velocity because of viscous dissipation, which will be amplified by

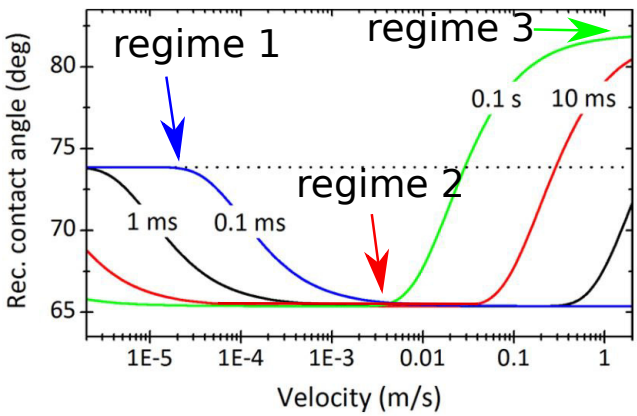

Figure 14: Dynamic receding contact angle of a moving twodimensional drop. Figure and description adapted from [8]. The indication of the three regimes was added.

the adaptation-caused CAH. In order to model the interplay Butt et al. proposed the combination of common dynamic contact angle models with adaptive wetting theory. It is suggested to replace $\cos\theta_m$ in eq 8 and $\cos\theta^\infty$ in eq 12 by $\cos\theta_A(v)$ from eq 17 for advancing angles and $\cos\theta_R(v)$ from eq 18 or 19 for receding angles.

The adaptive wetting theory is the base for my thesis. For investigation of the predicted behaviour, dynamic contact angle measurements over multiples orders of velocities have to be measured.

Table 1: Comparison of different setups for velocity dependent contact angle studies

goniometer/ tilted plate	Wilhelmy plate	inflating drop
+ wide velocity range	+ wide velocity range	- for small velocities mostly
+ no motor needed	- motor needed	+ no motor needed
+ simultaneous measurement of $\Theta_R(v)$ and $\Theta_A(v)$	- $\Theta_R(v)$ or $\Theta_A(v)$ measured	- $\Theta_R(v)$ or $\Theta_A(v)$ measured
- restriction to surfaces with low to medium adhesion	+ even highly adhesive surfaces	+ even highly adhesive surfaces

3 Experimental setup

In order to measure dynamic contact angles in dependence of velocity, a suitable setup is required. For this reason, a goniometer was built, which allows measuring the contact angles of sliding drops on different inclinations. A high-speed camera records the moving drops and by analysis of the videos the contact angles are extracted. In Section 3.1 the choice of the experimental setup will be explained and its mechanics are discussed. In Section 3.2 the optical system implemented in the setup is presented and in Section 3.3 details about the video analysis software are given. A quick explanation of the measurement routine can be found in Section 3.4. Section 3.5 covers the choice and synthesis of the surfaces used to test the functionality of the setup.

3.1 Mechanical system

To measure dynamic contact angles, different configurations are possible (Section 2.3): inflating drop method, Whilhelmy plate or a tilted plate. With respect to the aim of this work some additional aspects have to be considered when choosing one method. An overview of the advantages and disadvantages of the three methods for measuring dynamic contact angles can be found in Table 1. For the inflating drop, the contact line velocity depends on the drop size and the volume flow into the drop. A disadvantage of that kind of setup is the limited velocity range and difficulty to accomplish a constant velocity. For the available DataPhysics OCA 35 the resulting maximum velocity is in the order of $v \sim 1$mm/s. Furthermore, the inflating drop method and the Wilhelmy plate do not allow to measure the receding and advancing contact angle at the same time. However, the choice of a goniometer, or tiltable plate, promises a simple construction, easy change of several experimental parameters as rolling distance and tilt angle and the possibility to measure receding and advancing angle at the same time. Because of these advantages, it was decided to construct a setup using a tiltable plate. A drawback is the necessity of drop sliding, making the measurement on surfaces that have too high static CAH impossible. But by changing the drop weight, still a wide range of surfaces can be tested. According to the planned experiments, the following demands should be met by the setup:

1. A high-speed camera is required in order to be able to analyse speeds of more than 20 cm/s.
2. The sample has to be tiltable continuously from 0° up to 90° for changing the magnitude of drop velocity.
3. The distance between drop deposition and camera should be variable, to be able to measure at a distance where the drop has reached steady-state velocity.
4. Easy adjustment of the two previous settings should be able in order to facilitate the measurement's workflow.

One way to facilitate inclination change without having to adjust the light source and camera every time would be the construction of a complete tilting framework, where sample holder, camera and

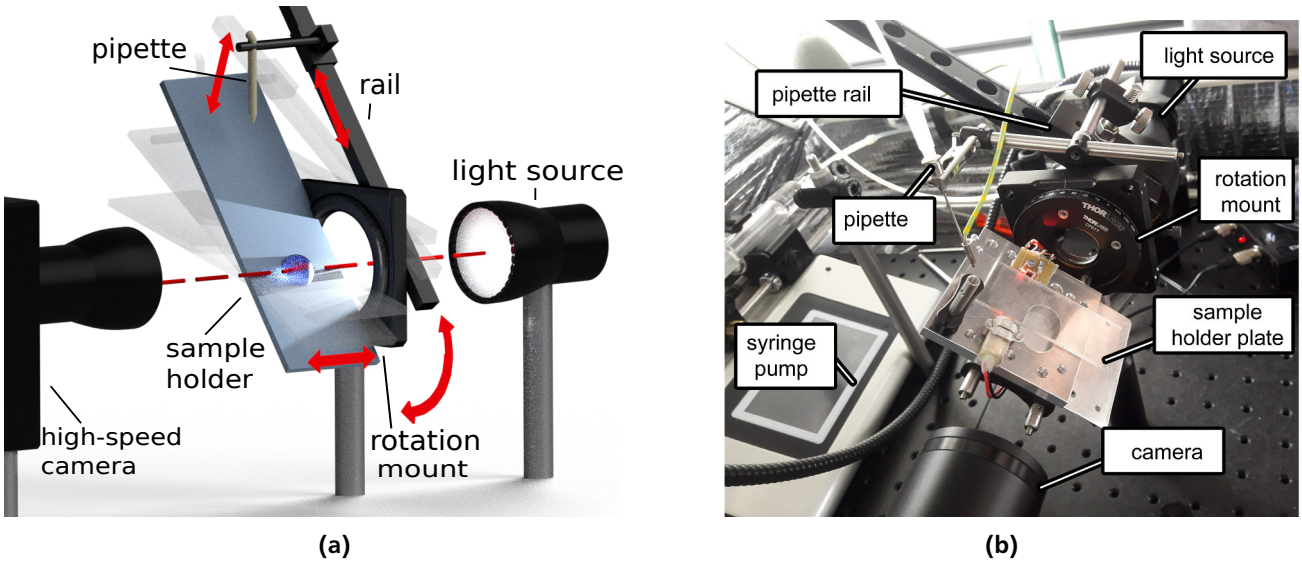

Figure 15: Picture (a) shows a schematic illustration of the experimental setup and the degrees of freedom. The red line marks the rotational axis. Picture (b) shows a photo of the final setup.

light source are mounted on a tiltable platform. A simpler and much more cost efficient way is to have just a rotation mount for the sample holder. By designing the setup in a way that the droplet can be filmed when passing the rotational axis of the tilting mechanism, the camera and light source can be fixed at a permanent position (Figure 15a) and do not need to be readjusted. For the variation of the drop rolling distance, the pipette is attached to a sliding rail. The sample holder plate is also mounted on rails, so that for a fixed pipette position different lateral points on a sample can be tested without having to adjust the camera and pipette. The final setup can be seen in Figure 15b. The camera is mounted on a Manfrotto sliding rail, making the working distance easily adaptable as well.

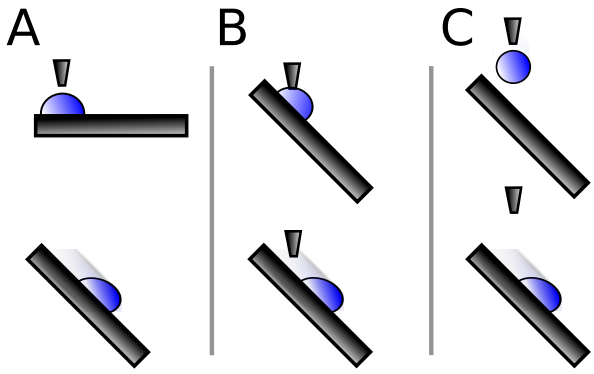

Figure 16: Three different ways to deposit the drop. A: Depositing on a horizontal plane and then tilting it. B: Filling up on the tilted plate until the drop detaches. C: Dropping the liquid from a small height

As pipette a metal needle is used, that is connected to a 20ml glass syringe via a Teflon tube. All three parts were rinsed with acetone and deionised water before the first use. The syringe is mounted in a kdScientific syringe pump. Three different placement methods for the drop are possible (Figure 16). First, placing the drop on the horizontal surface before tilting it to the desired angle. This method is difficult for high angles, as the tilting has to be very fast in order to reach the desired angle before the drop has passed the whole sample. This would add additional effects due to different tilting speeds, as it needs to be done manually. Furthermore, the sitting time of the drop might influence the result for

adaptive surfaces. Second, the drop could be placed onto the already tilted substrate, inflating it until the gravitational force exceeds the capillary force from the needle and the surface. The drop then detaches from the needle and starts to slide down. Here, adaptive surfaces might even lead to varying drop size as the surface properties change during inflation. Even for non-adaptive cases varying drop size can result at different spots from inhomogeneities on the surface. Therefore the third option is chosen: dropping onto the already inclined surface from a small height. A slow flow of water will form a drop at the tip of the needle, that pinches off when gravitational exceed capillary forces at the needle. That way the drop size should remain constant for one needle and the drop has no sitting time. The drop detaching volume V is proportional to

$$V \sim \frac{\gamma_{LG} R_{Needle}}{g\rho}, \tag{20}$$

with needle radius R_{Needle} [52].
By changing the needle diameter the drop size can be varied. Experiments are conducted with two needle types leading to drop sizes of $(33.5 \pm 0.3)\,\mu$L and $(17.6 \pm 0.3)\,\mu$L. Depending on the falling height h_0 and inclination angle α the drop will already have an initial velocity component parallel to the surface at the time of impact. When neglecting air resistance this initial velocity can be calculated as:

$$v(t = 0) = \sin\alpha \cdot \sqrt{2h_0 g} \tag{21}$$

So even for a small falling height of $h_0 = 3$mm the drop will start to slide with more than 20 cm/s on a 60° tilted plate. The needle is therefore always deposited as low as possible without bringing the drop into contact with the surface before pinch off.
Choi et al. have shown that even for conventional pipetting, the drops can charge electrically due to the interaction with the pipette surface [53]. For that case Equation 20 has to be extended by an electrostatic force, that can change the volume at which the drop detaches. Therefore, the needle in this setup is grounded to remove possible charges that build up in the Teflon tube and to get constant drop sizes.
All of the mechanical parts were ordered at Thorlabs GmbH and Manfrotto GmbH, except for the sample holder plate. The plate was designed for this setup and then given to the mechanical workshop of the institute for production. It is able to hold samples of variable widths, lengths and thicknesses and a hole was inserted so that later an additional camera and light for a top/bottom view of the drop might be added. Also, two recesses were milled about 2 cm before the camera's field of view (FOV), that serve to insert a laser trigger. The trigger is built from a class 1 laser-diode and a photodiode by the electronics workshop. When a drop passes, the laser is blocked and the photodiode detects a change in light intensity. A 5V signal is created and sent to the camera to trigger the video recording. In the recording software a delay time can be used to adjust the recording start depending on the time the drop needs to travel from the laser trigger to the FOV of the camera. An image of the plate, the laser trigger and a mounted glass sample can be seen in Figure 17. The sample is locked in position by a clamp. The plate has various boreholes so that the position of the laser or the clamp can be switched and additional elements, as the reflection blocker in this image, can be attached. Furthermore, the plate is mounted on two rods that come from the rotation mount and serve as rail. By this, the relative position of the sample to the pipette or camera can be changed. An engraved scale on the rods facilitates the exact adjustment and repeatability of the experiments.

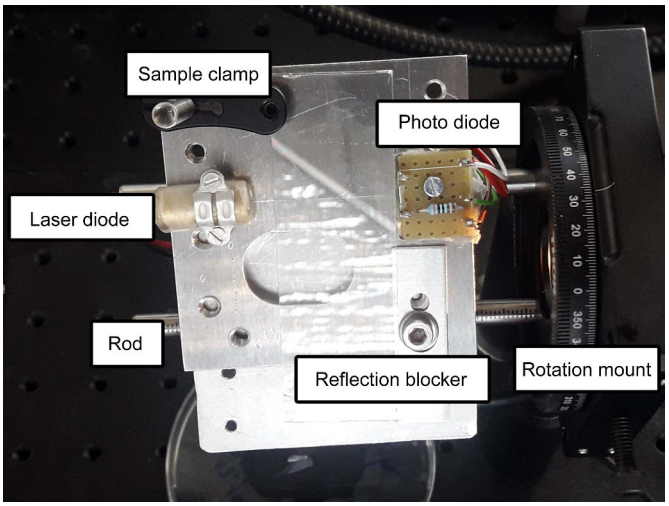

Figure 17: Photo shows the plate with the laser trigger, sample holder clamp and a metal plate to block reflections from glass samples. The plate is mounted on two rods, that are attached to the rotation mount and allow to change sample position relative to pipette and camera.

Table 2: Camera specifications

Producer	Photron
Model	Mini UX100
Maximum resolution	1280 x 1024 pixel
Pixel size	10 μ m
Memory	32GB
Maximum fps	800,000
Resolution at 800,000 fps	640 x 8
Pixel depth	12 bit

3.2 Optical system

The optical system plays a crucial role for the contact angle measurements and determines the accuracy of the complete setup. For recording a *Photron Mini UX100* high-speed camera is used, that can record up to 4,000 fps at full resolution (1,280 x 1,024 pixel) and up to 800,000 fps at reduced resolution (640 x 8 pixel). An overview of the most important specifications of the camera can be found in Table 2. The camera comes with a software to control settings and to record. The videos are recorded onto the fast internal memory of the camera first. When the recording is finished, the data is transferred to the computer via Ethernet cable. Later, the videos are analysed by a contact angle measurement software, explained in Section 3.3.

Different lenses are mounted onto the camera according to the physical quantities of interest. For analysis of the drop motion over the whole sample without contact angle analysis a Computar V2518 25mm objective is used. For contact angle measurements 1x and 2x magnification lenses from *Edmund Optics* are used. The choice of lenses is inherently connected to the maximum velocity of drops that can be recorded and the maximum resolution of contact angles. The higher the magnification, the less light the sensor receives, which in turn limits the maximum frame rate or shutter time of the camera and can lead to blur for fast drops. The 2x magnification allows a high resolution of the whole drop for precise contact angle measurements with a resolution of 5μm/px, while the 1x magnification allows to measure contact angles over a longer distance but with less accuracy. Their specifications are given in table Table 3.

Both lenses for contact angle analysis are bi-telecentric. A telecentric lens is characterised by the fact that the entrance or exit pupil is located at infinity so that the object-sided or image-sided chief

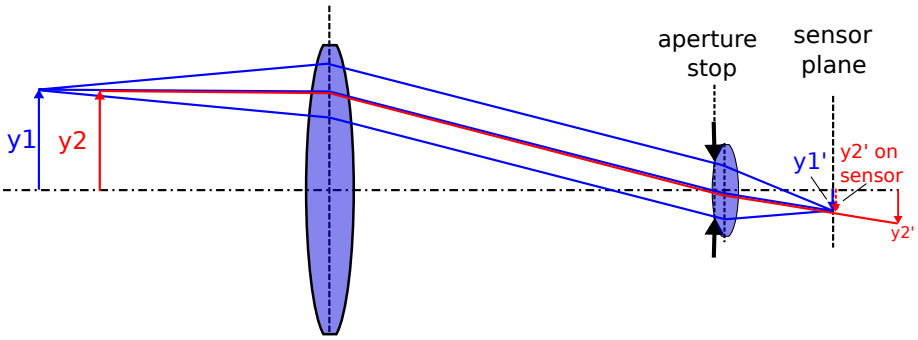

(a)

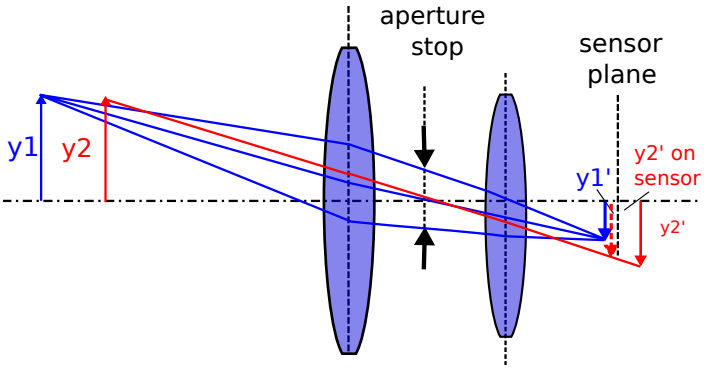

(b)

Figure 18: Illustration of an object-side telecentric lens (a) and a common entocentric lens (b). Based on [54]

Table 3: Specifications of lenses used for contact angle analysis

Producer	Edmund Optics	Edmund Optics
Type	bi-telecentric	bi-telecentric
Magnification	1X	2X
FOV on Photron MiniUx100 sensor	12.8mm	6.4 mm
Pixel resolution on Photron MiniUx100 sensor	10μm/px	5μm/px
Typical distortion at 588nm	< 0.06%	< 0.04%
Typical telecentricity at 588nm	< 0.045°	< 0.075°

rays are parallel to the optical axis. That results in a constant magnification, independent of the object's distance from the sensor plane [55], as can be seen on the schematic view of an object space telecentric lens in Figure 18a compared to a common (entocentric) lens in Figure 18b. A bi-telecentric lens is telecentric in both object and image space, so that the magnification is independent of object and image position. This is achieved by placing the aperture stop at the coinciding focal points of the entrance and exit lens. Apart from the mentioned magnification constancy another benefit of telecentric lenses over conventional lenses is that they have less barrel or pincushion distortion and therefore are also widely used in machine vision. Pincushion and barrel distortion are radial distortions resulting from non-uniform magnification, see Figure 19 for an illustration.

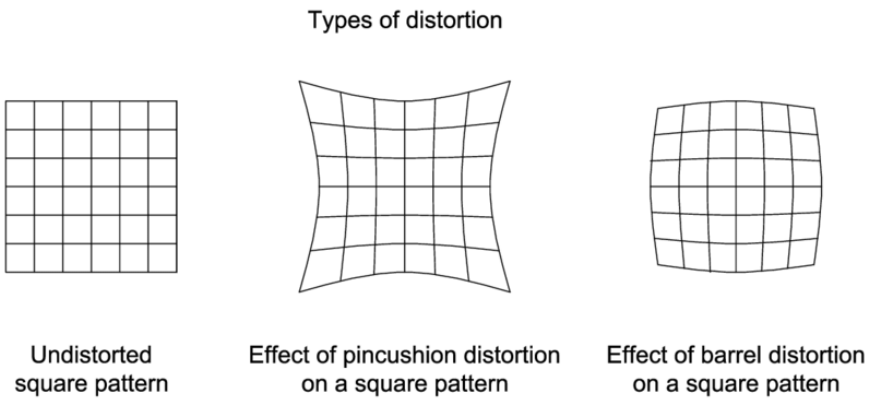

Figure 19: Types of distortion, taken from [56]

For recording droplets at high frame rates a sufficiently powerful light source is needed, because the number of photons reaching the sensor is limited by the short exposure time and the magnifying objective. Therefore, a high intensity LED of *Advanced Illumination* is used. Additionally, telecentric, which means collimated, light is created using the LED in combination with another telecentric objective. Although telecentric illumination and collimated illumination both mean that the light rays are parallel, in practice LEDs sold as "collimated" are sometimes insufficiently collimated, still bearing a beam angle of more than 10° [57]. One reason to use telecentric illumination is the enhanced edge contrast due to the fact that diffuse reflections at the object are reduced. Another advantage is an increase of the light throughput to the sensor when used with a telecentric camera objective, because only a small part of the light is lost. This allows for higher magnifications and higher frame rates and therefore higher drop velocities. In contrast, a diffuse light emits light in many angles and the efficiency of light emitted by the LED towards light received by the camera sensor is much lower. The

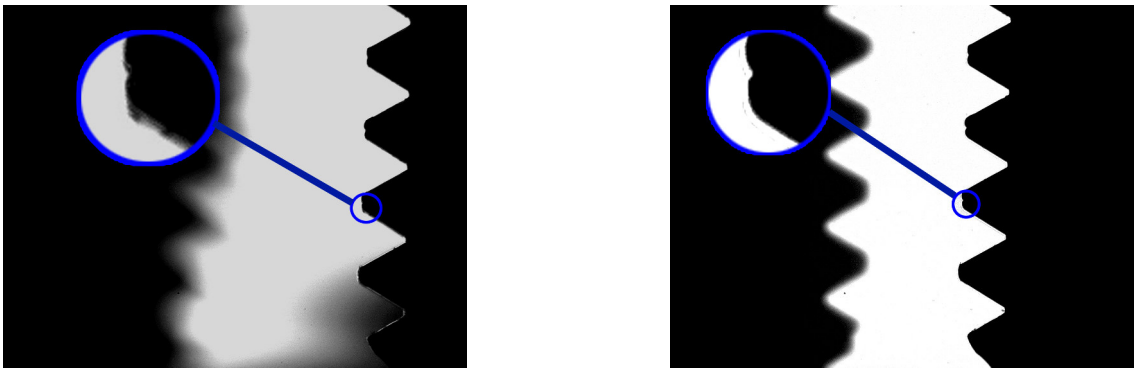

(a) (b)

Figure 20: Two screws at different object distance taken with a telecentric camera objective. In picture (a) diffuse illumination is used and in (b) telecentric illumination

third advantage of telecentric illumination is a reduction of blur of defocused objects when used in combination with a bi-telecentric objective, resulting in a depth of field perceived larger [58]. I tested the improved edge contrast and depth of field of the telecentric illumination with two test objects (Figure 20).

With the purchased light and camera objective combination velocities of $400\,\mu$m/s up to 30 cm/s were successfully tested. That means that according to Figure 12 adaptive wetting processes with time scales from $\tau \sim 0.1\,\mu$s to $\tau \sim 0.1$ ms can be investigated on this setup. Slower processes might also be detectable but rather by changes of velocities and contact angles over drop numbers, not by velocity dependent CAH.

For the drop motion it can be of interest to get a top/bottom view of the drop, in order to detect possible drop deformations. The deformation depends on the capillary number. For increasing capillary numbers the base area of the drop elongates from a circle to an oval shape and the aspect ratio of drop length to drop width increases [59]. When the capillary number is further increased a corner develops at the rear side [60], [59]. This is problematic as contact angle models start to deviate strongly when a corner develops [61]. For even higher capillary numbers the corner becomes a cusp and finally a trail develops that leaves little droplets behind. Therefore it was tested if it is feasible to install a mirror so that both, bottom view (for drop deformations) and side view (for contact angles) can be recorded at the same time using just one camera. The path of the light of the mirror image is longer than for the real drop and therefore the depth of field is the critical factor for this setup. Unfortunately, the depth of field is insufficient to be able to focus on both views at the same time (Figure 21). The depth of field increases with decreasing magnification [62], so this might be an option for future investigations with lower magnification lenses. Here, a set of experiments was run with a changed position of the camera to see whether cornered drop deformation appear. As can be seen in Figure 22, the drop elongates for high capillary numbers but maintains an oval shape. This agrees with the fact that Le Grand et al. found the critical capillary number for corner development to be $Ca_c > 3.5 \cdot 10^{-3}$ and our experiments were conducted for lower Ca. Therefore a side view is sufficient for our needs. In the future, a second camera might be added if higher capillary numbers are of interest.

When glass slides are used as a substrate, reflections can distort the image and make contact angle measurements impossible. Using a metal plate of the same thickness and placing it between light source and glass improves image quality significantly (Figure 23). Adjusting aperture of light and camera objective as well as their geometrical alignment finally leads to a clear image with strong contrast that enables to do automatic processing of the contact angles (Figure 23 (c)).

(a) (b)

Figure 21: Insufficient depth of field for using a mirror to obtain a simultaneous side and bottom view. Picture (a) focussed on the side view, picture (b) focussed on the bottom view. The white line indicates the edge of the mirror

(a) (b)

Figure 22: Two examples of drops from a top view on PDMS brushes. Drop in picture (a) moves with ca. $v = 7\,\mathrm{cm/s}$ or $Ca = 9 \cdot 10^{-4}$. The drop in picture (b) with ca. $v = 20\,\mathrm{cm/s}$ or $Ca = 2.4 \cdot 10^{-3}$. Aspect ratios of the drops are 1 and 1.3 respectively. Contrast is digitally enhanced.

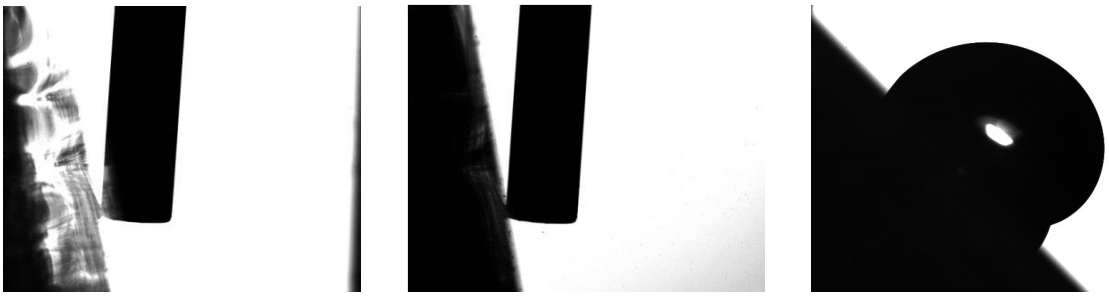

(a) (b) (c)

Figure 23: Reflections for glass substrates: For illustration a needle is placed in contact with a glass slide on picture (a). For picture (b) a metal plate shields the reflections. Picture (c) shows a typical example of a sliding drop on the finalised setup. A strong contrast is accomplished even without digital enhancement.

The video of one experiment usually contains thousands of images that need to be processed. Therefore a software is necessary. For this thesis, a fully automated program was assembled for *MATLAB* that can analyse a whole set of videos at the push of a button. In a first step, a recursive algorithm categorises all the images and detects which sections of the videos show a complete drop and are therefore suitable for contact angle analysis. For the actual contact angle analysis an already existing code developed by Andersen et al. [63] was used and modified according to the needs for this work.

Preprocessing

Usually, contact angle data is averaged over multiple drops and the videos contain a series of drops with some time in between them. Therefore, a large part of the images actually show only the background or parts of the drop. But the code used for contact angle analysis requires images containing the whole drop. Therefore, these sections have to be extracted from the recorded videos at first. The video data can be divided into three categories of sections: The first section before and after a drop has passed, only showing the the background (Figure 24a), the second section showing the drop only partly while entering and leaving the FOV of the camera (Figure 24b) and the third section showing the whole drop (Figure 24c). A recursive algorithm was developed to search for starting and ending points of sections belonging to the different categories.

First, it identifies the sections that belong to category one (only background), and then distinguishes between categories two and three in the remaining parts. As this kind of analysis takes a few seconds per image, a linear image by image comparison of all frames takes too much time and a recursive algorithm was devised to reduce the number of images that need to be analysed. It first moves in large steps through the stack of images only comparing every Δn images, where Δn is the step size. If a change of category is found between two of these large steps, the recursive algorithm starts to search for the exact section ending point in the part between the last two analysed images. This is done by dividing the current part in the middle into a left and a right part and then analysing the image in the middle. According to the result, this process is repeated for the right or the left part. This is done until narrowing down the position of the section ending to one image. After that, the index of this point is saved and the algorithm starts moving with step sizes of Δn again to repeat the same process until all the images have been categorized. This way, the searching process requires only an order of $\mathcal{O}(n \log_2 n)$ instead of $\mathcal{O}(n^2)$ analysing operations for n images. That means, that the time necessary for categorisation of a 100 frame video section can be estimated the be in the order of a few minutes instead of a few hours.

All images of category one (except for one needed as reference later on) can be deleted as they contain no additional information. To detect images from this category, it is required that the first image in the directory belongs to category one, as a reference. The algorithm can then compare other images and by calculating the 2D-correlation coefficient determine whether or not an image belongs to this category. Images of category two, showing parts of the drops, cannot be analysed by the contact angle software, but are still not deleted, as they can be useful for analysis. To identify images showing the whole drop, the background is subtracted from the image to be analysed (Figure 24d) only leaving the drop. Now, the first line of pixels at the sides where the drop enters and leaves the image are analysed. When the drop is already completely in the image, these pixels should all be white. A threshold for the sum of these pixel values is used to decide whether the images can be classified as category two or three. The positions of the starting and ending points of sections belonging to category three are saved in a file, for the contact angle analysis.

Contact angle analysis

In order to extract the contact angles from the videos, I use and adapt the openly available script collection *Drop shape analysis* for *MATLAB* (*DSAfM*). It was originally developed by Andersen et

Figure 24: Before contact angle analysis an algorithm divides the video into three categories: Category one only containing the background (a), category two win which the drop is partly visible (b) and category three in which the drop visible completely (c). For distinguishing categories two and three a difference of the image and the background is used (d).

al. [63]. I chose this software because of three main advantages over other common contact angle measurement software. First, the openly available code enables the user to add, change and adapt the functions of the software according to his needs. This is often not the case for commercially available software and is necessary to improve the results for baseline finding, edge detection and automation of the video analysis. Secondly, the software offers to analyse non-axisymmetric drops, unlike the common axisymmetric drop shape analysis used for sessile drops. That makes it a perfect tool for the measurements of CAH of a moving drop, where for example the *LB-ADSA* plugin for *ImageJ* fails. Third, a well functioning automatism for analysing images without manual input is already implemented. There is no need for setting a baseline or indicating the drop shape as for example with *DropSnake*, another popular contact angle measurement tool for *ImageJ*. This is the only way to analyse the thousands of images captured by the high-speed camera in an efficient way. The possibility to change the code allows to enhance the automation functionality. For example, automatic analysis of the tilt angle and a rotation of the images by this angle was added and requires no manual input, unlike the original version. This was necessary as the original version fails to analyse images of more than 45° inclination. In the following, a description of the final modified version of the (*DSAfM*) will be given, clearly indicating additions done for this work. First, the analysis of a single image is explained.

The outline of the *DSAfM* for a single frame is illustrated in Figure 25. A typical example of an image that is to be analysed can be seen in Figure 25a. For the analysis by this script, a slightly angular view is required so that the beginning of the drop's reflection can be seen. Before starting to analyse the drop, two additional steps were implemented for the modified version. The first step is to carry out a pre-analysis of the tilting angle. As the camera is adjusted horizontally, the inclination in the video is equal to the inclination of the sample in reality. The pre-analysis estimates the tilting angle from the background image and rotates the drop images before analysis. This was required as the *DSAfM* cannot analyse images with too much inclination. Furthermore, I subtract an image containing only the background from the drop image (as in Figure 24d). This is done because it removes possible reflections and prevents errors in drop contour detection caused by the edge of the underlying sample. After that, the drop analysis can start.

The *subpixelEdges* script uses edge detection algorithms already included in *MATLAB* to find possible edge positions with sub-pixel precision. Figure 25b shows the image after these first steps. Next, *findlongestedge* connects the detected edge points to edge lines, filtering for the longest edge to exclude for example reflections or dirt. After that, the edge is divided into left and right part of the drop by *leftrightedges*, so that a different angle can be fitted on both sides.

One of the more tricky operations is the consequent *findreflection*, that tries to identify the baseline of the drop by searching for the point where the drop outline ends and the reflection starts. This way also the baseline is found. The result can be seen in Figure 25c. The *findreflection* script is prone to errors but one of the most important steps for correct contact angle analysis. One problem can

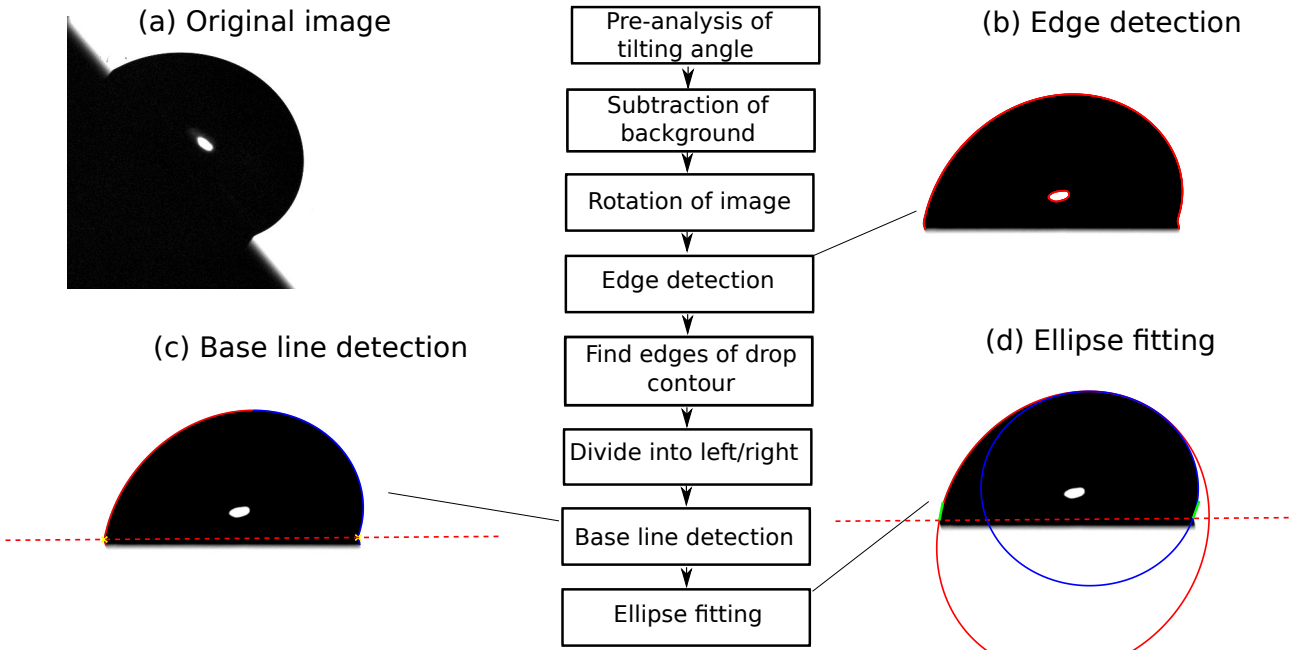

Figure 25: Outline of the adapted *Drop shape analysis* for one image. Original image of side view of the drop sliding down the incline (a), after subtracting the background and edge detection (b), after detecting the longest edge, split into left and right part with detected baseline (c), after ellipse fitting with contact angles illustrated by a tangent in green (d)

occur when the contact angle is of over 90°, and the algorithm can detect wrongly the point of largest radius of the drop to be the point of reflection (right side of the drop in Figure 26a). To solve this problem the original version of the software already includes a kind of cut off parameter to filter out the edge data above a certain y-value. A similarly incorrect detection can happen below the actual reflection (Figure 26b). To avoid the necessity of manually setting these cutoff parameters, they are approximated from the already analysed drop contour. The total height of this contour is used as indication for that. As long as the ratio of reflection height and drop height (depending on illumination and view angle) maintains in a similar range, this works quite well. Another change was done in the algorithm of the *findreflection* script. For each point on the detected edge, the script calculates two linear fits through neighbouring points, left and right of the edge point. Originally, the reflection point is found by searching for a point where the slopes of adjacent points are of similar magnitude but the opposite sign. The slopes are then added up, resulting in a value close to zero for similar magnitude but opposite sign of slope. This is done for all points on the edge, and the reflection point is chosen as the point having the lowest sum, i.e. the lowest difference in magnitude. To increase robustness in the modified version, the two slopes are subtracted instead of added. By that, it can be searched for the highest magnitude, not the lowest. The advantage is that an additional weighting according to the actual magnitude is inherently included. That way "sharper" angles are favoured and errors as in Figure 26a (right drop side) can be diminished. Still, there is certainly more space for improvement in this part of the program in the future.
Finally, the extracted drop shapes for the left and right side can be fitted by ellipses or polynomial functions and the tangent at the intersection with the baseline can be determined. To find the contact angles, the angle between the tangent and the baseline is calculated for the left and right side of the drop (Figure 25d). In the paper published about this software, Andersen et al. analysed the two different fitting methods and found the elliptical fit to be less sensitive to optical distortions and noise than the polynomial one.

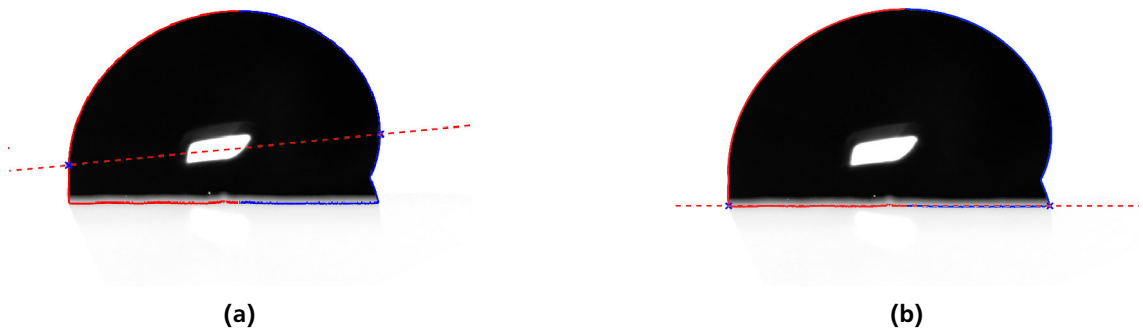

Figure 26: Possible errors in the step identifying the edge between real drop and reflection. In picture (a) on the right side of the drop the algorithm detects the reflection point at the widest part of the drop. This would only be correct in the case of contact angles close to 90°. In picture (b) the reflection point is detected too low.

Table 4: Comparison of measured contact angles by different image analysis methods: manual tangent fitting, the *DropSnake* plugin and the *DSAfM* used throughout this work. For the manual tangent method and *DropSnake*, the measurement was repeated three times and the average value ± standard deviation is given. The *DSAfM* was averaged over three measurements applying a Gaussian blur with a standard deviation of 0,2 and 4.

Method	θ_A*(°)	θ_R*(°)
manual tangent	115.4 ± 1.1	88.1 ± 1.6
DropSnake	118.5 ± 1.1	89.6 ± 1.6
DSAfM	116.6 ± 0.2	88.0 ± 0.4

For the analysis of a complete video instead of a single image the process is very similar. The only difference is that the baseline and the drop's inclination are analysed for all frames before any ellipse fitting. The base line is then averaged to increase accuracy. This is especially necessary due to the sensibility of the *findreflection* script. Especially for contact angles close to 90° the uncertainty is of a few pixels and can lead to significant noise. Therefore, all images should be analysed with the identical, averaged baseline.

Apart from changes to the actual video analysis, I enhanced the automation of the script, so that a stack of videos can be processed by executing the script just once, and I implemented the creation of log files and saving of the output data for improvement of the working process.

I compared the results of the contact angle measurement for one drop image to manual analysis by tangent in *ImageJ* and to the result using the *DropSnake* plugin for *ImageJ*. For the two latter methods the measurement was repeated three times on the same image and the average value and standard deviation were calculated. For the *DSAfM* no manual input is required and therefore, results would only vary within numerical accuracy. To gain an idea of the influence of blur, the analysis was repeated on three versions of the image to which a different amount of Gaussian blur was applied. The standard deviation of the Gaussian blur for the three images was chosen as $\sigma = \{0, 2, 4\}$. The results of the average contact angles and the their standard deviations can be found in Table 4. The average values for the advancing contact angle varies within 3.1° and for the receding within 1.6°. The deviation between measurements is much higher for the two methods in *ImageJ* as they require manual input. Additionally, due to the manual input the measurements took various minutes, while the *DSAfM* only needs a few seconds. Also, setting the base line for the manual methods is very hard, because the reflection point cannot be seen clearly at the rear as $\theta_R \approx 90°$. In contrast, the *DSAfM* can increase accuracy by using the average baseline from the whole video.

Andersen et al. tested the accuracy of the software with generated drop images of defined contact angles. For noiseless and sharp images the maximum absolute error is of ca. 0.8° and occurs at contact angles close to 180°. Between 60° and 110° error is of less than 0.1°. Furthermore, the influence of blurred edges and noise in the image was tested for a drop of 140°. In the unblurred case the absolute error is of 0.2°. Blurring the edge by 0.5 pixels increases accuracy to less than 0.02° because the edge detection algorithm can use the grey-scale information to calculate edges with sub-pixel accuracy, while the sharp image only contains black and white pixels. Increasing the blur further decreases the accuracy and leads to measurement errors of up to 2° for the tested 3 pixel blur at a contact angle of 140°. This corresponds to a relative error of 1.4%. All these tests were done with a rather low-resolution image of 512 x 337 pixels, while the high-speed camera on my setup is used at 1280 x 1024 pixels. In consequence, the contour of the drop and the angle at the contact line can be identified even more accurate and this should increase the accuracy of the contact angle measurement.

Before each experiment the syringe, tube and needle are rinsed with fresh DI water. Samples are cleaned from dust by blowing NO_2 and discharged by using an ionising air blower (IAB) for at least 5 minutes unless stated otherwise. When the sample is fixed, it is rotated to the desired inclination angle and the distance between pipette and camera is set. The pipette is aligned vertically and a few mm above the substrate, so that the drop detaches before touching the substrate, but has a small falling distance.

Before placing the drop, the camera settings have to be configured. The frame rate was chosen according to drop velocity and varied between 50 fps to 4,000 fps. The shutter time was usually chosen to be 1/12,500 s. This keeps the motion blur low, while still guaranteeing a large quantity of light per image. For velocities of more than 0.5 m/s synchronised strobe light is recommended to increase the intensity, but this was not necessary for the conducted measurements.

The videos are recorded onto the fast internal memory of the camera first. When the recording is finished, the data is transferred to the computer via Ethernet cable. Before dropping the first drop of water, the camera is set in endless record mode. That means that it records to the internal memory, and when the memory is full overwrites the oldest images. For example, for a maximum memory capacity of 2 minutes of video, it means that always the last two minutes are stored. A trigger input defines the start or end of the actual video to be saved to the computer later. When a start-trigger is set, the camera resumes recording until either the memory is filled once, an end-trigger is given or a specified frame number is recorded. Transfer to the computer takes about 10 minutes for the maximum video length. The triggers can either be set manually in the software or externally. As mentioned a laser trigger was built, that was used as an external trigger.

Table 5: The different materials tested. Quasi-static advancing and receding contact angles are measured by inflating drop method inflating from 10 to $25\,\mu$L and back at a rate of $1\,\mu$L/s. Heterogeneity is given by maximum difference found in CAH at different spots on the sample. Measurements were repeated at least on three different spots on the sampled and averaged.

Material	Substrate	θ_A*(°)	θ_R*(°)	CAH*(°)	Heterogeneity(°)	Sliding
PHEMA brushes	SI wafer	70 ± 1	26 ± 3	44 ± 2	8	no
PDMS brushes, batch 1	glass	106 ± 1	97 ± 2	9 ± 2	4	yes
PDMS brushes, batch 2	glass	109 ± 1	97 ± 1	13 ± 1	5	yes
PFOTS	SI wafer	115 ± 1	96 ± 1	19 ± 1	1.3	yes

3.5 Testing surfaces

In order to test the functionality of the setup, a first set of experiments is conducted on a possibly adaptive surface in comparison to a presumably non-adaptive surface. Velocities of ca. 0.5 mm/s to more than 20 cm/s can be tested on the setup. According to the adaptive wetting theory, adaptation time scales of ca. 0.1-10 μs are required to observe adaptive contact angle hysteresis for these velocities (Figure 12). No suitable material was found in literature with a confirmed adaptation in that time scale. Often, time resolutionrestricts investigation to slower adaptations. Thin films of polymers are promsing candidates for surface adaptations [50] and therefore polymer brushes were considered as first testing materials for possibly adaptive surfaces. As presumably non-adaptive reference samples fluorosilane coated silicon wafers were used. The institute plans to measure adaptation time scales in the future by surface plasmon resonance (SPR) and x-ray reflectometry (XPR), but currently we have no information about the adaptation or its time scale for the used surfaces. Both surfaces have the advantage of being easy to prepare. For future projects the plan is to also test mixed polymer brushes and random copolymers of hydrophilic and hydrophobic components that promise strong adaptations by selective swelling or molecular reorganisation [9], [43].
In the following, first the general concept of polymer brushes and their role in surface adaptation will be discussed. Then the choice and synthesis of the brushes and the non-adaptive reference material will be explained.

3.5.1 Polymer brushes in general

Polymer brushes are defined as films of polymer chains that are covalently tethered to a surface by one end [64]. Chen et al. published an extensive review of polymer brushes upon which the following section is based [64]. To synthesise polymer brushes "grafting from" or "grafting to" methods can be used. "Grafting from" methods anchor the initiators to the surface first and grow the brushes from there. By this technique one is able to control the properties, as for example grafting density (number of tethered chains per area) or film thickness well. One example of these methods is the atom transfer radical polymerisation (ATRP). The "grafting to" methods graft end-functionalised polymer chains onto the substrate, for example by a thermal process, but are limited in grafting density and film thickness.
By changing grafting density, molecular weight, thickness and chemical composition of the brushes, they can be used to tune surface properties like wettability, lubrication, self-cleaning and adhesion. Because only one end of the chain is anchored to the surface, the brushes show high mobility. They can show very low adhesion and CAH of less than 5°. Additionally, the polymer brush films are very thin and can be used to functionalise surfaces. All of this makes them very interesting for research and application. One example is the use in medical technology where polymer brushes are used as stimuli-responsive surfaces for drug delivery.
Polymer brushes can take on different chain conformations according to grafting density, solvent quality, and the substrate-chain interactions. The conformations are commonly classified into a pancake,

mushroom, and brush regime as illustrated in Figure 27. For low grafting densities the conformation is governed by the strength of interaction with the substrate. When the interaction with the substrate is low, as in a good solvent, the chains stretch away from the surface and the chains take on the mushroom state [65]. For strong interaction with the substrate in a poor solvent, the chains collapse and create the pancake conformation. For high grafting density, the repulsive interaction between brushes creates the brush conformation, in which the chains become stretched and less mobile [65] . The thickness of a polymer brush layer depends on the equilibrium of osmotic pressure and elastic forces from chain stretching [66]. The solvent quality determines the osmotic pressure and in contrast to bulk polymers, polymer brushes collapse gradually with decreasing solvent quality [66].
The dynamics of the swelling has been investigated by Biesalski et al. for the case of polyelectrolyte brushes in water [67]. He observed an initial increase of film thickness apparently governed by diffusion. Interestingly, the water diffused faster than would be expected in the case of Fickian diffusion. Naini et al. showed that switching kinetics of thermoresponsive poly(N-isopropylacrylamide) (PNiPAAm) brushes in water follows first-order kinetics and has a response time in the order of microseconds to milliseconds for 65nm thick films [68].

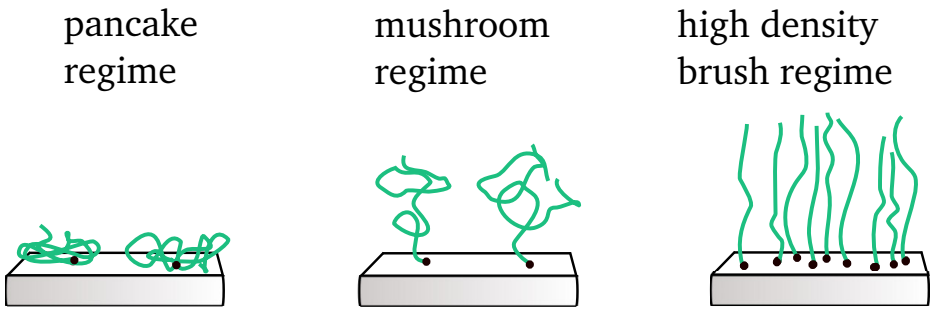

Figure 27: Schematic illustration of the different conformations of polymer brushes

3.5.2 Polymer brushes used for this work

Polymer brushes have already been used to create adaptive surfaces. The selective swelling of polymer brushes can be used to switch surface properties when different kinds of polymer chains are grafted on the same surface. These so-called mixed brushes can be used to change the properties of the surface by using selective solvents that swell one of the brush types while the other one remains collapsed. That way the upper layer exhibits properties of the swelled polymer brushes according to the solvent used. By this manner, Minko et al. produced a surface that can be switched from hydrophilic to hydrophobic and vice versa by exposure to different solvents [9]. But the synthesis of mixed polymer brushes is not trivial and was therefore not suitable as initial testing surface. Still, due to the fact that polymer brushes are very responsive to their surrounding they make interesting candidates for surface adaptation. For this work two different types of possibly adaptive surfaces are considered: PHEMA and PDMS brushes.

PHEMA brushes

PHEMA brushes can be produced in-house by "grafting from" technique ATRP and promise therefore well controllable brush layers. Furthermore, PHEMA takes up water [69] and contact with water can thus be expected to increase hydrophilicity. PHEMA brushes were synthesised on a silicon wafer by Gunnar Kirchner (Max Planck Institute for Polymer Reseach, Mainz) and quasi-static CAH was measured by the inflating drop method for characterisation. A 10 μL drop was inflated to 25 μL, and subsequently deflated with a volume flow of 1 μL/s. The results are reported in Table 5. Additionally, the surface was tested on the setup. Unfortunately, the hydrophilicity and CAH were found to be too high for the tilted plate setup. At the rear contact angles of close to zero were observed. Drops stick

to the surface up to 90° inclination. A rough estimate for a 20μL with $\theta_{min} = 0°$ and $\theta_{max} = 70°$ using Equation 5 gives an adhesion force of 250μN but a gravity of 200μN. The adhesion force is higher than gravity and the drops does not move. When the water is dropped from a few centimetres height, the drop elongates extremely, leaving a trail behind before stopping. Figure 28 shows a set of still frames from a video. At the rear, film instability sometimes breaks the trail and various small droplets are left behind. While it might be possible to gain interesting insight from studying this behaviour, it is not the objective here. The elongated drops cannot be analysed by the video analysis software as they do not maintain an approximately round shape and advancing and receding side are too far apart as to fit onto the FOV of the camera. For that reason, PHEMA brushes were not studied further.

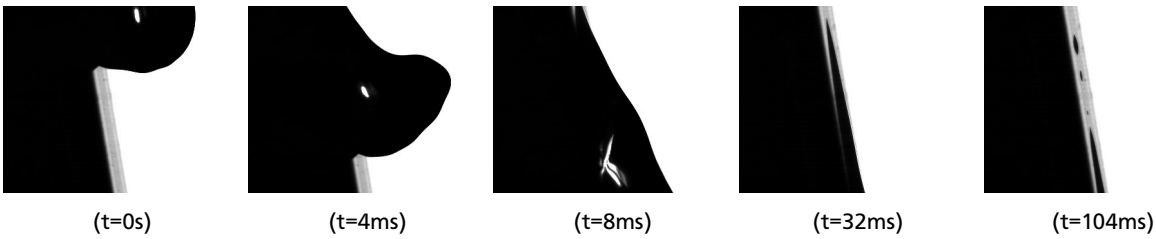

Figure 28: Drop of water impacting on a inclined PHEMA surface (α =80°). The drop elongates and sticks to the surface. Film instability breaks up the trail and leaves small droplets. Therefore the more hydrophobic polymer surfaces were used for the following experiments.

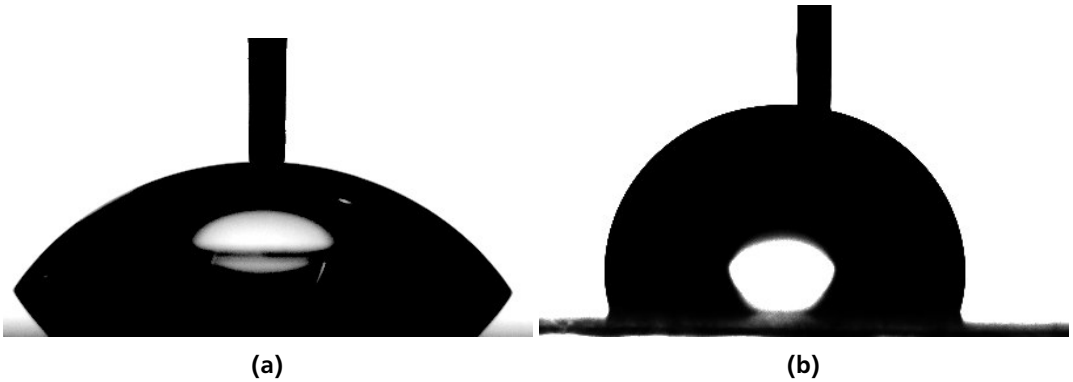

Figure 29: Still frames from quasi-static CAH measurements with water by inflating drop method. Picture (a) shows PHEMA brushes on a silicon wafer with $\theta = 55°$. Picture (b) shows PDMS brushes on glass with $\theta = 105°$. Contrast is enhanced digitally

PDMS brushes

As an alternative, I prepared PDMS brushes on glass. These surfaces show a low hysteresis and good self-cleaning properties and are therefore interesting for application in many fields, as e.g. medical technology. The low hysteresis is attributed to the high mobility of the brushes and these surfaces are therfore somtimes referred to as 'liquid-like' [70]. Although PDMS is hydrophobic, small amounts of water have been shown to diffuse into it, for crosslinked PDMS up to 40 mol/m^3 [71]. Furthermore, the preparation of these kinds of surfaces is very simple and can be done even by persons, who are not experienced in chemical synthesis.

The PDMS brushes are prepared following the steps as provided by Teisala et. al [72]. They recently found that PDMS binds even at room temperature and without additional UV radiation or heat supply. The grafting reaction is thought to be initiated by hydrolysis of the PDMS by water that is surface-bound to the substrate. The PDMS chains become Si-OH terminated in this process and can then bind to the silanol groups of the surface via condensation or other hydrolysed PDMS chains. The authors also conducted X-ray photoelectron spectroscopy measurements to study the amount of bound PDMS.

The results indicate that for increasing grafting time (exposure time) the bound chains grow in length, while the grafting density remains constant, creating covalently bound polymer surfaces.
For preparing these surfaces, glass slides are first ultrasonicated in toluene, ethanol and deionised (DI) water for 5 minutes each and then dried by nitrogen before cleaning them with an oxygen plasma for 10 minutes. After that, ca. 30 mg of liquid PDMS oil is drop-casted onto the strongly hydrophilic glass. The liquid spreads fast and leaves a thin film. After a certain grafting time the sample is ultrasonicated in toluene, ethanol and DI water consequently for 10 minutes each to remove the unbound PDMS. A thin film of less than 10 nm is left on the glass slide. Teisala et al. measured film thickness by atomic force microscopy (AFM) and found it to increase with grafting time from 2.8±1.1 nm for 1 day, 4.3±0.7 nm for 5 days and 5.1±0.7 nm for 10 days. They also measured quasi-static CAH with the inflating drop method for different grafting times and molecular weights of the PDMS oil used. The advancing contact angles increase with grafting time from $60 \pm 5°$ for 1 minute to $106 \pm 1°$ for 2 hours, up to $109 \pm 1°$ for 2 to 10 days. Increasing the grafting time first decreases CAH until a grafting time of 1 day. Then the CAH increases (due to a decrease in the receding angle) and more stick-slip was observed. The results for the CAH can be seen in Figure 30a. For molecular weight of more than 7000 g/mol entanglement is expected for PDMS and indeed CAH increases for high molecular weights (Figure 30b). That was explained by Teisala et al. by decreased mobility of the PDMS, bringing its properties closer to cross-linked PDMS that shows a CAH of about 30°. Similarly, for very low molecular weights also higher CAH was observed. The hypothesis of Teisala et al. is that the PDMS chains are too short and therefore inflexible.

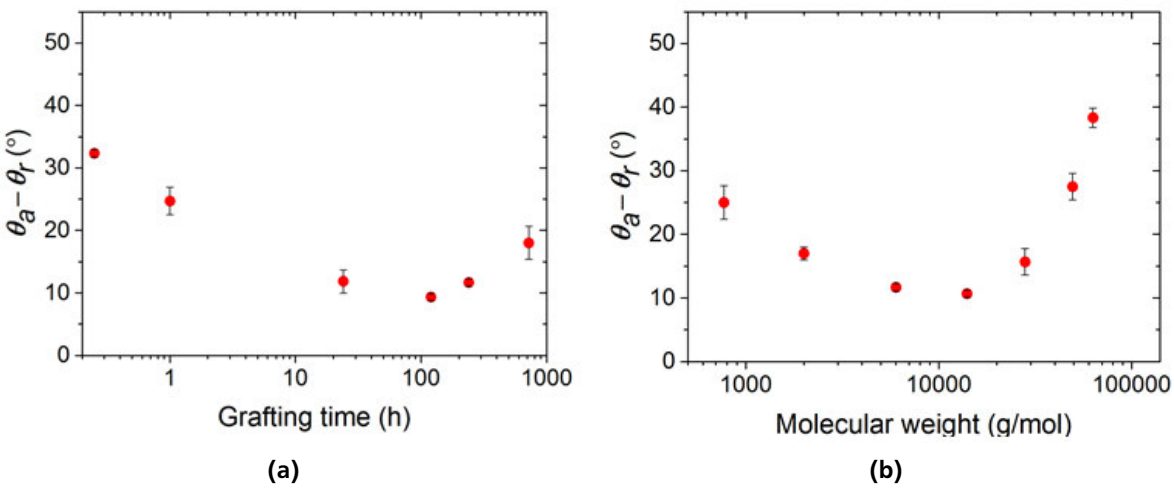

Figure 30: Contact angle hysteresis (CAH) on liquid-like PDMS, reprinted with permission from [72]. Measured by inflating/deflating the drop from 10 to 25μL and back at a rate of 1 μL/s. Picture (a) shows the CAH for different grafting times and a molecular weight of 6000g/mol. Picture (b) shows CAH for different molecular weights and 24h grafting time.

For this thesis, grafting times of 24 hours have been used and PDMS of a molecular weight of 6000g/mol. The surfaces thus should show film thicknesses of 3 to 4 nm. Indeed, they were found to be too small for identifying them by profilometer. As substrate microscope glass slides were used as they are reported to be almost atomically flat [73], easy to use and of low cost. Two batches were prepared by the same procedure, but using different oxygen plasma cleaners as the first one was out of order for the second batch.
To characterise the samples, the inflating drop method is used with the same parameters as by Teisala et al., for reasons of comparability. The results can be found in Table 5 for both PDMS samples. The receding angles agree with the results of Hannu et al. showing $\theta_R^* = 97°$, but the advancing angle of batch 1 is 3° lower. Hannu et al. reported $\theta_A^* = (109 \pm 1)°$, as on batch 2. For batch 1 $\theta_A^* = 106°$. The

CAH on batch 1 is therefore of ca. 9° and smaller than the 12° from the reference. With measuring accuracies of ±1° to 2° for these measurements the deviation is still acceptable. For one sample of batch 1 furthermore the surface roughness was measured by AFM and found to be 0.6 nm

3.5.3 Fluorosilane surfaces as reference

Fluorosilane is used as reference system as it exhibits contact angles and hysteresis in a similar range as PDMS brushes. I prepared the surfaces with the help of Alexander Saal and Amy Stetten (both Max Planck Institute for Polymer Research, Mainz) by chemical vapor deposition on silicon wafers using trichloro(1H,1H,2H,2H-perfluorooctyl)silane. The wafers are cleaned in an oxygen plasma before and CVD is carried out under vacuum. P-doped (P++/Boron) silicon wafers supplied by Si-Mat are used with a thickness of 525 μm and resistivity of less then 0.005 Ω cm. Drops passing over a surface can lead to charge separation leaving a charged surface and drop and creating a Coloumb force [74]. This might also be considered as an adaptive process[8]. Although it is not clear yet, whether the charging effect is strong enough to influence the contact angle, I attempt to minimise this charging for the reference material. Experiments within our group have shown mostly positive charge of drops, in agreement with Yatsuzuka et al.[74], so that the surface should be left with a negative net charge. Therefore a p-doped silicon wafer can help to neutralise the surface charge by mirroring it. Furthermore, the wafer is deposited onto an aluminium plate for the experiments.
Again, quasi-static CAH is measured by inflating drop method (Table 5). The receding angle of ca. 95° is similar to the PDMS surfaces, but the advancing angle is higher with 115°, leading to a higher hysteresis. For comparison of dynamic CAH it would be ideal to have the same CAH and contact angles. By tuning the process parameters of the PDMS grafting and fluorosilane coating this is probably doable, but was not possible within the time range of this thesis.

4 Experimental results

Three different kinds of experiments were conducted. In Section 4.1 the dynamics of a single drop on an incline are studied and compared to experiment, for the reference case and for the PDMS brushes. The functionality of the goniometer was tested by measuring the dynamic CAH of both surfaces for different contact line velocities by changing the inclination angle. This is discussed in Section 4.2. Furthermore, I investigated whether the number of drops that rolled or slid down the PDMS-brush surface has an effect on the velocity or contact angle. These experiments are presented in Section 4.3.

4.1 Dynamics of a drop on an incline

At first, the dynamics of a single drop moving down a non-adaptive surface will be discussed. This is of interest for understanding the influence of parameters like pipette height, inclination angle and rolling distance on the drop velocity. Furthermore, the contact angle measurements should be conducted at a distance, where initial drop oscillations resulting from the impact have already decayed.
As explained in Section 2.3, a drop on a surface that is inclined gradually will start to move when the inclination angle α is higher than a critical sliding angle α_c. Gravity G and contact line pinning force or adhesion force F_{Adh} are in balance at the critical angle [61]. For $\alpha > \alpha_c$ the drop slides or rolls down the surface and additional forces will act [75]. On an ideally flat, homogeneous and rigid surface the drop will accelerate until a balance of forces is reestablished and then continue with a constant velocity. Various studies have been published studying this terminal steady-state velocity [76, 77, 61, 78, 75]. Commonly the aerodynamic drag is considered negligible and steady-state velocity is deduced from a balance of gravity

$$G = m \cdot g \cdot \sin\alpha, \tag{22}$$

a force of viscous dissipation in the drop

$$F_{Vis} \sim v \cdot \eta \tag{23}$$

and a contact line pinning force or adhesion force as defined previously by Equation. (5). The steady-state velocity is defined by the balance [61]:

$$m\,g\,\sin\alpha = F_{Adh} + F_{Vis} \tag{24}$$

To be precise F_{Adh} as defined by Equation (5) is just the static adhesion force that needs to be overcome to move the drop. The equation was originally derived for a static drop at the verge of sliding and the contact angles entered into the equation are static angles [28]. For finding the steady-state velocity this force is commonly assumed to be constant even for the dynamic regime [77, 75, 61] and velocity dependent forces are modelled by the viscous term. It was shown by Pilat and Gao et al. experimentally that Equation (5) even holds for the dynamic regime, giving the complete force necessary to move the drop, by inserting the dynamic contact angles instead of static ones [79, 80]. This can be interpreted as the kinetic lateral adhesion force:

$$F_{LA}(v) = \frac{24}{\pi^3}\gamma_{LG}D(\cos\theta_R(v) - \cos\theta_A(v)) \tag{25}$$

Therefore the sum of the retarding forces in Equation (24) can be interpreted as a kinetic adhesion force. It can be reasoned that the equation even holds for the kinetic case because the dynamic

contact angles already incorporate the effect of viscous dissipation. Using Equation(25) to represent the retarding forces in Equation(24) yields:

$$m\,g\,\sin\alpha = F_{LA}(v) \tag{26}$$

This equation describes the steady-state. To gain an idea of the transient dynamics before reaching the steady-state a simple approach is to model the motion of a drop by Newton's second law [78, 81, 82, 83]. Ahmed et al. compared this analytical approach to a more detailed numerical simulation and found good agreement when drop deformation was not too strong [82]. According to Newton's law the acceleration is proportional to the net force:

$$\frac{dv}{dt}\cdot m = m\,g\,\sin\alpha - F_{LA}(v) \tag{27}$$

For the steady-state $dv/dt = 0$ and Equation(27) consistently becomes Equation (26). To calculate the dynamic lateral adhesion force a contact angle model is necessary. In a first step, following Pilat et al. a linear model of the MKT is used, that allows solving Equation (27) analytically by a simple exponential Ansatz. For the case of small arguments of the sinh in the MKT equation it can be written:

$$v = \frac{\gamma_{LG}}{\zeta}(\cos\theta^{\infty} - \cos\theta_d(v)), \tag{28}$$

where the MKT parameters have been combined in a contact friction coefficient [1]

$$\zeta = \frac{k_B T}{\kappa_0 \lambda^3} \tag{29}$$

It has been shown that ζ can also be expressed in terms of viscosity:

$$\zeta = \frac{\eta\,\nu_L}{\lambda^3}\exp\frac{\gamma_{LG}(\lambda^2\cos\theta^{\infty}+1)}{k_B T}) \tag{30}$$

in which θ^{∞} is the Young's static contact angle and ν_L corresponds to the volume of liquid displaced, and can be approximated by the molecular volume of the liquid [84]. The friction coefficient thus incorporates effects of bulk viscosity [35]. Equation (28) can be used to calculate the dynamic advancing and receding angle by changing the sign of velocity. As common surfaces show hysteresis even for v =0 m/s different θ^{∞} have to be chosen for advancing and receding angles [35], here denoted by θ_A^{∞} and θ_R^{∞} respectively. This can be inserted into Equation (25) as proposed by Pilat et al.:

$$F_{LA}(v) = \frac{48D\zeta}{\pi^3}v + \frac{24}{\pi^3}\gamma_{LG}D(\cos\theta_R^{\infty} - \cos\theta_A^{\infty}) \tag{31}$$

Inserting Equation (31) into Equation(27) one obtains:

$$\frac{dv}{dt}m = m\,g\,\sin\alpha - \frac{48D\zeta}{\pi^3}v - \frac{24}{\pi^3}\gamma_{LG}D(\cos\theta_R^{\infty} - \cos\theta_A^{\infty}) \tag{32}$$

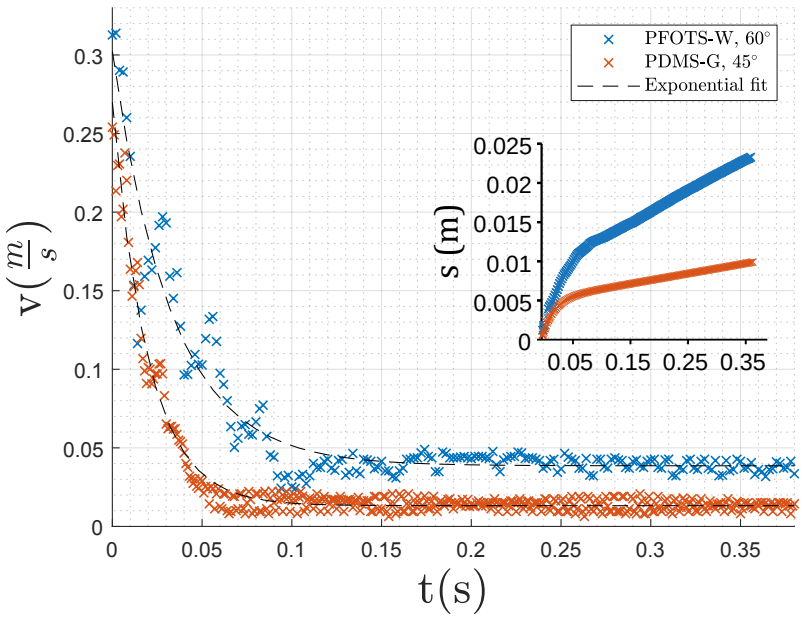

Figure 31: Examples of the initial dynamics of a $(17.6 \pm 0.3)\,\mu$L drop of water on PFTOS on silicon wafer and PDMS brushes on glass (sample 1). The inclination angles were 60° and 45° respectively. The insert shows the travelled distance over time for both drops.

Solving the differential equation (32) by an exponential Ansatz yields the solution

$$v(t) = \frac{\Pi_1}{\Pi_2} + (v_0 - \frac{\Pi_1}{\Pi_2}) \exp(-\Pi_2 \cdot t), \tag{33}$$

$$\Pi_1 = g \sin\alpha - \frac{24}{m\pi^3} \gamma_{LG} D (\cos\theta_R^\infty - \cos\theta_A^\infty), \tag{34}$$

$$\Pi_2 = \frac{48 D \zeta}{m\pi^3} \tag{35}$$

with initial velocity v_0. Keeping in mind the simplifications of this model, especially the linear MKT, it should be used mainly for qualitative analysis. According to Equation (35), the movement can be described by an exponential function. The drop will accelerate or decelerate depending on v_0 and converge towards a constant steady-state velocity v^∞. The steady-state velocity depends on the balance of gravity and the kinetic adhesion force. The relaxation time of the exponential function scales $\tau \sim m/\zeta$, and therefore higher friction coefficients and lower drop mass should reduce the time to reach steady state.

To see if drops do indeed follow an exponential behaviour, the initial dynamics of drops on both samples were measured. At first the pipette was adjusted in a way that the impact of the drop can be seen on the video. The low magnification 25 mm objective was used to cover large distances. The contact angle software cannot be used here, due to the low magnification and the poorly resolved drop. Therefore the drop velocity was extracted by tracking the whole drop with *Photron FASTCAM Analysis*. For the PFOTS surfaces the quasi-static hysteresis is larger and a higher inclination is necessary to overcome the static adhesion force. Two exemplary results can be seen in Figure 31. It shows the first 370 ms after the drop impacts and wets the surface. The blue curve shows the fluorosilane (PFOTS) on a wafer, the red one PDMS brushes on glass. To verify Equation (35) exactly, contact angle measurements are necessary. For this reason, at the moment an exponential fit is used. It can be seen that the velocity indeed follows an exponential decay, also on the PDMS brushes. The dropping

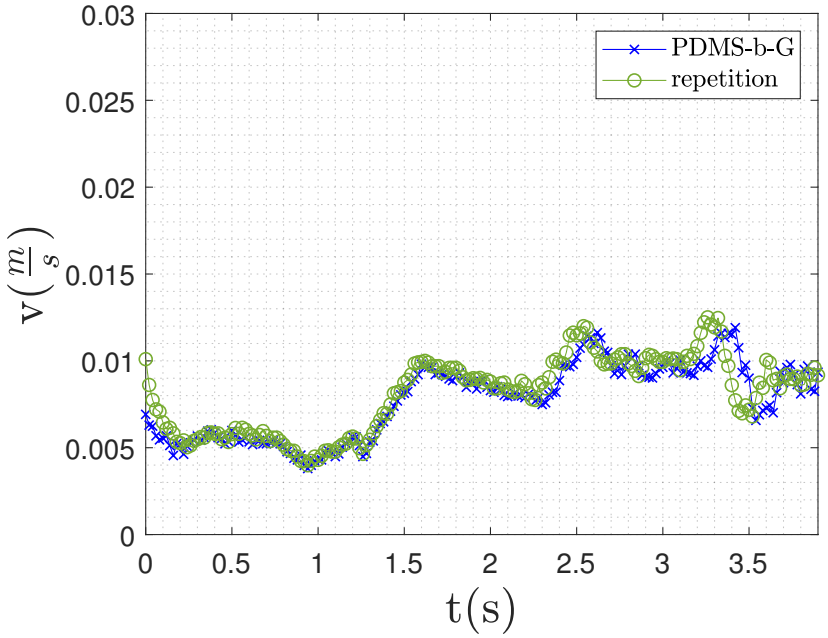

Figure 32: Examples of velocity fluctuation on PDMS brushes on glass (sample 1). The first drop and a subsequent drop show the same behaviour

height was ca. 5mm and the initial velocities follow the predictions of Equation (21). The drops reach their terminal velocity in less than 200 ms. Especially for the drop on PFTOS an additional oscillation is visible. This can of course not be predicted by the simple model but the oscillations decay in a similar time range as the terminal velocity is reached. Before the initial impact energy is dissipated and steady-state is reached the drops have travelled about 1 cm to 2 cm (insert in Figure 31).
For the PFOTS the drop continues to travel at almost constant velocity. In contrast, on the PDMS surfaces the drop velocity can change quite drastically over the length of the surface. An example can be seen in Figure 32. In contrast to Figure 31, a longer time range of 4 seconds is shown. Also, the pipette was positioned 2 cm before the camera, so that the initial impact energy has already dissipated when the drop reaches the camera. Nonetheless, the drop does not reach equilibrium but shows fairly strong velocity fluctuations. A second drop that moves over the same part of the surface will exhibit the same behaviour (Figure 32 in orange). The first reason that comes to mind is heterogeneity of the surface. Indeed the quasi-static hysteresis on a PDMS sample on glass can vary by 5° but for the PFOTS surfaces this values is only of 1.3° as reported in Table 5. That can disturb the balance of forces and thus accelerate or decelerate the drop locally. If adaptation plays a role on this surface it could actually reinforce the velocity fluctuations. According to the adaptive wetting theory, increasing velocity increases θ_A. Depending on the ratio of adaptation time scale, drop length and velocity also θ_R can be increased. For $v >> L/\tau_{SL}$ the drop passes fast enough over the surface, that the adaptation cannot equilibrate, increasing both contact angles and decreasing the dynamic hysteresis caused by adaptation. Thus, for a fast moving drop, less water can diffuse into the surface or the molecules cannot reorganise, rendering it less hydrophilic and increasing the velocity further. Of course in the real system this mechanism will be limited by viscous dissipation and contact line friction, but could still lead to a reinforcement of velocity fluctuations.
Considering the heterogeneity of the surface and the possible reinforcement by adaptation, it is therefore important to carry out the contact angle measurements without changing the position

during experiment. Furthermore, it can be seen that the setup is highly sensitive to a shift in force balance. This is an advantage for measuring even small changes in the interfacial energies. The velocity might be even more sensitive than the actual contact angles, as changes of a few degrees can lead to drastic velocity differences. On the other hand, increased sensitivity, as always, also makes the measurements susceptible to interference by unwanted effects as heterogeneity, drop path change or drop volume variations.

4.2 Dynamic contact angle hysteresis

After studying the dynamics of drop motion on the tilted plate, I measured the CAH in dependence of the velocity to test the functionality of the setup. The dynamic CAH can be measured over velocities of approximately three orders of magnitude. For changing the velocity, the inclination angle of the sample is varied. For this experiment a PDMS sample from batch 1 was used and compared to the PFOTS coated wafer. The drop volumes were $(33.5 \pm 0.3)\,\mu$L on PFOTS and $(17.6 \pm 0.3)\,\mu$L on PDMS. On PFOTS a larger drop volume is required due to the higher static CAH. Temperature was $T = 21°$C for both experiments, relative humidity was $RH = 38\%$ for experiments on PFTOS and $RH = 48\%$ on PDMS. The pipette was positioned in a way that the drop impact is about 4 cm ahead of the camera's FOV. As discussed in Section 4.1 the initial impact energy dissipates very fast. To prevent that the results are affected by surface inhomogeneity the contact angle was always measured at the same spot on the sample. Furthermore, in between drops an ionising air blower (IAB) was used for 5 minutes to dry the surface and remove possible charges on the surface.

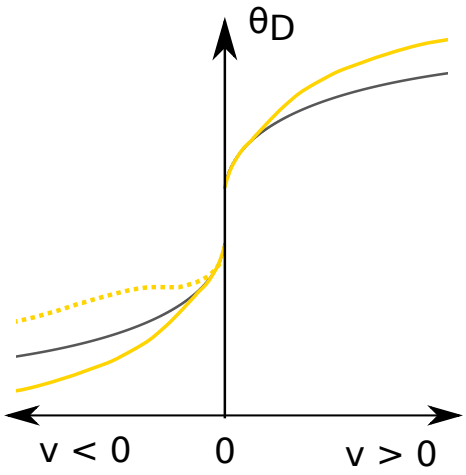

Figure 33: Schematic illustration of the expected dynamic CAH on adaptive and non-adaptive surfaces. The black curve shows the dynamic CAH for a non-adaptive surface. The yellow curves show the CAH for adaptive surfaces that have the same static contact angles. The CAH for adaptive surfaces is a combination of both adaptation caused CAH and the usual CAH dynamics. The receding angle can be increased or decreased compared to non-adaptive surfaces. The sign of the adaptive component of CAH depends on the velocity regime.

At first, I review the expected behaviour for both surfaces according to theory. For non-adaptive surfaces, the dynamic contact angle theories predict an increase of $\theta_A(v)$ and a decrease of $\theta_R(v)$ with increasing contact line velocities (Figure 6 in Section 2.3). As a result, the dynamic CAH

$$\mathrm{CAH}(v) = \theta_A(v) - \theta_R(v) \tag{36}$$

rises with v. This behaviour is attributed to viscous dissipation and contact line friction. For adaptive surfaces an additional origin of dynamic CAH exists. The adaptive wetting theory describes the additional component of CAH, which during experiments is expected to be observed in combination with the usual non-adaptive contact angle dynamics.

The influence of adaptation can only be observed for a specific range of velocities that depends on the relaxation time of the adaptation process. Velocities outside of this visible range lead to non-adaptive dynamics, because the drop moves either too fast, or too slow to be influenced by the change of interfacial energies (Section 2.4). Within the visible range, the adaptive wetting predicts the advancing angle $\theta_A(v)$ to increase with the velocity v. That means, that the usual dynamics are reinforced by adaptive wetting. The receding angle may either decrease with v or increase depending on the velocity regime (Section 2.4). In between the intermediate and high velocity regimes, the liquid-solid adaptation is so slow, that it does not equilibrate in the front of the drop but in the vicinity of the rear part. Therefore, a similar mechanism as for $\theta_A(v)$ is predicted: increasing the velocity decreases the adaptation of the solid-liquid interface and increases $\theta_R(v)$. In between the low and intermediate velocity regimes the liquid-solid interface equilibrates before the rear passes. In contrast, the liquid-gas interface at the rear cannot readapt to the gas completely. Increasing velocity decreases the readaption at the rear and decreases the receding contact angle. An exemplary schematic illustration of the adaptive vs. the non-adaptive wetting behaviour can be found in Figure 33. Both cases for the adaptive component of the receding contact angle are shown.

4.2.1 Qualitative observations

The results of the experiments for both surfaces are depicted in Figure 34. The advancing contact angles are plotted for positive velocities and the receding contact angles for negative velocities. Furthermore, the capillary numbers are given on the second x-axis. Each data point represents one drop and error bars give the standard deviation within the video of this drop. The data is shown for velocities from ca. 0.4 mm/s to ca. 10 cm/s.

Results on the reference sample

The dynamic contact angles on PFOTS show an approximately symmetric behaviour: the receding contact angle decreases with similar dependence on v as the advancing angle increases. The dynamic CAH increases from CAH(0.5mm/s)= 23° to CAH(90mm/s)= 40°. The average increase of CAH over v is therefore $\Delta\text{CAH}/\Delta v = 0.19°\text{s/mm}$ for the plotted velocity range. The behaviour is qualitatively as expected from theory.

Results on the PDMS brushes

For the contact angles on the PDMS brushes an asymmetric CAH can be seen. While the receding contact angle depends strongly on the contact line velocity, the advancing contact angle remains approximately constant within the investigated velocity range. The observation for $\theta_A(v)$ is unexpected. Even on non-adaptive surfaces an increase over v is expected. In the case of adaptation there should be an even stronger dependence on v. The adaptive wetting theory cannot explain why the velocity dependence of the advancing contact angle is decreased compared to the reference. It might be possible that adaptation not only changes the free surface energies, but also influences the physical properties that govern the non-adaptive contact angle dynamics. These parameters are slip length or friction coefficient for the common contact angle theories. For the MKT, e.g. the distance λ of adsorption sites might be changed by surface adaptation. This is sounds not unreasonable, especially for cases where adaptation originates from surface reconstruction. But at this point, it can only be hypothesised what the real causes of the observed dynamic CAH on PDMS brushes are.
Despite of the constant $\theta_A(v)$, the dynamic CAH on PDMS rises much faster with increasing velocity than on PFOTS due to the strong decrease of $\theta_R(v)$. At low velocities the hysteresis of the PDMS brushes is lower than for PFOTS, but already at v =1 cm/s it surpasses the dynamic CAH of PFTOS. The dynamic CAH on PDMS for the plotted range increases from CAH(0.4mm/s)= 14° to CAH(110mm/s)= 48°. The average increase for this range is $\Delta\text{CAH}/\Delta v = 0.31°\text{s/mm}$, and thus 60% higher than on PFTOS. For velocities of $1\,\text{mm/s} < v < 10\,\text{mm/s}$, the PDMS brushes show a much

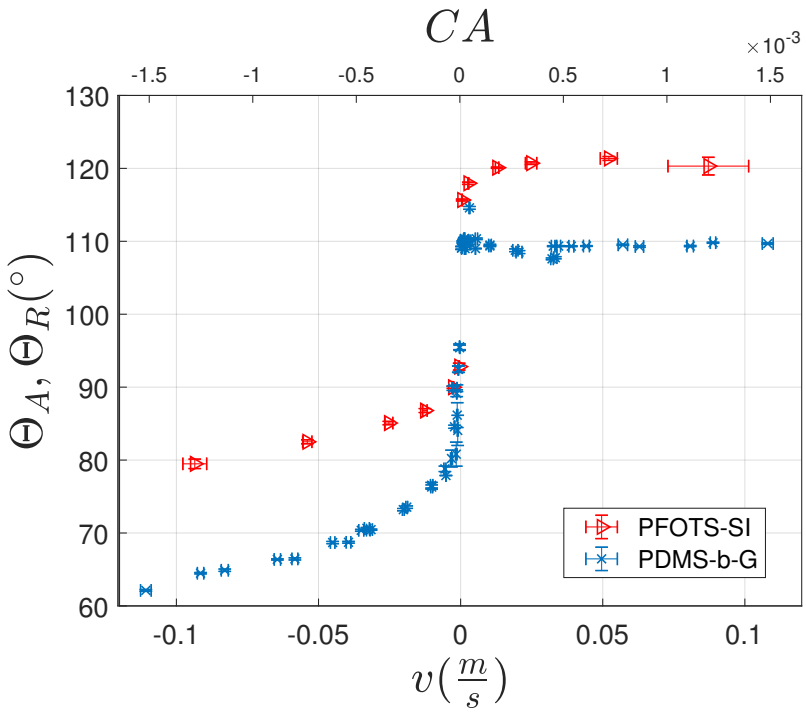

Figure 34: Dynamic contact angle hysteresis of water on PFOTS on silicon wafer and PDMS brushes (batch 1) on glass . The drop volumes were $(33.5 \pm 0.3)\,\mu$L and $(17.6 \pm 0.3)\,\mu$L respectively. Error bars are the standard deviation within the video of one drop.

stronger decrease of $\theta_R(v)$ than the PFOTS surfaces. For $v > 10\,$mm/s the slope of both surfaces begins to be of the same magnitude. One possible explanation of this observation is indeed surface adaptation. The initial strong decrease could be explained by a superposition of non-adaptive dynamics and adaptive wetting. Of course, this difference could also be caused simply by differences in contact line friction. A reason for that could be an additional dissipative process in the surface. The PDMS brushes are flexible and notwithstanding the small film thickness elastic deformations similar to those on crosslinked PDMS might happen on the nanometer scale. These could lead to viscoelastic dissipation. Lhermerout et al. have recently published a paper studying the dynamic CAH on thin film brush-like PDMS [30] for varying chain lengths. They found, that longer chains in the film, lead to higher layer thickness and a much stronger increase of the dynamic CAH at small capillary numbers. They interpreted this observation as an increase of viscoelastic dissipation in the PDMS film. However, the viscoelastic dissipation would predict also an increased velocity dependence for the advancing contact angle. The opposite was observed in my experiment and the dynamic CAH shows a strong asymmetry.

Asymmetry in the dynamic CAH has been reported before, for structured surfaces and smooth PTFE [85]. Kim et al. have also observed a velocity independent advancing contact angle for superhydrophobic surfaces similar to my observations on the PDMS brushes [85]. Omori et al. investigated the asymmetry by means of molecular dynamics simulations [86] and observed a density change near the contact line that leads to increased friction for the receding part. It remains an open question if this explanation holds for almost incompressible fluids as water. In the case of adaptive wetting, the asymmetry can be explained by different adaptation time scales for the process at the front and at the rear. In the next step, the results are compared to the dynamic contact angle theories by fitting to see whether the data on PFTS and PDMS brushes can be described quantitatively.

Table 6: Fitting parameters on PFTOS for the best fit.

Theory	Parameter name	Value for $\theta_A(v)$	Value for $\theta_R(v)$
Molecular kinetic theory (MKT)	$\theta^{\infty}(°)$	114	90
	λ(nm)	3	1
	κ_0(MH)	0.03	40
Hydrodynamic theory	$\theta^{\infty}(°)$	119	89
	$\ln(L_v/L_s)$	400	700

Table 7: Fitting parameters on PDMS (batch 1). Values for τ_{SG} and τ_{SL} are calculated from fitting parameter τ_ϵ/l_ϵ assuming $l_\epsilon = 10$nm for $\epsilon = \{SG, SL\}$ respectively.

Theory	Parameter name	Value for $\theta_A(v)$	Value for $\theta_R(v)$
Molecular kinetic theory (MKT)	$\theta^{\infty}(°)$	110	91
	λ(nm)	5	1
	κ_0(MH)	0.5	0.6
Hydrodynamic theory	$\theta^{\infty}(°)$	110	85
	$\ln(L_v/L_s)$	100	2000
Adaptive wetting theory	$\theta^{\infty}(°)$	-	88
	$\Delta\gamma_{SG}$ (mN/m)	-	30
	τ_{SL} (μs)	$\tau_{SL} << 0.1$ or $25 << \tau_{SL} << 4 \cdot 10^4$	$\tau_{SL} << 0.1$ or $25 << \tau_{SL} << 4 \cdot 10^4$
	τ_{SG} (μs)	-	2
Combined adaptive molecular kinetic theory	$\theta^{\infty}(°)$	-	96
	$\Delta\gamma_{SG}$ (mN/m)	-	9
	τ_{SG} (μs)	-	70
	λ(nm)	-	1
	κ_0(MH)	-	1

4.2.2 Fitting to theory

Results on the reference sample

At first, the behaviour of the reference case is discussed, i.e. for the PFOTS coated silicon wafer. For comparison to theory, the MKT and the hydrodynamic theory were fitted to the results using the *fit* function included in *MATLAB*. The results are split into two diagrams for the both contact angles, for better clarity. Also, different fits were done for both sides. That is necessary as none of the theories account for static CAH. The static Young's angle therefore has to be replaced by the static advancing or receding contact angle respectively. These angles were also used as parameters and determined from the fit. Figure 35a shows the results for the advancing contact angle and Figure 35b for the receding contact angle. The fitting parameter values for the best fit can be found in Table 6.

The hydrodynamic theory is not able to fit well, possibly due to the strong velocity dependence for rather small capillary numbers. Cross-over between thermally activated processes - that are modelled by MKT - and hydrodynamic regime is expected to happen in the vicinity of the depinning transition [87], although interestingly MKT is able to describe processes much faster than that [1]. For a fluorinated surface, as PFOTS is, Snoeijer et al. estimated the cross-over to happen between $CA \sim 10^{-5}$ and $CA \sim 10^{-4}$ [87]. Therefore, the hydrodynamic model is incapable of describing the strong contact angle increase for lower capillary numbers. A similar observation was made by Blake et al. on PET [1] (Figure 36).

Fitting the MKT results in a better description of the contact angles. The distance of adsorption sites for the best fit is in a molecular range of λ_A =3 nm and λ_R =1 nm for advancing and receding contact angle. Values differ due to the slight asymmetry that is present on PFOTS, too. Furthermore, only few data points were measured and therefore the fit is less reliable. For that reason, the hopping rates vary between the orders of $\kappa_0 \sim 10kHz$ and $\kappa_0 \sim 10MHz$. Nonetheless, the parameter values for the best

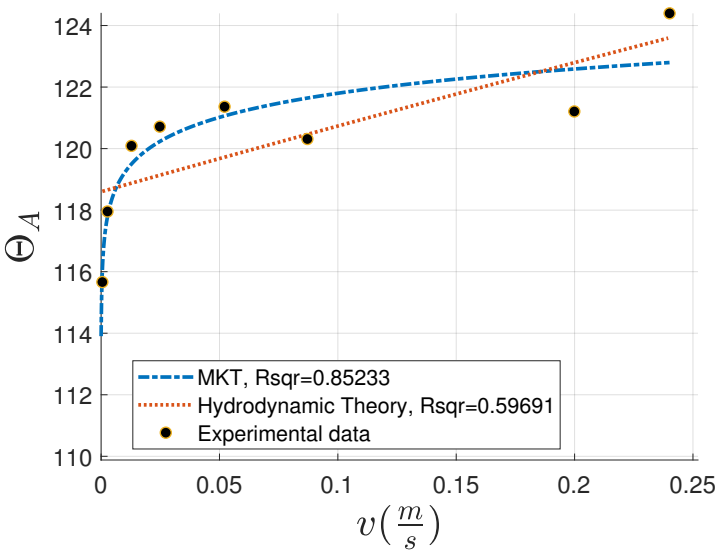

(a) Advancing contact angle $\theta_A(v)$ for water on PFOTS and fitted MKT (dashed, blue) and hydrodynamic theory (dotted, orange). Fitting parameters can be found in Table 6.

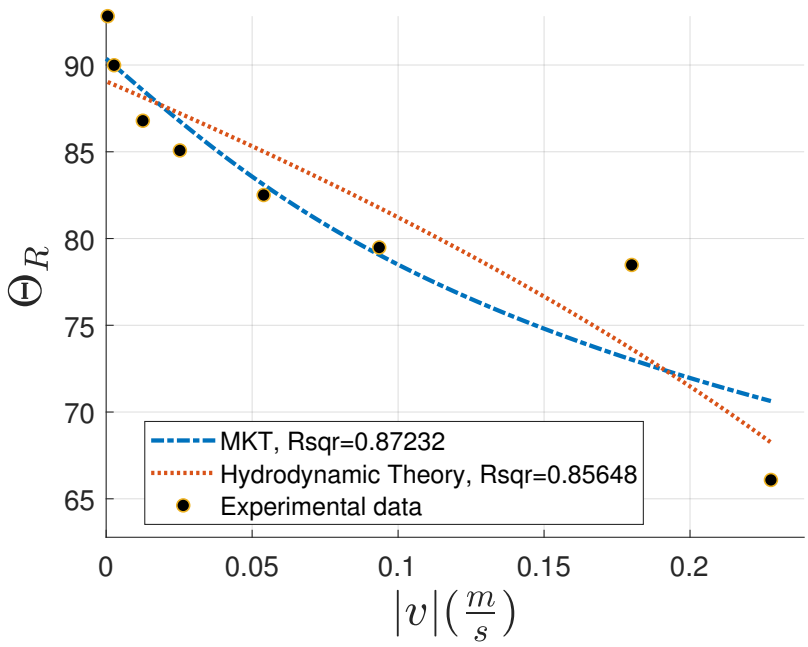

(b) Receding contact angle $\theta_R(v)$ for water on PFOTS and fitted MKT (dashed, blue) and hydrodynamic theory (dotted, orange). Fitting parameters can be found in Table 6.

Figure 35: Measurement results for dynamic contact angles of water on a PFOTS coated silicon wafer.

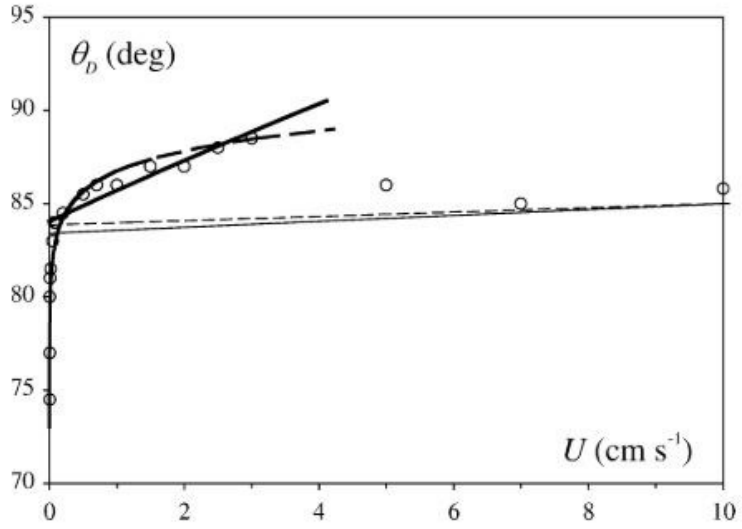

Figure 36: Advancing angle $\theta_A(v)$ as measured by Blake et al. for aqueous glycerol solution on PET. Dashed lines show fits to the MKT, solid lines to the hydrodynamic theory. The bold lines are fits to the low-velocity regime, thin lines for the high-velocity regime outside of the scale of this diagram. Taken from [1].

fit lie well within the usual and physically acceptable range [1]. Although the fit describes correctly the dependence for small velocities, the values measured for $v > 5$ cm/s do not align well with the model and apparently show some noise. This could be the start of a transition towards a different regime, similar to the measurements of Blake et al. on PET, where a decrease and subsequent increase of $\theta_A(v)$ was found for similar velocities (Figure 36) [1] [20]. They found an unsteady transition with stick-slip behaviour from low speed to a high-speed mode with different contact angle dynamics. It was suggesteted that this transition is caused by interactions with polar sites on the surface for low speeds, which are shielded by entrainment of air molecules for the high-speed regime[20]. A transition might also be caused by adaptive processes. More likely, the observations originate from measurement errors as the measurement was only done once, and deviation from the MKT predictions is of less than 2°. Repetition of the measurement with additional drops at higher speeds would be necessary to identify if transition exists.

Results on the PDMS brushes

As mentioned, it is difficult to prove adaptation only from measurements of the dynamic CAH. One reason is the coexistence of multiple causes of dynamic CAH (adaptive and non-adaptive) that cannot be easily separated. Therefore, the proof of adaptation is not the aim of this experiment. Still, the quantitative analysis can give some hints about adaptive time scales and serve as a proof of concept that adaptive wetting theory can be investigated on the setup. But it must be emphasised that additional investigations by alternative methods are required to make concluding remarks on the existence of a adaptation process. Although PFOTS was used as a non-adaptive reference with similar static wetting properties, a difference in dynamics is not necessarily caused by adaptation. Therefore, only a hypothetical analysis of the results can be done with respect to the adaptive wetting theory.
As the advancing angle is approximately constant, no adaptive theory was fitted to $\theta_A(v)$. If adaptation exists on the PDMS surface, it might be too fast or too slow to influence $\theta_A(v)$ within the tested experiments. From theory we can estimate some limits of the adaptation velocity. In the following, I will refer to the different states of the surface as 'dry' and 'wet' state to facilitate the discussion following Butt et al. [8]. The 'dry' state refers to the state of the surface directly before the first contact with the drop. The 'wet' state denotes the condition when in contact with water for sufficient time for the surface to equilibrate. The surface may actually not take up any water, but rather adapt

by a change of surface composition or surface charge. Thus, the wet state not necessarily refers to the water content of the solid surface.
As explained in Section 2.4, two different adaptation time scales are expected to affect the dynamic contact angles. τ_{SL} and τ_{SG} characterise the adaptation at the solid-liquid and solid-gas interface respectively. The former one is the adaptation from the dry state to the wet state when the drop contacts the solid. The latter one is the reverse adaptation from wet to dry state behind the drop. The advancing contact angle is governed by τ_{SL}. When the ratio of peripheral thickness and relaxation time is in the order of the contact line velocity $l_{SL}/\tau_{SL} \sim v$, according to Equation(17) θ_A increases with v. Assuming that the advancing angle is velocity dependent for smaller or higher velocities than the measured range of 0.4 mm/s to 10 cm/s we can say

$$l_{SL}/\tau_{SL} << 0.4\,\text{mm/s, or } l_{SL}/\tau_{SL} >> 10\,\text{cm/s} \tag{37}$$

The adaptation is too slow or too fast to increase $\theta_A(v)$ within the measured velocities. From Equation (37) one can estimate

$$\tau_{SL} >> 25\mu\text{s or } \tau_{SL} << 0.1\mu\text{s}, \tag{38}$$

assuming the peripheral thickness l_{SL} =10 nm as proposed by Butt et al.

For the receding contact angle two scenarios of the adaptive influence exist: increasing or decreasing $\theta_R(v)$. The increase is governed by solid-liquid adaptation τ_{SL}, while the decrease is governed by solid-gas adaptation τ_{SG}. No increase of $\theta_R(v)$ with v was found. The adaptation governed by τ_{SL}, from dry to wet state, can therefore be either non-existent or outside of the measurable range of this experiment. The latter includes time scales that correspond to an adaptation to the wet state that has already equilibrated when the rear part passes:

$$l_{SL}/\tau_{SL} << v << L/\tau_{SL} \tag{39}$$

Assuming that this is true, one can calculate 25μs$<< \tau_{SL} <<$ 40ms for the drop length of ca. 4 mm. Behind the rear part of the drop the surface starts to re-adapt to the new surrounding medium, air. The surface properties eventually return to the dry state. This process is only characterised by the time scale of solid-gas adaptation τ_{SG}. Depending on drop velocity and τ_{SG} that process thus may affect $\theta_R(v)$ (Section 2.4) and $\theta_R(v)$ can be described by Equation (18). In other words, the completely wetted surface reverses from the wet to a dry state at the rear part of the drop, leading to a change of γ_{SG} and thus $\theta_R(v)$. It is possible that $\tau_{SG} \neq \tau_{SL}$ and that this part of the adaptive process is visible. Therefore the receding angle is studied in more detail in the next paragraph.
The receding contact angle on PDMS follows a very similar behaviour as for the PFOTS surfaces: A strong decrease of $\theta_R(v)$ can be observed for small capillary numbers. The MKT and the hydrodynamic theory, the adaptive wetting theory and the combination of MKT and adaptive wetting were fitted. The parameter values can be found in Table 7. MKT leads to a good fit for a large velocity range. The parameters are $\theta_R^\infty = 91°$, λ =1 nm and κ_0 =600 kHz and in physically plausible orders of magnitude. The hydrodynamic theory again fails to describe the strong contact angle change for low capillary numbers.
To test the performance of the adaptive wetting theory, Equation(18) is used. In a first step, the adaptive wetting theory is fitted without combining it with a non-adaptive theory like MKT or hydrodynamic theory. Equation (18) yields a good fit for $v \leq$6 cm, but does not predict a further decrease of $\theta_R(v)$ for higher velocities. Fitting parameters can be found in Table 7 as well. The reason for the deviation at higher velocities is that viscous dissipation and contact line friction are not accounted for

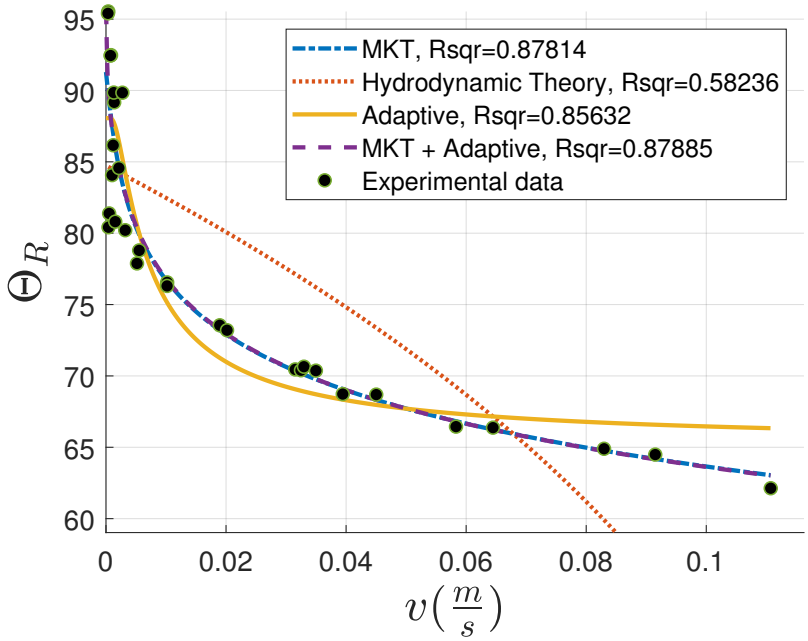

Figure 37: Receding contact angle $\theta_R(v)$ for water on PDMS (batch 1). Fitted theories were the MKT (dashed, blue), the hydrodynamic theory (dotted, orange), the adaptive wetting theory and the combination of MKT and adaptive wetting theory. The fitting parameters can be found in Table 7.

in the adaptive wetting theory. As adaptive wetting theory describes the mechanism of an additional cause of dynamic CAH, not an alternative one, it is logical to try to combine it with the MKT or hydrodynamic theory. This was proposed by Butt et al. [8]. Here, the combination with MKT is tested because the hydrodynamic regime apparently has not been reached as indicated by the poor fitting results on both surfaces. As explained previously, the MKT is based on the idea of energy barriers, that the liquid molecules have to overcome in order to move the contact line. The out-of-balance surface tension force $F_W = \gamma_{LG}(\cos\theta^\infty - \cos\theta_D(v))$ changes the energetic landscape by decreasing the barriers in the direction of contact line motion[35]. For the case of adaptive wetting, this force changes according to the state of the surface, and thus θ^∞ in MKT Equation (12) can be replaced by $\theta_R(v)$ or $\theta_A(v)$ from adaptive wetting. For the receding angle the combined model is:

$$v = 2\kappa_0\lambda\sinh[\gamma_{LG}(\cos\theta_R^\infty + \frac{\Delta\gamma_{SG}}{\gamma_{SG}^\infty}\, e^{-l_{SG}/v\tau_{SG}} - \cos\theta_R(v))\frac{\lambda^2}{2k_BT}] \tag{40}$$

in which the equilibrium angle is θ_R^∞ due to static hysteresis. This form of combination assumes, that the adaptation solely changes the free surface energy but not the distance of adsorption sites or the hopping rate. Due to the larger number of parameters and the nonlinear form, fitting for this model is not very stable and a more sophisticated fitting algorithm like bootstrap fitting should be considered in the case of a more detailed analysis in the future. Nonetheless, the combined model can describe the data very well and the parameters are of reasonable value (Table 7). Fitting parameters for the contribution of non-adaptive dynamics by MKT are of the same order as in the separate fit of MKT. For the adaptive component the adaptation time $\tau_{SG} = 70\mu s$ and the surface tension change is $\gamma_{SG} =$ 9 mN. Figure 38 shows the contribution of the adaptive wetting theory and the MKT separately. The

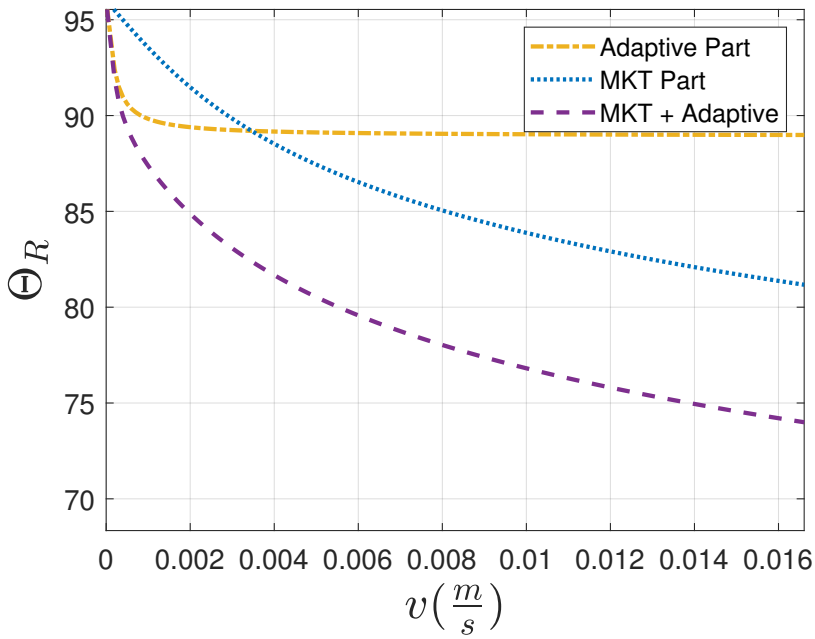

Figure 38: The contribution of the MKT and adaptive wetting theory plotted separately for the combined theory. The adaptive part accounts for the strong initial decrease, while the MKT represents the weak dependence for higher velocities

adaptive part accounts for the rapid decrease at low velocities, while the MKT describes the weak dependence for higher velocities.

In conclusion, the dynamic CAH of PDMS brushes and of a PFOTS coated silicon wafer were successfully measured. Thereby, the functionality of the setup has been proven and it was possible to compare the results to the different contact angle theories. The presumably non-adaptive surface behaved as expected and predicted by theory, while the PDMS brushes showed some unexpected results for the advancing contact angle. The MKT shows a good performance for most contact angles. In contrast, hydrodynamic theory is not able to yield a satisfying description of the data. The receding contact angle of the PDMS brushes was furthermore analysed with respect to the adaptive wetting theory yielding plausible parameters and good fitting results. That is a necessary but not sufficient condition for the verification of the adaptive wetting theory. Due to the lack of independent measurements to confirm adaptation on PDMS brushes, only hypothetical analysis of the results with respect to adaptive wetting could be done. Under the hypothesis that adaptation takes place, I was able to narrow down the time scale for the solid-liquid interface. Furthermore, the receding angles can only be affected by adaptation if $\tau_{SL} \neq \tau_{SG}$. However, for the range of capillary numbers studied, the dynamic CAH will always be affected by additional dynamic processes, that are described by MKT and the hydrodynamic theory. Therefore, a combination of MKT and adaptive wetting theory was tested and has shown improved fitting performance compared to the adaptive wetting theory. The CAH has a much stronger increase for low velocities on the PDMS brushes. Adaptation in combination with MKT can explain this stronger dependence of the CAH on velocity, as adaptation reinforces that dependence. But without additional measurements it cannot be concluded to which extend, if at all, surface adaptation influences the results. Nonetheless, the setup full-fills the desired functions and can be used in the future in combination with complementary methods to analyse the adaptive wetting theory in more detail.

Apart from the contact angle hysteresis, also the drop motion dynamics are of interest. For measuring the dynamic CAH at a certain velocity, the inclination angle has to be adjusted. Therefore understanding the dependence of v on α facilitates the correct adjustment of α. Following the discussions of the initial dynamics in the last Section, the terminal velocity can be calculated. For the steady-state velocity one finds

$$\lim_{t\to\infty} v(t) = \frac{\Pi_1}{\Pi_2} = \frac{m\,g\,\sin\alpha - 24/\pi^3 \cdot \gamma_{LG} D(\cos\theta_R^\infty - \cos\theta_A^\infty)}{48 D\zeta/\pi^3} \tag{41}$$

This result is compared with terminal velocity estimations from Kim et al. [77]. For the energy balance Kim et al. assumed a static hysteresis over the whole velocity range. Indeed dynamic contact angles were found to change negligibly compared to the static hysteresis for their experiments. The viscous dissipation was modelled separately based on a Stokes flow in the wedge of the drop for small drops. The following scaling law for the terminal steady state velocity was deduced:

$$\lim_{t\to\infty} v(t) \sim \frac{m\,g\,\sin\alpha - \gamma_{LG} D(\cos\theta_R^\infty - \cos\theta_A^\infty)}{\mu L_p c(\theta)\ln(L/L_m)} \tag{42}$$

in which $c(\theta)$ is a function the contact angle describing the amount of dissipation and L_p, L, and L_m are the peripheral length of the drop/solid contact area, the macroscopic length scale and the microscopic length scale respectively. L and L_m are defined analogously to hydrodynamic contact angle theory (Section 2.3.1). As can be seen, the dependence on static hysteresis, inclination angle, viscosity and the Young's static contact angle is very similar to my model. The two latter dependencies are included in ζ. Difference origins mostly from the hydrodynamic approach by Kim compared to the MKT approach for Equation (41). Both equations predict a linear dependence on $\sin\alpha$.
Figure 39 shows the measured velocities over $\sin\alpha$ for both surfaces. It is clearly visible that the velocities do not follow a linear relationship with $\sin\alpha$. This can be explained by the fact, that the linear approximation of the MKT and the hydrodynamic theory are not suitable to describe the real dynamic CAH due to the fast increase at slow capillary numbers. The linearised MKT was replaced by the original version of the MKT, because it describes the dynamic CAH on both surfaces well. Equation (26) and (25) were solved numerically and the result is plotted in Fig. 39 as well. Additionally, a linear function was fitted to represent Equation (42) and (41). The usage of the nonlinear MKT leads to a much better approximation than predictions of Kim et al. and Equation(41). Deviations can be explained by uncertainties of equivalent drop diameter. The true equivalent diameter of the drop is unknown, as only the length can be measured. I assume a constant base area, and thus a constant equivalent diameter as the drop's width should decrease and the length should increase for higher velocities [59]. Having measured, the dynamic CAH allows to solve Equation (27) for the transient case as well. Comparison of the numerical results to the measured initial drop dynamics studied in the last section show a good agreement (Figure 40).

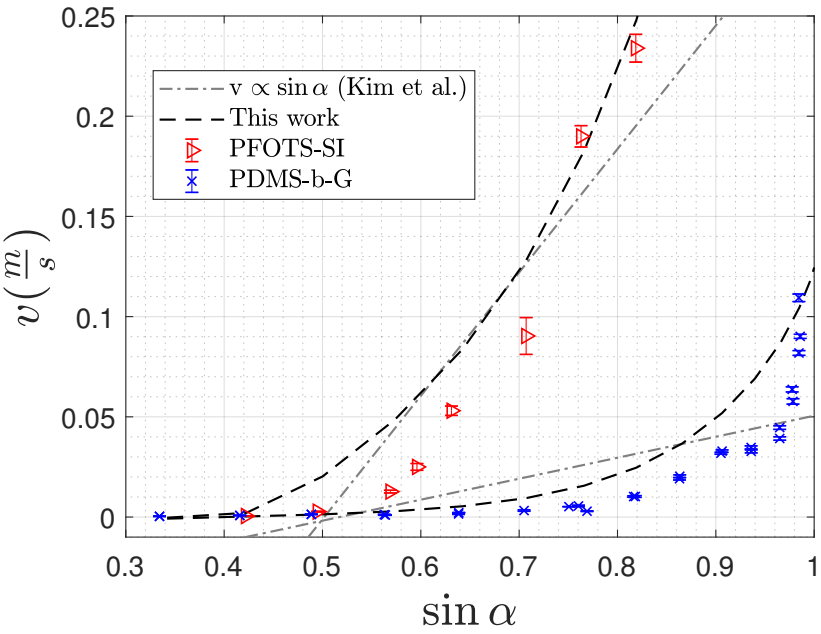

Figure 39: Drop velocities over the sinus of the inclination angle for water on PFOTS and PDMS brushes. The drop volumes were $(33.5 \pm 0.3)\,\mu\mathrm{L}$ and $(17.6 \pm 0.3)\,\mu\mathrm{L}$ respectively. Calculation by Equation (26) and (25) using the MKT is plotted in black. A linear fit representing linear dependence according to Equation (42) and (41) is plotted in grey.

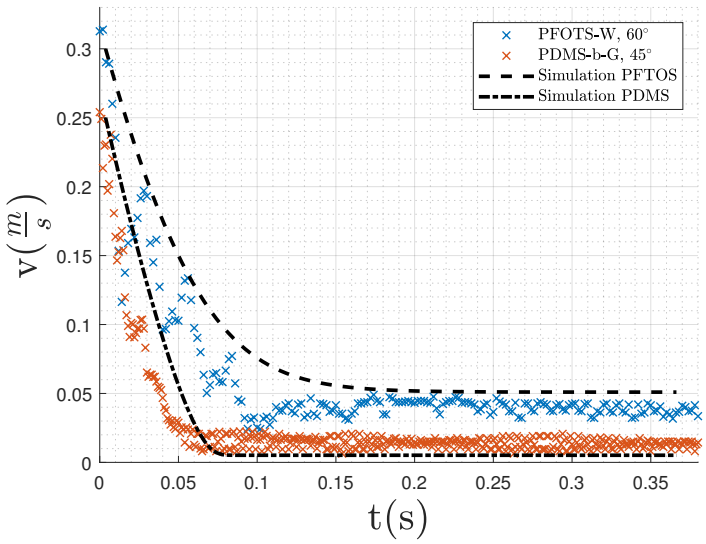

Figure 40: Comparison of numerical solution of Equation (27) to measurement results of the initial drop dynamics. The drop volume was $(17.6 \pm 0.3)\,\mu\mathrm{L}$ on both surfaces. See Appendix for contact angle and force curves of the simulation (Figure 52).

4.3 Drop-wise adaptation

Furthermore, I tested the PDMS surfaces for slow adaptations, outside of the ranges that would influence the dynamic CAH measured in the last Section. Slow adaptations might be observable over a number of drops. The condition for that is, that the reverse adaptation, equilibrating to the surrounding air, takes longer than the time passing between drops.

4.3.1 Measurements on the high-speed goniometer

For the drop wise adaptation, a series of 22 drops with a time of 6 seconds in between was pipetted onto the surface using the syringe pump. The inclination angle was α =45°. This analysis also helps to understand in which way possible adaptations can be reversed and how experiments can be conducted under repeatable conditions. Therefore, the series of drops was repeated various times and different strategies to reverse adaptation were applied in between runs. Three hypotheses can be made to reverse the adaptation: molecular reorganization could be reversed simply by waiting. If water diffuses into the surface and swells it, waiting can also evaporate the water and reverse the surface to a dry state. If charging of the surface plays a role, an ionising air blower (IAB) allows to remove the surface charge. The blower additionally increases the air flow and therefore evaporation. For this reason, the third strategy is blowing of NO_2 onto the surface to be able to distinguish effects from the ions in the air and the increased gas flow. The experiment was conducted twice in a similar manner on two different PDMS brush surfaces from different production batches. The results of both experiments show contrary behaviour, but trends within each of the experiments were repeatable. In the following, both experiments will be discussed and possible reasons for differences are also mentioned.

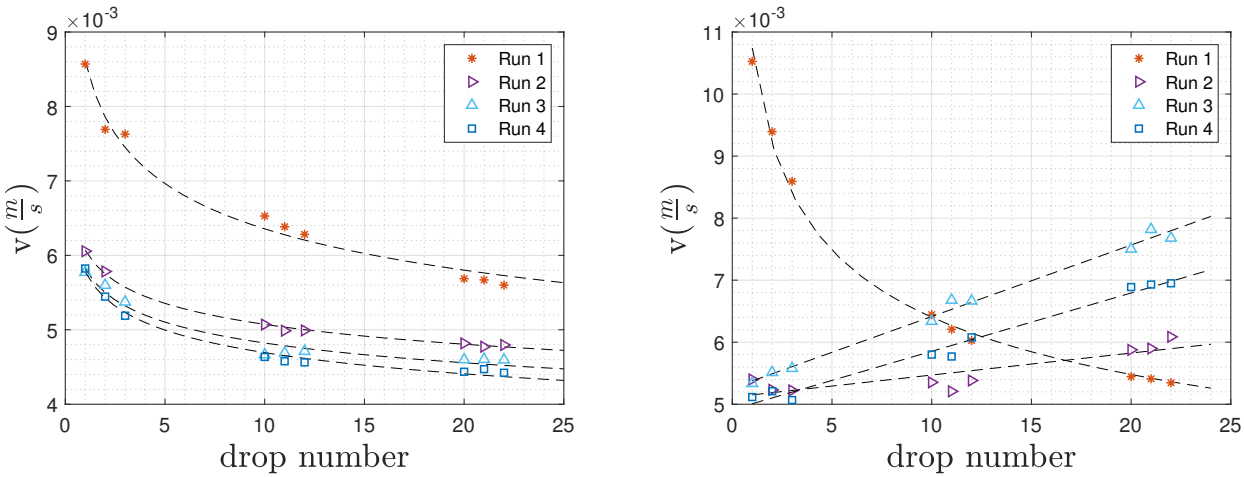

(a) Results for batch 2

(b) Results for batch 1

Figure 41: Drop velocities over drop number for the first runs. Dashed lines are exponential or linear fits to guide the eye

The experiment on the first surface (from batch 2) were structured as follows: one experimental run consists of a series of 22 drops. The first run was conducted on the new, unused surface. Then 4 runs were conducted with 10 minutes waiting time in between. After waiting 60 minutes three runs were conducted with 10 minutes of NO_2 blowing onto the surface. After waiting another 60 minutes another three runs were conducted with 10 minutes of IAB in between.
For the first surface, the velocity was found to decay within each run. Waiting in between the runs did not recover the velocity completely. Figure 41a shows exemplary the velocities of the first 4 runs. The decay follows an exponential behaviour. For the following runs only an overview is given. Figure

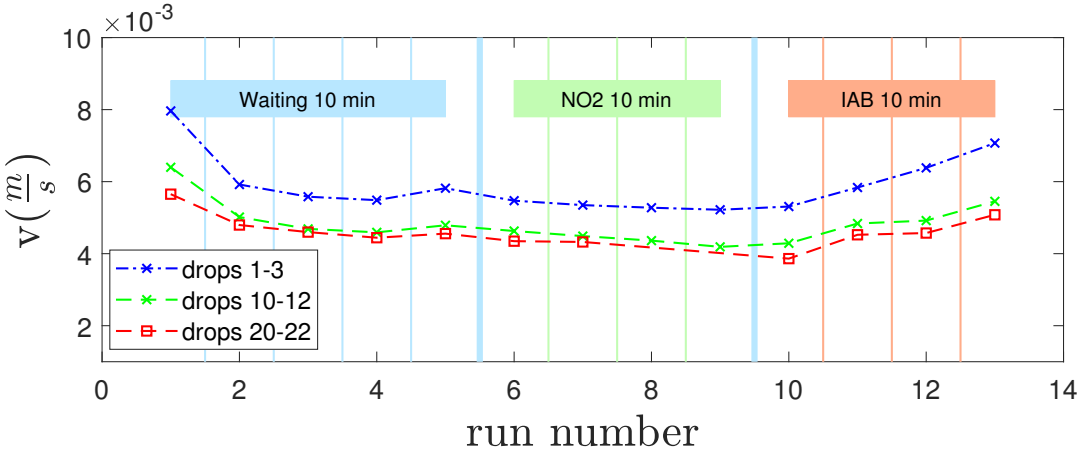

(a) Results for sample 1

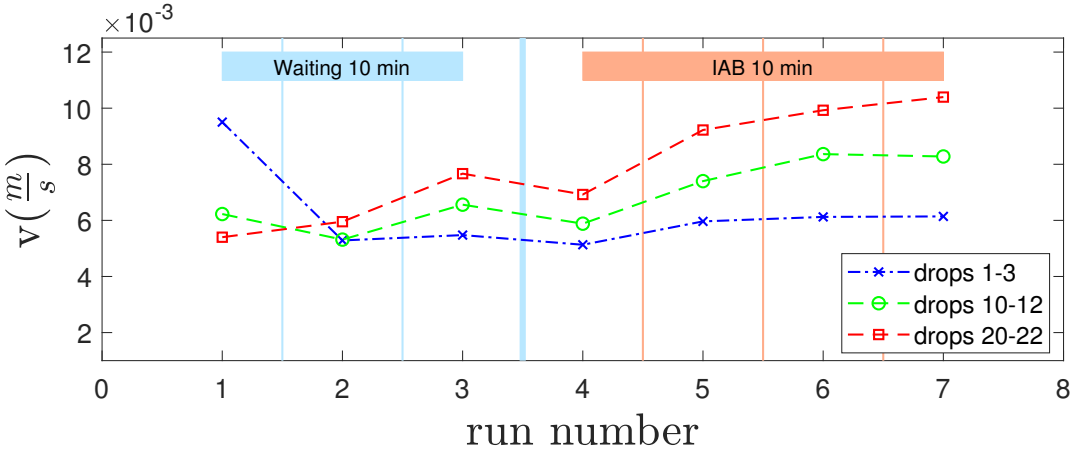

(b) Results for sample 2

Figure 42: Drop velocities over case numbers. Drop velocities are averaged in triples and the three plot lines give the average velocity drop 1-3, 10-12 and 20-22. Thin vertical lines indicate a time of 10 minutes in between runs. The bold vertical lines indicate a waiting time of 60 minutes.

42a shows the velocities over the run number. The blue line shows the averaged velocity for the first three drops of each run. The green and red show the averaged velocity for drop 10-12 and 20-22 respectively. For alls runs the velocities decrease within the run, i.e. over drop number. The first run shows generally the fastest velocities, and the following runs show lower and almost constant levels of initial and final velocities.Waiting or NO_2 blowing increases the velocity again, but not to the level of the first run. Waiting for 60 minutes does not change this. This partial recovery of the initial velocity thus seems to happen for waiting time of less than 10 minutes. In contrast, for the IAB an increase of velocity was found after every run. After three runs with using the IAB in between almost the initial state of run 1 is reached again. In order to check if the tendencies found in the first experiment are repeatable, a second experiment was conducted on another sample. Both samples were prepared in the same way but in different batches.
For the repetition on another sample (from batch 1) fewer runs were conducted and NO_2 was not used as it had shown no difference in comparison with waiting. The results for the first four runs are again plotted over the drop number in Figure 41b. The first run followed the same behaviour as in

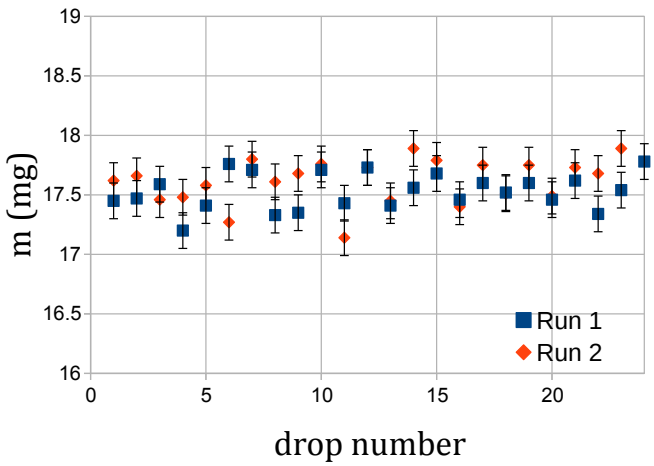

Figure 43: Drop weights measured with a micro scale over a series of drops (blue) and the repetition (orange).

the last experiment but the following three runs show a completely opposite tendency: drop velocity increases for later drops. This increase seems to follow a rather linear dependence, furthermore the slope changes. Again, the drop velocities are averaged in triples and plotted for all runs in Figure 42b. Here, waiting time of 60 minutes does show a change in comparison to 10 minutes and decreases velocity and slope of the increase. Using the IAB seems to continue the previous trend of increasing slope over run number.

The results are not consistent with the findings of the first experiment (except for run number 1). Possible reasons for that are numerous and can even be the interaction of multiple phenomena. The possible causes can be divided into three categories: differences of the surface properties, differences of the ambient conditions and differences of the experimental setup. A slight change of the surface properties can exist in between batches and samples. Quasi-static advancing contact angles on the first surface were 3° higher for θ_A*. That means, that there was clearly a difference in the chemical properties or roughness of the surface. Additionally, the samples show heterogeneity and thus testing at different spots might have an influence on the dynamics. A difference in ambient conditions might only play a minor role, because of a change in relative humidity from $RH = 41.7\%$ at $T = 21.5°\mathrm{C}$ in the first case and $RH = 52.0\%$ at $T = 20.2°\mathrm{C}$ in the second. Furthermore, slight differences in the experimental setup cannot be avoided: slightly different pipette height and distance from the camera are possible but should the should already have reached steady-state where these two parameters play no role any more. Apart from that, the drop size might change slightly in between experiments or even over the time of the experiment due to the flexibility of the tube and could explain velocity differences.

To exclude that, I measured the drop weights over a series of drops on a micro scale. The micro scale needs some time to equilibrate and within the time of 6 seconds between drops had an accuracy of approximately ±0.3 mg. The results for two experiments can be seen in Figure 43. No significant drift of weight over drop number was found and the standard deviation of the measured values is of 1%. Nonetheless, changes below the measurement accuracy are possible. From the maximum deviation within these weight measurements, the maximum gravity deviation can be calculated to be $5.2\,\mu$N for $\alpha = 45°$. All these factors can change the measured velocities on the surface, especially because the setup is very sensitive. But they do not deliver an explanation for completely reversed observations.

An additional experiment was done to see if the tendencies of decreasing or increasing drop speed with drop number continues if more drops are used. On the second surface sample (batch 1) two

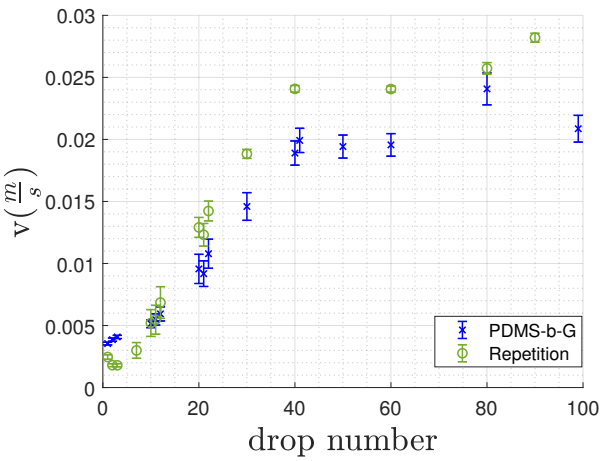

(a) Drop velocities

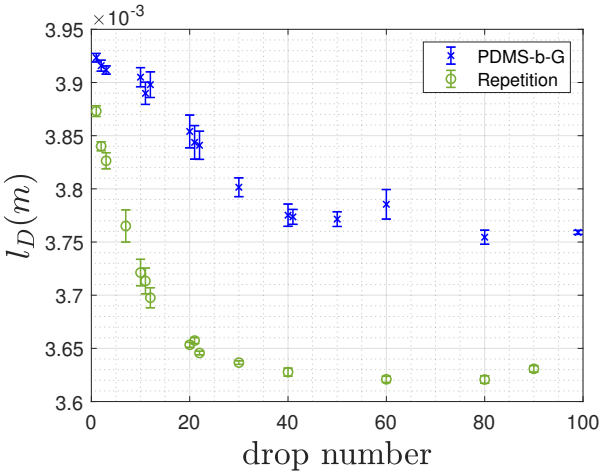

(b) Drop lengths

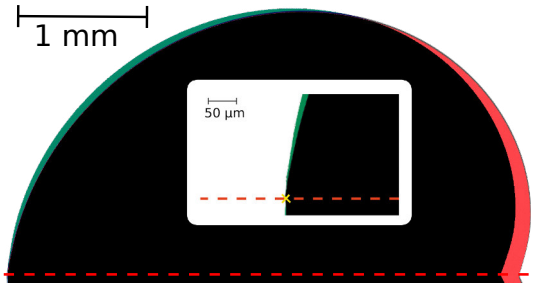

(c) Comparison of drop number 1 and number 60 by overlay. The green part at the rear shows drop 100. The red part at the front shows drop 1. The black part show areas both drops share. The red dashed line marks the base line. The insertion shows a comparison of the magnified rear part.

Figure 44: Comparison of a series of 100 drops.

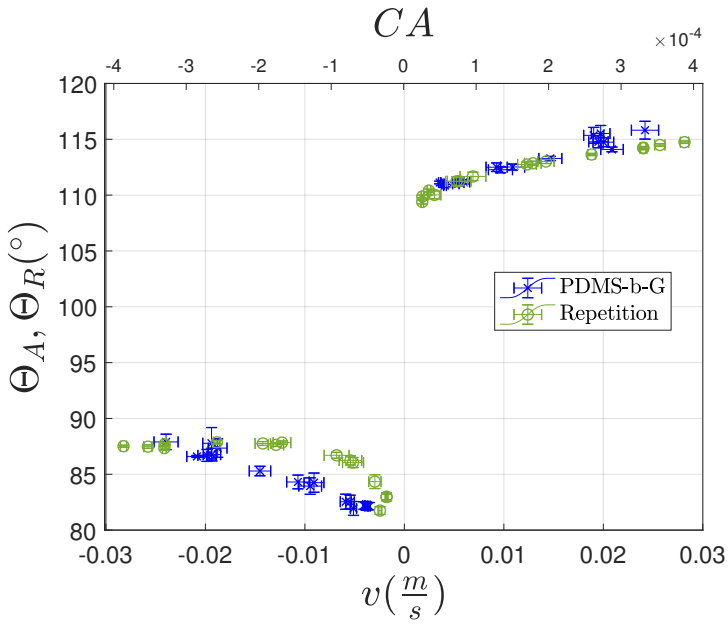

Figure 45: Contact angles for a series of 100 drops. Faster drops have higher contact angles

more runs were done, this time with 100 drops. The result can be seen in Figure 44. The velocity increases almost linearly within the first 40 drops and then saturates. After waiting 10 minutes, the second run shows qualitatively the same behaviour, although velocities differ. For the first 40 drops I could observe a significant increase of both advancing and receding angle. Especially interesting is the increase of the receding angle. Usually, faster drops have a lower $\theta_R(v)$, but here it is the other way around. Figure 45 shows the contact angles for the measured drops in dependence of their velocity. Faster drops, i.e. drops of higher drop number, have higher $\theta_R(v)$ and $\theta_A(v)$. Hysteresis maintains almost constant values for higher velocities in strong contrast to the measurements done for single drops in Section 4.2. This change of contact angle over drop number can explain the speeding up of the drops by two mechanisms. First, the increase of both contact angles decreases the base area of the drop. As adhesion force is proportional to the base diameter it also decreases. That can actually be seen in the lengths that decrease with the number of drops (Figure 44b). Second, the dynamic CAH remains almost constant although velocities increase more than four fold. That means that either, the static CAH has decreased or the dependence of the dynamic CAH on velocity has changed. In both ways, the dynamic adhesion force for a certain velocity is decreased and the drop accelerates until a higher velocity at which gravity and adhesion force are again in balance. Therefore later drops have higher velocity but similar hysteresis.

To see whether this is just a local effect, e.g. due to slight drop path change or defects, the experiment of 100 drops is repeated with the low magnification objective. In Figure 46 the velocity profiles over 3 cm length of the sample can be seen. The position of drop impact is at −1.5 cm. The velocity of drop 100 is ca. 8 times faster over the complete measurement length and confirms that the speed up is not a local effect. It has less data points as for this test all videos were taken at the same frame rate. Additionally, I analysed the drop radius before pinch off from the pipette and found no change within measurement uncertainty of ±2% (insert in Figure 46), in agreement with the previous weight measurements. The same test was done on a PFOTS coated glass and did show no significant difference of velocity (Appendix, Figure 53).

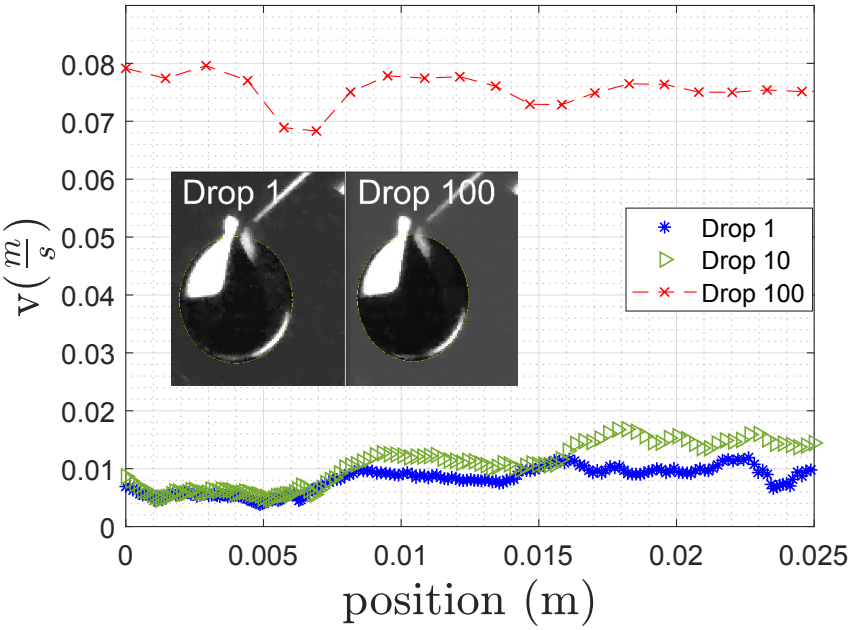

Figure 46: Drop velocities over the length of the sample taken at $1.5\,\mathrm{cm}$ distance of the impact position. Inset shows drop sizes of drop 1 and drop 100 before pinch off from the pipette. Drop radius does not vary within measuring accuracy and is $(1.59 \pm 0.03)\,\mathrm{mm}$

.

It was found that the drop wise adaptation can have an effect on the contact angle and velocity. This effect is reversed by a few minutes of waiting, although still some changes remain if the experiment is repeated afterwards. In the following I will discuss some hypotheses.
On crosslinked PDMS unbound polymer chains can cause speeding up of droplets. Hourlier-Fargette et al. found that these oligomers can be extracted by a water drop and build a film around it [88]. A water surface covered by PDMS oil will have a sudden decrease of surface tension when a critical surface concentration is passed. Hourlier-Fargette et al. observed, that the drop changes from a slow to a fast regime. Immersing the PDMS in a good solvent, e.g. toluene, can remove the uncrosslinked oligomers and prevent this behaviour[88]. For PDMS oil on a water surface the cricitcal surface concentration is 0.75 mg/m^2, which for my drop volumes leads to a critical quantity of $1.8\cot 10^{-5}$ mg of unbound PDMS per drop. I used 25 mg of PDMS per sample and the amount of toluene used to wash was 50 ml per sample. One can estimate that the PDMS is dissolved with a concentration of $\sim$ 0.5mg/ml in the Toluene. Assuming that the same concentration is left in the brush layer, the total amount of unbound PDMS in the complete sample can be estimated from film thickness and area to be in the order of $\sim \cot 10^{-6}$ mg. Therefore it is very unlikely that a drop which only extracts a small part of the oligomers in the film can reach the critical surface concentration. Also, the effect observed on cross-linked PDMS was not a drop-wise speed up, but a change of velocity for one single drop along the sample.
Another possible reasons for the observed speed up can also be a change of motion regime from sliding to rolling. But there the question remains by what this transition was caused. Change of surface roughness can explain an increase of the advancing angle by the Wenzel equation but would be expected to decrease the receding angle as it is below 90°. Water uptake and swelling of the surface would be expected to decrease contact angles as well [47]. Another hypothesis could be the formation

Table 8: Overview of roughness values measured by AFM

sample	rms (nm)
PDMS-b-g on the drop path	0.6
PDMS-b-g next to the drop path	1.7
uncleaned glass slide	1.6

of a liquid film with drop number. Drops can leave a thin film of liquid behind the receding contact line which increases the apparent solid surface free energy [19]. Again, this could only explain the cases of decreasing velocity as the film would decrease the receding angle [19], not increase it.
A more probable cause for the drop-wise speed up is charging of the drop and surface, which can create a Coloumb force [74]. Yatsuzuka et al. have measured that drops running down a teflon plate charge up positively and leave a negative net charge on the surface. A change of surface charge can have an influence on the contact angle and wetting kinetics [89],[90]. After a number of drops, the surface charge can saturate. The attraction between drop and surface could decrease and the drops might become faster. It is not known if this effect is strong enough to explain the observations on the PDMS brushes.

4.3.2 Additional measurements by other methods

To gain an idea of possible causes for the observations made in the last section, a few additional measurements have been done by alternative methods to characterise the surfaces.
First, an atomic force microscopy (AFM) measurement was done to investigate possible changes of the surface topography like roughening. Two spots of the sample were measured: one on the drop path, where a few hundred drops had passed, and another one next to the drop path, where no drops had passed. Measurements were carried out by Uwe Rietzler (Max Planck Institute for Polymer Research, Mainz). Results for the roughness can be found in Table 8. The AFM images taken on the drop path can be seen in Figure 47a and 47b. The surface is very flat with a roughness of rms =0.6 nm. Still, different structures can be found on the surface, that are not expected. Ring shaped structures with a diameter of approximately 50 nm and furthermore larger loops on the scale of micrometres are visible. These structures are too large to be the PDMS brushes, and were found to originate from the underlying glass (Figure 47 (d)). Comparison of glass slides from different boxes all showed similar structures. Interestingly, these structures were not removed by ultrasonicating 5 mintues in toluene and ethanol. Maybe a more thorough cleaning process is required, or the structures are not on top of the glass but rather structures of the glass from some production step. Although these structures are very flat and may not have any effect on the contact angle, for the future a preparation on silicon wafers is recommended. A test of preparing the PDMS brushes on a silicon wafer also decreased the heterogeneity significantly. The maximum difference of quasi-static CAH on the sample is 1° instead of 5° on glass.
Comparing to the AFM images taken next to the drop path shows that some additional contamination exists (Figure 47 (c)), that has been washed away by drops on the drop path. Therfore, the surface exhibits increased roughness of 1.7 nm. The higher value of the roughness is not necessariy related to higher roughness of the PDMS film itself, but could be only cuased by the partciles ontop. The AFM measurements were conducted a few hours after the last drop passed, so the differences cannot explain changes in velocity that occur during runs or from 10 minutes waiting time. It might explain a difference for the first drop, but generally one would expect a slower drop due to additional dissipation by the contamination. Environmental dust can be removed by the drop but creates additional retention force for the drop [91]. The first drops on the fresh samples were observed to be faster though, for both drop-wise adaptation tests. The contaminations probably stem either from the water in the last washing step during sample preparation or from contamination in air that settles during the

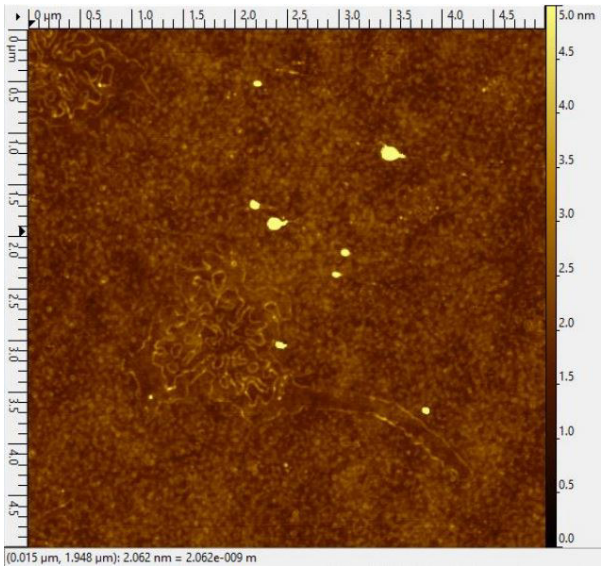

(a) PDMS brushes on drop path, $5\,\mu\mathrm{m} \times 5\,\mu\mathrm{m}$

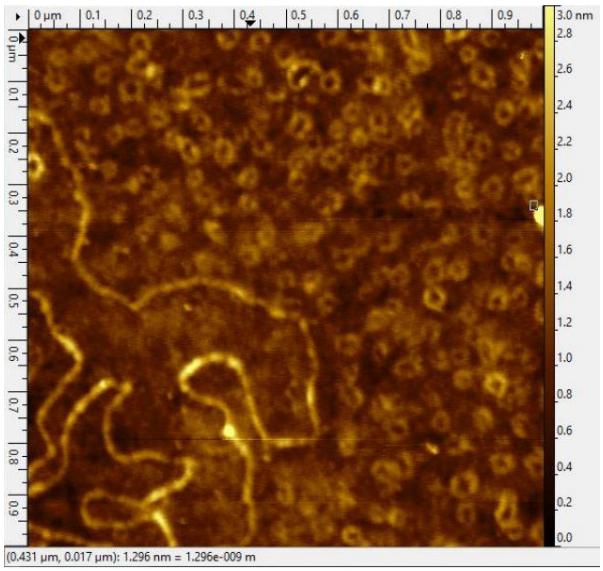

(b) PDMS brushes on drop path, $1\,\mu\mathrm{m} \times 1\,\mu\mathrm{m}$

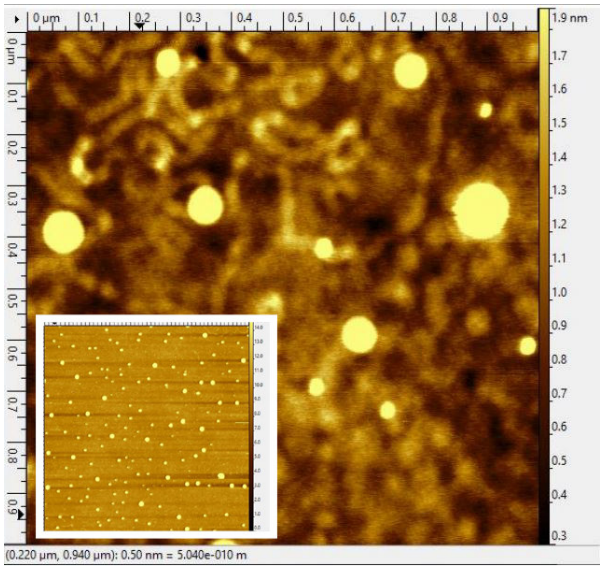

(c) PDMS brushes outside of drop path, $1\,\mu\mathrm{m} \times 1\,\mu\mathrm{m}$, insert $5\,\mu\mathrm{m} \times 5\,\mu\mathrm{m}$

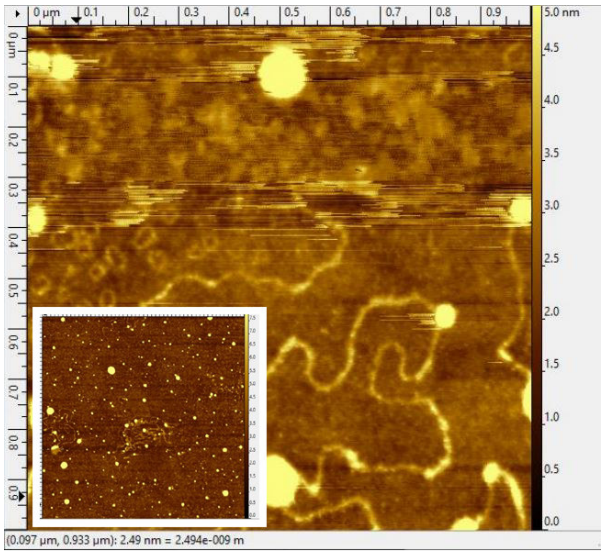

(d) uncleaned *Thermo Scientific* microscope slide, $1\,\mu\mathrm{m} \times 1\,\mu\mathrm{m}$, insert $5\,\mu\mathrm{m} \times 5\,\mu\mathrm{m}$

Figure 47: AFM measurements on PDMS brushes on the drop path (a,b), next to the drop path (c) and on an uncleaned glass slide (d). Measured on a Park NX20 in tapping mode with a cantilever with spring constant 26N/m.

experiment. The washing step in water is done with deionised water from another device as the water used for the water drops. Although the quality should be the same, it may be possible that the water for sample preparation has some contamination that is then washed away by the drops.
Additionally, the PDMS brush surface on glass was tested for drop charging on a different tilted plate setup. The experiment was carried out in cooperation with Amy Stetten (Max Planck Institute for Polymer Research, Mainz). Drops of 45 μl were dropped onto the 45° tilted surface every 5 seconds. After sliding 2 cm the drops passes an electrode that measures the current for the discharge (Figure 48a). From this, the total net charge in the drop can be integrated (Figure 48b). It can be seen that a strong initial charging of ∼10 nC of the drop exists. This decays rapidly down to below 1 nC after about 40 drops and shows a slight increase afterwards. These fluctuations in the end might actually be caused by slight drop path changes as usually surfaces on this setup have been experienced to equilibrate to a constant value. The results confirm that charging happens on this surface. Moreover, the changes of the net charge happen over a similar number of drops as the velocity changes observed on the high-speed goniometer.

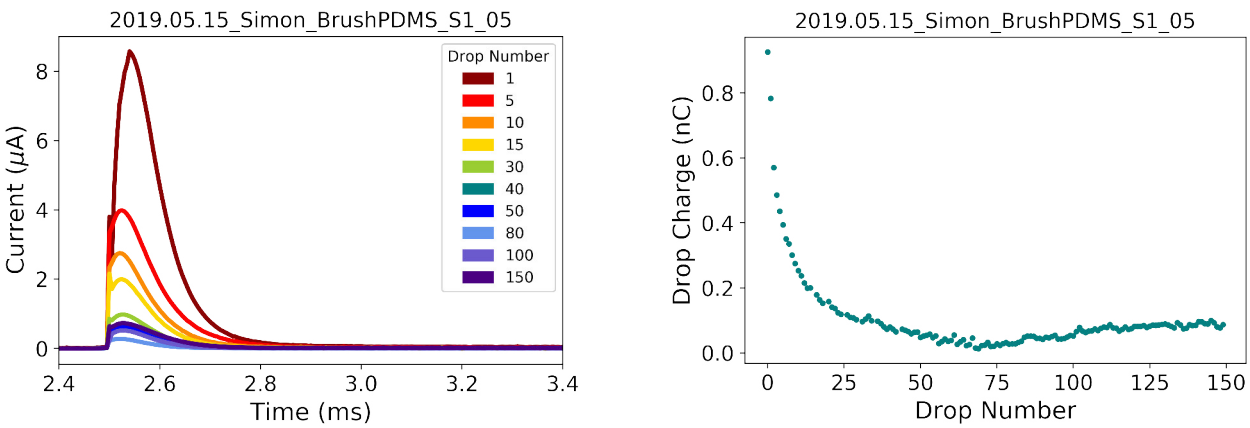

(a) Dropwise current measured

(b) Drop charge over drop number

Figure 48: Charging experiments carried out on PMDS brushes on glass. Diagrams were kindly provided by Amy Stetten.

Investigating the surfaces by additional methods confirmed that charging effects occur and have a similar drop dependence as the velocity. This could indicate that both observations are correlated. Furthermore, it was found that the drops remove contamination of the surface and by that reduce the measured roughness, although not necessarily the roughness of the PDMS film itself. Contamination does not return in a few hours and therefore possibly only affects the first drops. Furthermore, very flat structures were found on the glass substrate, that can be measured also on the PDMS coated surfaces. Although the roughness is below 0.6 nm for the clean surface, in the future a preparation on silicon wafers is recommended to avoid any influence of the substrate.

5 Summary and outlook

Dynamic wetting phenomena appear in many industrial and natural processes and their understanding is important for the improvement of material design in many fields, such as medical science or agriculture. When a liquid wets a surface, it is possible that the contact changes the properties of the surface e.g. by polymer swelling or molecular reorganisation. The wettability can be affected by these changes and this responsive behaviour can be used to design switchable surfaces. A theory for the dynamic contact angle hysteresis (CAH) on adaptive surfaces was proposed by Butt et al. For fast processes, the adaptation would not be noticed in common wetting characterisation methods, because the contact line velocities are too low. These kinds of adaptations might thus still be overlooked but could affect the wetting properties at high speeds, e.g. in industrial coating processes. Therefore, the observation of dynamic contact angles at high contact line velocities can help to characterise rapidly adaptive surfaces correctly and to determine the effect of fast adaptations on the wetting processes.
In this work, a high-speed goniometer was built to measure dynamic contact angles at velocities of less than 1 mm/s to more than 20 cm/s. The setup consists of an adjustable tilted plate, a high-speed camera and a backlight illumination. The telecentric camera objective and illumination produce high contrast images with clear edges, low distortion and high light throughput. For the contact angle measurement, I adapted an already existent software, which uses ellipse fitting and is suitable for non-symmetric drops. The base line detection in the software was improved, the video analysis was modified to be able to handle large inclinations and the automation of the video processing was enhanced. For that, I implemented an algorithm that automatically identifies which parts of the videos contain complete drops and can be used by the measurement software. Two modes of adaptation can be investigated on the setup: velocity dependent contact angles for fast adaptation time scales and drop-wise adaptation for slow adaptation time scales.
I verified the functionality of the setup by measuring the dynamic CAH on two test materials. The dynamic contact angles were investigated for velocities over three orders of magnitude and up to more than 20 cm/s. The test materials were polydimethylsiloxane (PDMS) brushes on glass and a silicon wafer silanised with trichloro(1H,1H,2H,2H-perfluorooctyl)silane (PFOTS). On the PFOTS surface, I measured an approximately symmetric change of contact angles over velocity. That means, that the increase of the advancing contact angle and the decrease of the receding contact angle show a similar dependence on the velocity. The measurements were compared to dynamic contact angle theories, namely the hydrodynamic theory and the molecular kinetic theory (MKT). The hydrodynamic theory is not able to predict the strong velocity dependence for small velocities found on both surfaces. The MKT generally describes the measured values well and yields plausible fitting parameters. For the contact angles of the PDMS brushes the adaptive wetting theory can be fitted well, which is a necessary but not sufficient condition for its verification. Adaptation creates an additional cause for CAH apart from dynamic processes described by the MKT and hydrodynamic theory. Therefore, a combined theory can be formulated describing the static contact angle in MKT with the adaptive wetting theory which improves the fitting. A stronger dependence of the contact angles on velocity is expected on adaptive surfaces due to the additional cause for CAH. The receding contact angle does indeed show a stronger decrease with velocity on the PDMS brushes compared to the PFOTS surface. By contrast, the advancing contact angle is approximately constant over the measured velocity range. The dynamic CAH is therefore strongly asymmetric. If the surface is adaptive, this hints to different adaptation time scales for the advancing and receding adaptation. But the behaviour of the advancing angle on PDMS compared to PFOTS is still unexpected and requires further investigation in the future. One hypothesis is, that the adaptation does not only change the interfacial energies but also the physical properties of the surface, that determine contact angle dynamics (e.g. contact line friction or slip length). Then, a more complex formulation of a combined theory would be required. However,

the aim of this experiment was a proof of concept for the setup and successful. Furthermore, the measurements on the non-adaptive surface agrees well with theory.
Additionally, I investigated the PDMS brushes for slower, drop-wise adaptation by measuring velocity and contact angles over a series of drops. The velocity was found to increase or decrease over the drop number. It is unclear why the observed trends differ so much on the tested samples. The increasing velocity can be explained by a significant increase of contact angles that was observed. Exposing the surface to air for a few minutes or the use of an ionising air blower can reverse the observed changes in velocity to a great extent, but not completely. One possible cause for the observed velocity changes might be charging of the surface. Additional experiments confirmed that drop charging indeed occurs and also shows drop-wise change. It is not clear if this effect is strong enough to explain the change in contact angle, but it is a promising starting point for future investigations.

Outlook

For the PDMS brushes, interesting insights might be gained by varying the film thickness and molecular weight to influence the adaptation time scale. Also, a comparison to PDMS brushes on silicon wafers is of interest. First, because the homogeneity of the brushes seems to be better on wafers. Second, because a thin, doped wafer can decrease the effects of charging. Furthermore, other promising surfaces can be tested on the setup, such as materials consisting of hydrophilic and hydrophobic components. These surfaces are known to reorganise according to the surrounding phase and thereby change their surface energy. That process might be rather slow and therefore very thin films are required to gain adaptation time scales suitable for this setup. For this, already the spin-coating of random copolymers consisting of the hydrophobic poly(styrene) and hydrophilic poly(acrylic acid) was tested, but improvement of the process parameters is required to obtain homogeneous surfaces.
For the verification of the adaptive wetting theory, independent measurements of the adaptation kinetics are indispensable. Currently, they can only be fitted under the assumption that adaptation exists, but other origins of dynamic CAH cannot be separated well. Also, if the dynamic CAH and adaptation time scales can be measured independently, one could calculate the width of the area that influences the contact angle, i.e. the peripheral thickness. Therefore, one important step is the measurement of adaptation times, for example by surface plasmon resonance (SPR).

List of Figures

References

[1] T. D. Blake. “The physics of moving wetting lines”. In: *J Colloid Interface Sci* 299.1 (2006), pp. 1–13.

[2] W. Barthlott and C. Neinhuis. “Purity of the sacred lotus, or escape from contamination in biological surfaces”. In: *Planta* 202.1 (1997), pp. 1–8.

[3] T. Darmanin and F. Guittard. “Superhydrophobic and superoleophobic properties in nature”. In: *Materials Today* 18.5 (2015), pp. 273–285.

[4] P. Olin et al. “Water Drop Friction on Superhydrophobic Surfaces”. In: *Langmuir* 29.29 (2013), pp. 9079–9089.

[5] H. Lin et al. “Effect of surfactant concentration on the spreading properties of pesticide droplets on Eucalyptus leaves”. In: *Biosystems Engineering* 143 (2016), pp. 42–49.

[6] X. J. Liu et al. “Extreme wettability and tunable adhesion: biomimicking beyond nature?” In: *Soft Matter* 8.7 (2012), pp. 2070–2086.

[7] P. World. *Lotus effect*.

[8] H. J. Butt et al. “Adaptive Wetting-Adaptation in Wetting”. In: *Langmuir* 34.38 (2018), pp. 11292–11304.

[9] S. Minko et al. “Two-level structured self-adaptive surfaces with reversibly tunable properties”. In: *J Am Chem Soc* 125.13 (2003), pp. 3896–900.

[10] P. Johnston et al. “Hydrophobic-hydrophilic surface switching properties of nonchain extended poly (urethane) s for use in agriculture to minimize soil water evaporation and permit water infiltration”. In: *Journal of Applied Polymer Science* 134.45 (2017), p. 44756.

[11] O. N. Tretinnikov and Y. Ikada. “Dynamic Wetting and Contact-Angle Hysteresis of Polymer Surfaces Studies with the Modified Wilhelmy Balance Method”. In: *Langmuir* 10.5 (1994), pp. 1606–1614.

[12] K. Grundke et al. “Experimental studies of contact angle hysteresis phenomena on polymer surfaces - Toward the understanding and control of wettability for different applications”. In: *Advances in Colloid and Interface Science* 222 (2015), pp. 350–376.

[13] P.-G. De Gennes, F. Brochard-Wyart, and D. Quéré. *Capillarity and wetting phenomena: drops, bubbles, pearls, waves*. Springer Science & Business Media, 2013.

[14] J. Drelich and E. Chibowski. “Superhydrophilic and Superwetting Surfaces: Definition and Mechanisms of Control”. In: *Langmuir* 26.24 (2010), pp. 18621–18623.

[15] R. E. Johnson and R. H. Dettre. “Contact Angle Hysteresis .3. Study of an Idealized Heterogeneous Surface”. In: *Journal of Physical Chemistry* 68.7 (1964), pp. 1744–&.

[16] J. Long and P. Chen. “On the role of energy barriers in determining contact angle hysteresis”. In: *Advances in Colloid and Interface Science* 127.2 (2006), pp. 55–66.

[17] E. L. Decker and S. Garoff. “Using vibrational noise to probe energy barriers producing contact angle hysteresis”. In: *Langmuir* 12.8 (1996), pp. 2100–2110.

[18] H. B. Eral, D. J. C. M. ’t Mannetje, and J. M. Oh. “Contact angle hysteresis: a review of fundamentals and applications”. In: *Colloid and Polymer Science* 291.2 (2013), pp. 247–260.

[19] E. Chibowski. “Surface free energy of a solid from contact angle hysteresis”. In: *Advances in colloid and interface science* 103.2 (2003), pp. 149–172.

[20] T. D. Blake. “Forced wetting of a reactive surface”. In: *Adv Colloid Interface Sci* 179-182 (2012), pp. 22–8.

[21] C. W. Extrand. “Contact angles and their hysteresis as a measure of liquid-solid adhesion”. In: *Langmuir* 20.10 (2004), pp. 4017–4021.

[22] R. J. Good. “Contact angle, wetting, and adhesion: a critical review”. In: *Journal of Adhesion Science and Technology* 6.12 (1992), pp. 1269–1302.

[23] J. Drelich. “Guidelines to measurements of reproducible contact angles using a sessile-drop technique”. In: *Surface innovations* 1.4 (2013), pp. 248–254.

[24] E. Pierce, F. J. Carmona, and A. Amirfazli. “Understanding of sliding and contact angle results in tilted plate experiments”. In: *Colloids and Surfaces A: Physicochemical and Engineering Aspects* 323.1-3 (2008), pp. 73–82.

[25] B. Krasovitski and A. Marmur. “Drops down the hill: Theoretical study of limiting contact angles and the hysteresis range on a tilted plate”. In: *Langmuir* 21.9 (2005), pp. 3881–3885.

[26] K. Y. Law and H. Zhao. *Surface Wetting: Characterization, Contact Angle, and Fundamentals*. Springer. 2016.

[27] D. L. Schmidt et al. “Contact angle hysteresis, adhesion, and marine biofouling”. In: *Langmuir* 20.7 (2004), pp. 2830–6.

[28] A. ElSherbini and A. Jacobi. “Retention forces and contact angles for critical liquid drops on non-horizontal surfaces”. In: *Journal of Colloid and Interface Science* 299.2 (2006), pp. 841–849.

[29] J. T. Korhonen et al. “Reliable measurement of the receding contact angle”. In: *Langmuir* 29.12 (2013), pp. 3858–3863.

[30] R. Lhermerout and K. Davitt. “Contact angle dynamics on pseudo-brushes: Effects of polymer chain length and wetting liquid”. In: *Colloids and Surfaces A: Physicochemical and Engineering Aspects* 566 (2019), pp. 148–155.

[31] P Petrov and I Petrov. “A combined molecular-hydrodynamic approach to wetting kinetics”. In: *Langmuir* 8.7 (1992), pp. 1762–1767.

[32] M. J. De Ruijter, J. De Coninck, and G Oshanin. “Droplet spreading: partial wetting regime revisited”. In: *Langmuir* 15.6 (1999), pp. 2209–2216.

[33] Y. D. Shikhmurzaev. “The moving contact line on a smooth solid surface”. In: *International Journal of Multiphase Flow* 19.4 (1993), pp. 589–610.

[34] D. Bonn et al. “Wetting and spreading”. In: *Reviews of Modern Physics* 81.2 (2009), pp. 739–805.

[35] R. Sedev. “The molecular-kinetic approach to wetting dynamics: Achievements and limitations”. In: *Advances in Colloid and Interface Science* 222 (2015), pp. 661–669.

[36] A. Clarke and E. Stattersfield. “Direct evidence supporting nonlocal hydrodynamic influence on the dynamic contact angle”. In: *Physics of Fluids* 18.4 (2006).

[37] T. D. Blake et al. “Forced wetting and hydrodynamic assist”. In: *Physics of Fluids* 27.11 (2015), p. 112101.

[38] L. Chen, J. P. Yu, and H. Wang. “Convex Nanobending at a Moving Contact Line: The Missing Mesoscopic Link in Dynamic Wetting”. In: *Acs Nano* 8.11 (2014), pp. 11493–11498.

[39] H. Wang and L. Chen. “A general model for dynamic contact angle over full speed regime”. In: *arXiv preprint arXiv:1902.01204* (2019).

[40] H. Wang. “From Contact Line Structures to Wetting Dynamics”. In: *Langmuir* (2019).

[41] D. Seveno et al. “Dynamics of Wetting Revisited”. In: *Langmuir* 25.22 (2009), pp. 13034–13044.

[42] I Luzinov, S. Minko, and V. V. Tsukruk. “Adaptive and responsive surfaces through controlled reorganization of interfacial polymer layers”. In: *Progress in Polymer Science* 29.7 (2004), pp. 635–698.

[43] H. Yasuda, A. K. Sharma, and T. Yasuda. “Effect of Orientation and Mobility of Polymer-Molecules at Surfaces on Contact-Angle and Its Hysteresis”. In: *Journal of Polymer Science Part B-Polymer Physics* 19.9 (1981), pp. 1287–1291.

[44] M. Morra et al. “On the Aging of Oxygen Plasma-Treated Polydimethylsiloxane Surfaces”. In: *Journal of Colloid and Interface Science* 137.1 (1990), pp. 11–24.

[45] R. J. Good and E. D. Kotsidas. “Contact-Angle of Water on Polystyrene - Study of Cause of Hysteresis”. In: *Journal of Colloid and Interface Science* 66.2 (1978), pp. 360–362.

[46] C. N. C. Lam et al. “Study of the advancing and receding contact angles: liquid sorption as a cause of contact angle hysteresis”. In: *Advances in Colloid and Interface Science* 96.1-3 (2002), pp. 169–191.

[47] K. Hanni-Ciunel, G. H. Findenegg, and R. von Klitzing. “Water contact angle on polyelectrolyte-coated surfaces: Effects of film swelling and droplet evaporation”. In: *Soft Materials* 5.2-3 (2007), pp. 61–73.

[48] J. Dupas et al. “Dynamic wetting on a thin film of soluble polymer: effects of nonlinearities in the sorption isotherm”. In: *Langmuir* 29.40 (2013), pp. 12572–12578.

[49] C. Monteux et al. “The role of hydration in the wetting of a soluble polymer”. In: *Soft Matter* 5.19 (2009), pp. 3713–3717.

[50] A. Tay et al. “How a coating is hydrated ahead of the advancing contact line of a volatile solvent droplet”. In: *European Physical Journal E* 33.3 (2010), pp. 203–210.

[51] R. S. Hansen and M. Miotto. “Relaxation Phenomena and Contact Angle Hysteresis”. In: *Journal of the American Chemical Society* 79.7 (1957), pp. 1765–1765.

[52] F Bierbrauer, N Kapur, and M. Wilson. “Drop Pinch-Off for Discrete Flows from a Capillary”. In: *ESAIM: Proceedings*. Vol. 40. EDP Sciences, 2013, pp. 16–33.

[53] D. Choi et al. “Spontaneous electrical charging of droplets by conventional pipetting”. In: *Scientific Reports* 3 (2013).

[54] S. Optics. *Technicon: Machine Vision*. 2019.

[55] R. Konrath and W. Schroder. “Telecentric lenses for imaging in particle image velocimetry: a new stereoscopic approach”. In: *Experiments in Fluids* 33.5 (2002), pp. 703–708.

[56] G. M. Paredes. “Study of Mooring Systems for Offshore Wave Energy Converters”. In: (2016).

[57] M. L. Technologies. *Collimated Backlights*.

[58] O. Engineering. *Telecentric lenses tutorial*.

[59] N. Le Grand, A. Daerr, and L. Limat. “Shape and motion of drops sliding down an inclined plane”. In: *Journal of Fluid Mechanics* 541.-1 (2005).

[60] T Podgorski, J.-M. Flesselles, and L Limat. “Corners, cusps, and pearls in running drops”. In: *Physical review letters* 87.3 (2001), p. 036102.

[61] B. A. Puthenveettil, V. K. Senthilkumar, and E. J. Hopfinger. “Motion of drops on inclined surfaces in the inertial regime”. In: *Journal of Fluid Mechanics* 726 (2013), pp. 26–61.

[62] F. Träger. *Springer handbook of lasers and optics*. Springer Science & Business Media, 2012.

[63] N. K. Andersen and R. Taboryski. “Drop shape analysis for determination of dynamic contact angles by double sided elliptical fitting method”. In: *Measurement Science and Technology* 28.4 (2017).

[64] W. L. Chen et al. “50th Anniversary Perspective: Polymer Brushes: Novel Surfaces for Future Materials”. In: *Macromolecules* 50.11 (2017), pp. 4089–4113.

[65] M. Stamm. “Polymer surfaces and interfaces”. In: *Characterization, Modification and Applications; Springer: Berlin, Germany* (2008).

[66] J. Habicht et al. “Swelling of thick polymer brushes investigated with ellipsometry”. In: *Langmuir* 15.7 (1999), pp. 2460–2465.

[67] M. Biesalski and J. Ruhe. “Swelling of a polyelectrolyte brush in humid air”. In: *Langmuir* 16.4 (2000), pp. 1943–1950.

[68] C. A. Naini et al. “Probing the Intrinsic Switching Kinetics of Ultrathin Thermoresponsive Polymer Brushes”. In: *Angewandte Chemie-International Edition* 50.19 (2011), pp. 4513–4516.

[69] N. A. Peppas and N. M. Franson. “The Swelling Interface Number as a Criterion for Prediction of Diffusional Solute Release Mechanisms in Swellable Polymers”. In: *Journal of Polymer Science Part B-Polymer Physics* 21.6 (1983), pp. 983–997.

[70] S. Wooh and D. Vollmer. “Silicone Brushes: Omniphobic Surfaces with Low Sliding Angles”. In: *Angewandte Chemie-International Edition* 55.24 (2016), pp. 6822–6824.

[71] J. M. Watson and M. G. Baron. “The behaviour of water in poly(dimethylsiloxane)”. In: *Journal of Membrane Science* 110.1 (1996), pp. 47–57.

[72] H. Teisala et al. *Grafting silicone at room temperature – A transparent, scratch-resistant non-stick molecular coating*. 2019, submitted to Science.

[73] S. H. North et al. “Effect of Physicochemical Anomalies of Soda-Lime Silicate Slides on Biomolecule Immobilization”. In: *Analytical Chemistry* 82.1 (2010), pp. 406–412.

[74] K. Yatsuzuka, Y. Higashiyama, and K. Asano. “Electrification of polymer surface caused by sliding ultrapure water”. In: *Ieee Transactions on Industry Applications* 32.4 (1996), pp. 825–831.

[75] B. S. Yilbas et al. “Dynamics of a water droplet on a hydrophobic inclined surface: influence of droplet size and surface inclination angle on droplet rolling”. In: *Rsc Advances* 7.77 (2017), pp. 48806–48818.

[76] P. Durbin. “Considerations on the moving contact-line singularity, with application to frictional drag on a slender drop”. In: *Journal of Fluid Mechanics* 197 (1988), pp. 157–169.

[77] H. Y. Kim, H. J. Lee, and B. H. Kang. “Sliding of liquid drops down an inclined solid surface”. In: *Journal of Colloid and Interface Science* 247.2 (2002), pp. 372–380.

[78] G. Ahmed et al. “Modeling the effects of contact angle hysteresis on the sliding of droplets down inclined surfaces”. In: *European Journal of Mechanics B-Fluids* 48 (2014), pp. 218–230.

[79] D. W. Pilat et al. “Dynamic measurement of the force required to move a liquid drop on a solid surface”. In: *Langmuir* 28.49 (2012), pp. 16812–20.

[80] N. Gao et al. “How drops start sliding over solid surfaces”. In: *Nature Physics* 14.2 (2017), pp. 191–196.

[81] G. Lorenzini. “Simplified modelling of sprinkler droplet dynamics”. In: *Biosystems Engineering* 87.1 (2004), pp. 1–11.

[82] M Aminzadeh et al. “On the motion of Newtonian and non-Newtonian liquid drops”. In: *Scientia Iranica* 19.5 (2012), pp. 1265–1278.

[83] S. Varagnolo. “Study and control of drop motion on inclined surfaces”. PhD thesis. UNIVERSITA DEGLI STUDI DI PADOVA, 2016.

[84] S. Ray et al. “Influence of the work of adhesion on the dynamic wetting of chemically heterogeneous surfaces”. In: *Langmuir* 24.22 (2008), pp. 13007–13012.

[85] J.-H. Kim, H. P. Kavehpour, and J. P. Rothstein. “Dynamic contact angle measurements on superhydrophobic surfaces”. In: *Physics of Fluids* 27.3 (2015), p. 032107.

[86] T. Omori et al. “Understanding the asymmetry between advancing and receding microscopic contact angles”. In: *Soft matter* (2019).

[87] J. H. Snoeijer and B. Andreotti. “Moving contact lines: scales, regimes, and dynamical transitions”. In: *Annual review of fluid mechanics* 45 (2013), pp. 269–292.

[88] A. Hourlier-Fargette et al. “Role of uncrosslinked chains in droplets dynamics on silicone elastomers”. In: *Soft Matter* 13.19 (2017), pp. 3484–3491.

[89] L. S. Puah et al. “Influence of surface charge on wetting kinetics”. In: *Langmuir* 26.22 (2010), pp. 17218–17224.

[90] H. Y. Jing, S. Sinha, and S. Das. “Elasto-electro-capillarity: drop equilibrium on a charged, elastic solid”. In: *Soft Matter* 13.3 (2017), pp. 554–566.

[91] B. S. Yilbas et al. “Water Droplet Dynamics on a Hydrophobic Surface in Relation to the Self-Cleaning of Environmental Dust”. In: *Scientific reports* 8.1 (2018), p. 2984.

Table of symbols

Symbol	Unit	Description
A	m^2	area
D	m	equivalent diameter
g	m/s^2	gravitational acceleration
h_0	m	falling height
h	kg m^2/s	Planck constant
k_B	kg $m^2/s^2/K$	Boltzmann constant
F	N	force
G	J	activation free energy
L	m	length
l	m	peripheral length
R	m	radius
d	m	distance
t	s	time
T	K	temperature
v	m/s	velocity
V	m^3	volume
W	J	work
x	m	position
α	deg	inclination angle
γ	N/m	surface energy
ζ	N/m	friction coefficient
θ	deg	contact angle
κ	Hz	frequency
λ	m	distance of adsorption sites
μ	Pa s	dynamic viscosity
ρ	kg/m^3	density
ν	m^3	molecular volume

Index	Description
A	advancing
Adh	adhesion
app	apparent
c	critical
E	Young (equilibrium)
g	gas
LG	liquid-gas
LA	lateral
m	microscopic
max	maximum
min	minimum
R	receding
s	slip
SG	solid-gas
SL	solid-liquid
vis	viscous
w	wetting

∞	equilibrium
0	initial
$*$	quasi-static

Acronym	Long form
ATRP	atom transfer radical polymerisation
Ca	capillary number
CAH	contact angle hysteresis
DSAfM	Drop shape analysis for MATLAB
IAB	ionising air blower
PDMS	Polydimethylsiloxane
PHEMA	Polyhydroxyethylmethacrylate
PFOTS	Perfluorodecyltrichlorosilane
Re	Reynolds number
SI	silicon wafer

A Appendix

A.1 Contact angle measuring

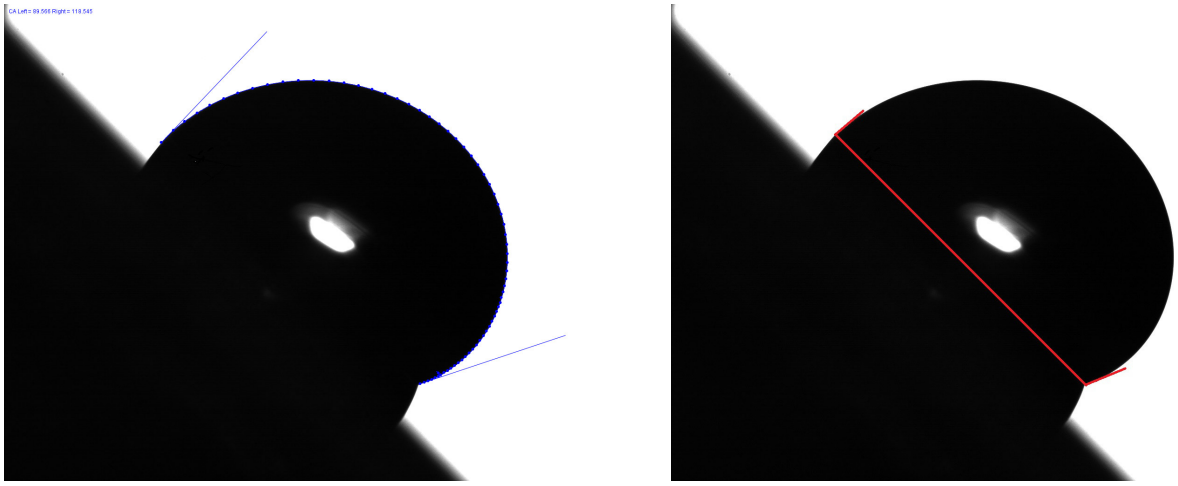

(a) *DropSnake* **(b)** per hand

Figure 49: Measuring contact angle by *ImageJ* plugin *DropSnake* or per hand.

A.2 Quasi-static contact angle measurements

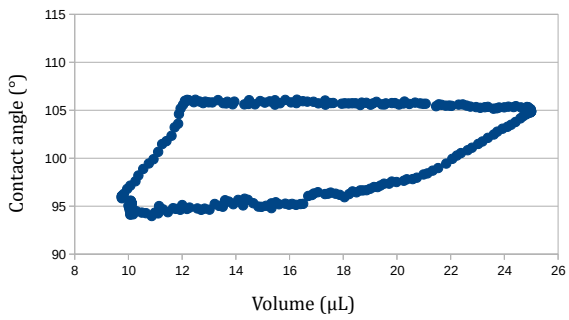

(a) PDMS on glass batch 1

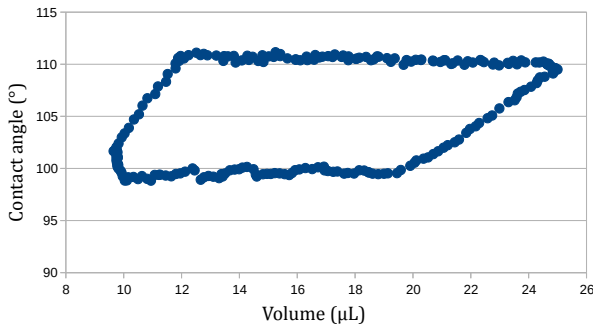

(b) PDMS on glass batch 2

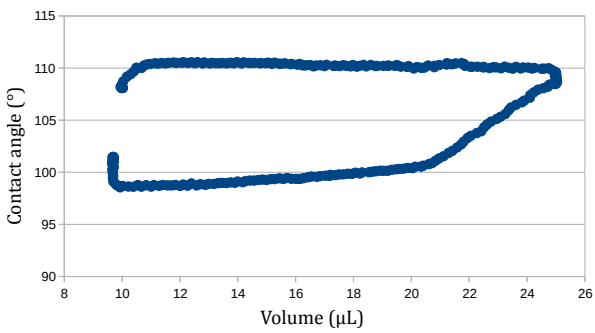

(c) PDMS on wafer

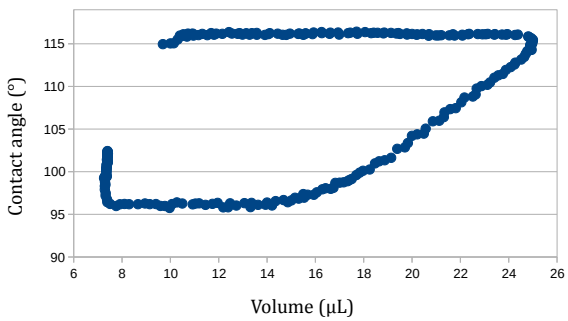

(d) PFOTS on wafer

Figure 50: Examples of the inflating drop measurement results done on a DataPhysics OCA 35. Drop were inflated from 10μL to 25μL and back with 1μL/s.

A.3 Drop dynamics

(a) t = 0 ms **(b)** t = 8 ms **(c)** t = 14 ms **(d)** t = 20 ms **(e)** t = 26 ms **(f)** t = 88 ms

Figure 51: Drop impact on PDMS.

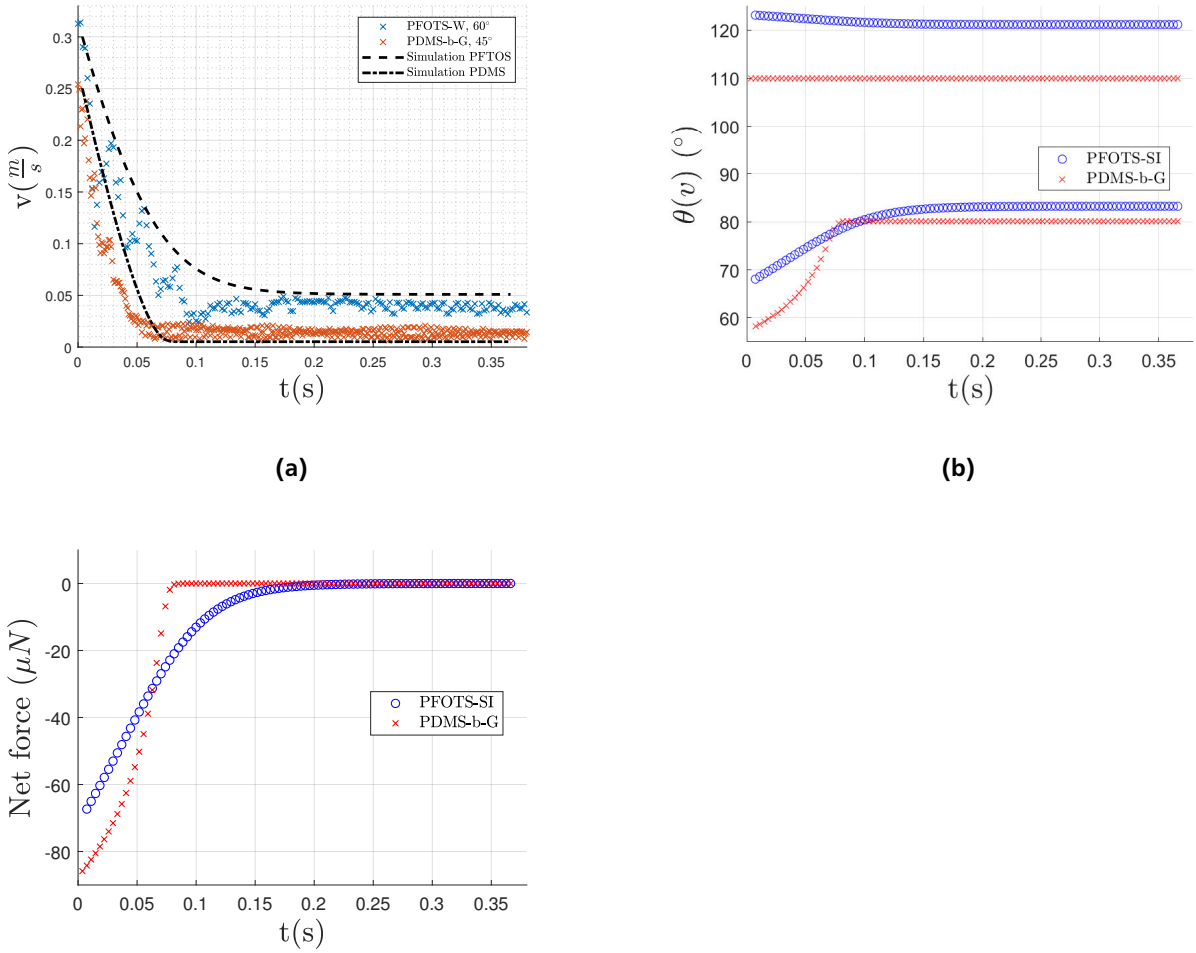

(a) **(b)** **(c)**

Figure 52: Initial drop dynamics. Picture (a) shows a comparison of numerical solution of Equation (27) to measurement results of the initial drop dynamics. The drop volume was $(17.6 \pm 0.3)\mu\mathrm{L}$ on both surfaces. Pictures (b) and (c) show the simulation results for contact angels and net forces ($F_{Adh} - G$) on the drop.

A.4 Drop-wise adaptation

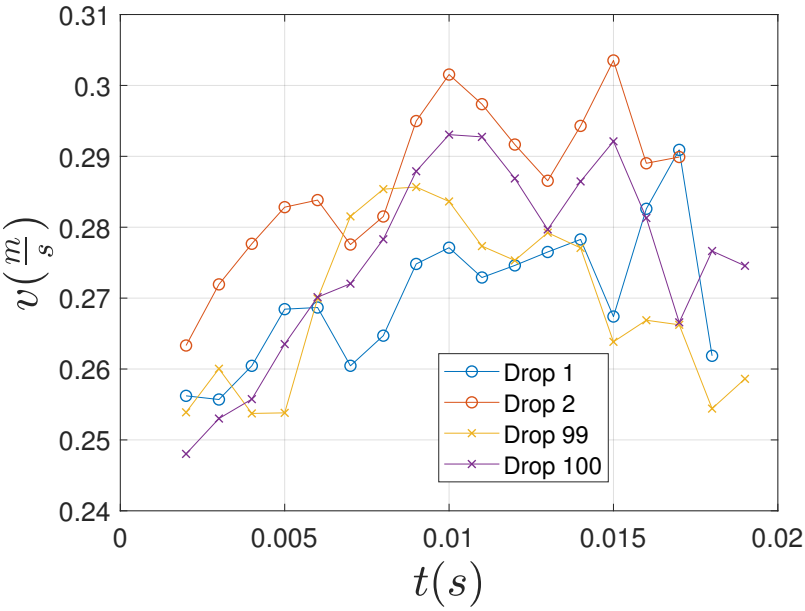

Figure 53: Measurement of drop velocities for PFOTS coated glass

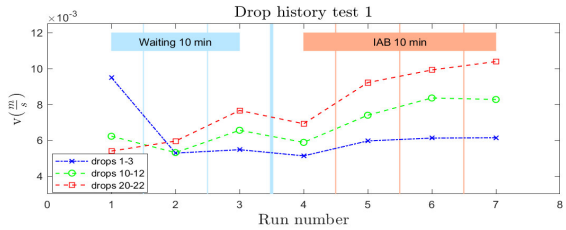

(a) Velocities

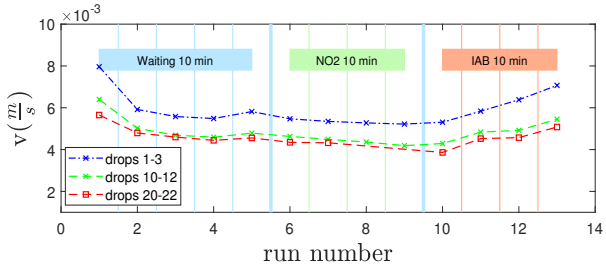

(b) Velocities

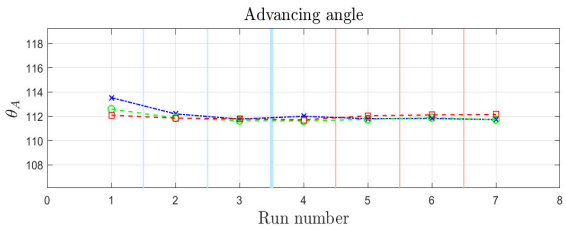

(c) Advancing angle

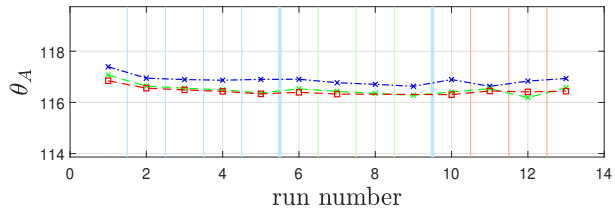

(d) Advancing angle

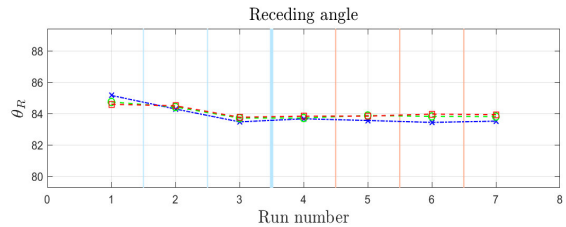

(e) Receding angle

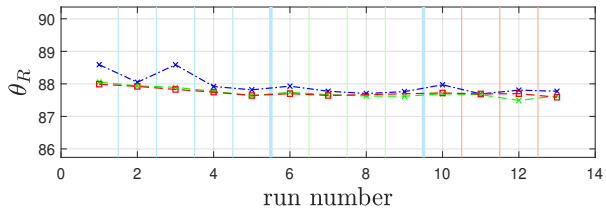

(f) Receding angle

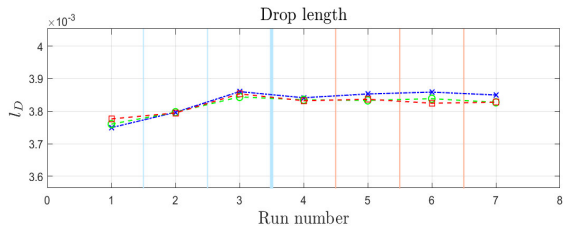

(g) Drop length

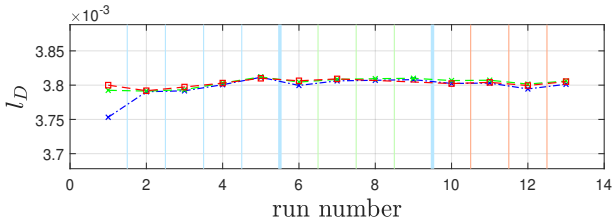

(h) Drop length

Figure 54: Experiment 2 on batch 1 on the left, experiment 1 done on a sample from batch 2 on the right.

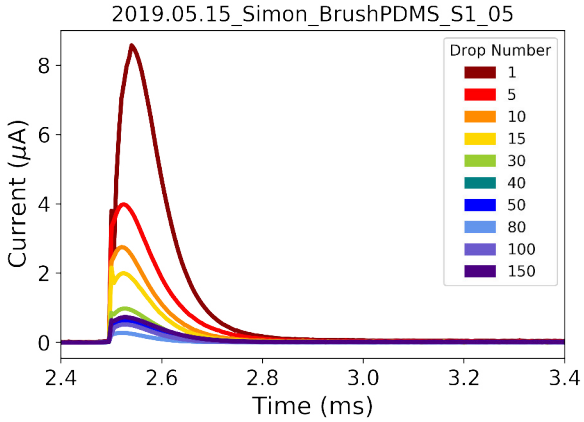

(a) Dropwise current measured - Exp 1

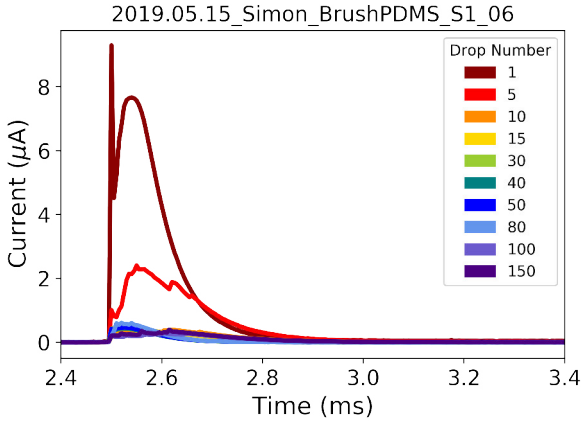

(b) Dropwise current measured - Exp 2

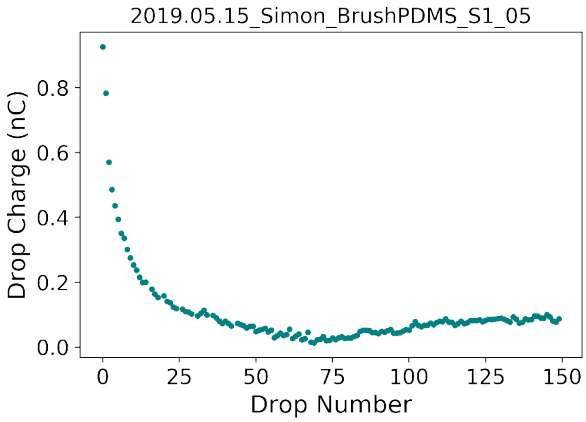

(c) Drop charge - Exp 1

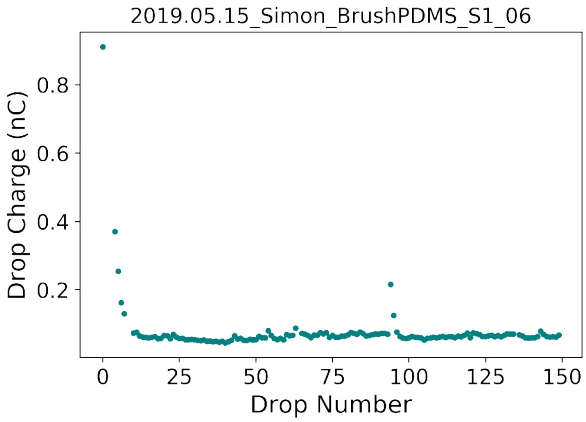

(d) Drop charge - Exp 2

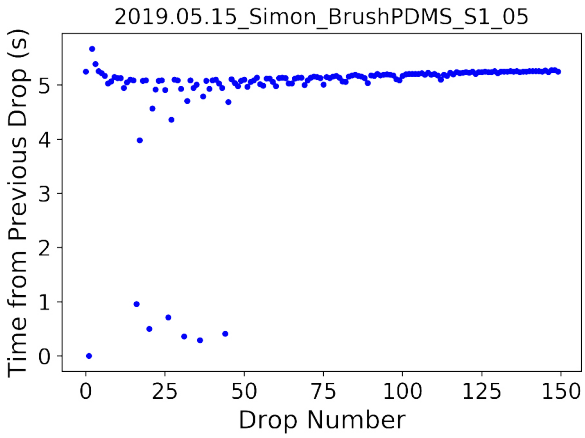

(e) Time in between drops - Exp 1

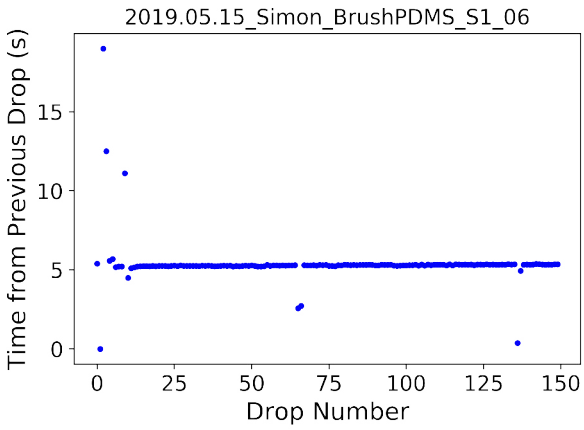

(f) Time in between drops - Exp 2

Figure 55: Charging experiments carried out on PMDS brushes on glass. Diagrams were kindly provided by Amy Stetten.